THE UNIVERSITY *of* EDINBURGH

Ultrafast Imaging of Photochemical Dynamics via X-ray Scattering: Connecting Theory and Experiments

Nikola Zotev

Doctor of Philosophy

The University of Edinburgh

2020

"The purpose of science is not to cure us of our sense of mystery and wonder, but to constantly reinvent and reinvigorate it."

Robert Sapolsky

Abstract

Although photochemical reactivity has been extensively studied, a clear picture of the underlying dynamics is largely missing predominantly because of the extremely short reaction times involved in these processes. The rapid development of X-ray free electron laser (XFEL) facilities in the last decade has fostered the emergence of new types of experiments that target photochemical dynamics. One of these new prominent techniques is non-resonant Ultrafast X-ray Scattering (UXS). In a pump-probe fashion, it enables the direct observation of structural dynamics on a femtosecond timescale. Due to the extreme brightness of the XFEL, these experiments can be performed even in gas phase. Because of the unconstrained molecular motion and lack of intermolecular interference, gas-phase UXS is a meeting ground for experimental and theoretical studies of the quantum nature of photochemical dynamics.

As promising as they are, gas-phase UXS experiments are still in their early days. A lot of fundamental aspects remain unexplored, and rigorous theoretical and computational frameworks are not established. This thesis aims to bridge existing gaps between theory and experiments, presenting an account of recent advances in data analysis and interpretation. The work gives an outline of the theory of time-dependent molecular quantum mechanics following photoexcitation, as well as X-ray-matter interaction. Practical aspects of the post-experimental analysis are presented. These include separation of the observed signal into isotropic and anisotropic scattering components, which allows internal and rotational molecular degrees of freedom to be dealt with independently in the analysis. The process of extracting useful information about the dynamics of the molecule as the reaction unfolds requires careful consideration of how to optimally represent the experimental signal and what inversion schemes are feasible given

the limitations of the experiment. The data interpretation often relies on input from computational modelling. This thesis also describes a computational scheme for calculating generalised (elastic, inelastic, total and coherent mixed) isotropic X-ray scattering cross-sections directly from the *ab initio* wave function of the molecule.

This methodological apparatus is applied in the analysis of a number of experiments, and the findings are presented. It is shown that X-ray scattering is in principle sensitive even to small rearrangements of the electrons upon absorption of light. The ability to detect the initially excited electronic state by means of transition dipole moment alignment is demonstrated in the case of the excitation of N-methylmorpholene (NMM) by a 200 nm linearly polarised laser. The subsequent dynamics, more specifically the fast coherent vibrations, are extracted from the experiment creating a "molecular movie" with high spatial resolution via high-throughput conformational sampling guided by computational modelling. Separately, the rate of dissociation of trimethylamine (TMA) after excitation is obtained from the loss of scattering interference between the fragments over the course of the reaction.

Lay summary

For more than a century, X-rays have been the tool of choice when unravelling the structure of matter. However, X-ray scattering is often considered a structure determination technique for condensed phase, *i.e.* solids or liquids, where the high density leads to a strong experimental signal. Applications to gas phase were limited. Similarly, X-ray studies of chemical reactions were restricted to matter undergoing slow physical transformations due to the lack of suitable pulsed X-ray sources needed to study fast reactions. This has all changed with the advent of X-ray Free Electron Lasers (XFELs), which produce extremely short pulses of X-rays with unprecedented brightness. Their arrival opened the door for ultrafast X-ray scattering (UXS) imaging even in gas phase.

One area where this new technology has great potential is the study of reactions initiated by light, known as photochemical reactions. Firstly, photochemical transformations tend to be extremely fast – on a femtosecond or picosecond timescale. Secondly, fundamentals of photochemical changes are best studied in gas phase, where, unlike condensed phase, the molecules are not affected by the environment, so the dynamics are unconstrained and closest to ideal conditions from a theoretical point of view.

In a typical UXS experiment in gas phase, a sample of molecules is excited by a UV laser, and then snapshots of its dynamics are recorded using X-ray pulses at different time delays, mapping out structural changes in order to create a "molecular movie". The aim of this thesis is to present a theoretical account of all aspects of this process, while maintaining a clear focus on how it relates to the interpretation and the analysis of ongoing experiments. In addition, the thesis describes computational algorithms that can be used to simulate the observables in these experiments. Their application to the analysis of a number of experiments yields a fruitful set of findings, which are presented in the final chapters of the thesis.

Acknowledgements

To claim that I am solely responsible for the writing of this monograph, although true by academic standards, is unfair on a deeper personal level. It is hard to imagine that it would have ever come to exist without the continuous help and support of my colleagues, friends and family.

First and foremost, I wish to thank my supervisor, teacher, mentor and friend, Dr Adam Kirrander, for allowing me to follow him down the rabbit hole to the wonderland of quantum mechanics. Although I believe that I mostly stayed true to my own style of work and thinking, I have come to realise how much I have adopted from his unique approach to science. His advice and guidance were indispensable to me.

I would like to thank all of my colleagues on both sides of the Atlantic - Dr Thomas Northey, Dr Andrés Moreno Carrascosa, Dr Mats Simmermacher, Dr Darren Bellshaw and Kyle Acheson in Edinburgh for the stimulating discussions and their friendship; as well as Haiwang Yong, Dr Brian Stankus, Dr Jennifer M. Ruddock and Prof. Peter M. Weber in Providence, Rhode Island, for their patience and eagerness to communicate experimental findings with theoreticians.

And last but not least, I would like to express my gratitude to my friends and family scattered around the world. A very special mention is reserved for the two people who stood by me day by day throughout my PhD - my brother and my wife. The numerous witty exchanges and discussions of science, philosophy and politics with my brother, Aleksandar Zotev, were a constant reminder of the existence of a bigger picture out there. My loving wife, Polina Zoteva, was often the only light to guide me and chase away the sweeping darkness of the computer terminal.

Contents

List of Figures

List of Tables

List of Abbreviations

BOA	Born-Oppenheimer approximation
IC	Internal conversion
ISC	Intersystem crossing
SOC	Spin-orbit coupling
PES	Potential energy surface
XFEL	X-ray Free-Electron Laser
SASE	Self-amplified spontaneous emission
SLAC	Stanford Linear Accelerator
LCLS	Linac Coherent Light Source
UXS	Ultrafast X-ray Scattering
QED	Quantum electrodynamics
CHD	1,3-cyclohexadiene
TDM	Transition dipole moment
NMM	N-methylmorpholine
TMA	Trimethylamine
DMA	Dimethylamine
TDSE	Time-dependent Schrödinger equation
TISE	Time-independent Schrödinger equation
TDPT	Time-dependent Perturbation Theory
NACME	Nonadiabatic coupling matrix element
EM	Electromagnetic
IAM	Independent Atom Model
HF	Hartree-Fock
CI	Configuration Interaction
CSF	Configuration State Function
MCSCF	Multiconfigurational Self-Consistent Field
CASSCF	Complete Active Space Self-Consistent Field

SA-CASSCF	State-Averaged Complete Active Space Self-Consistent Field
CASPT2	Complete Active Space 2^{nd} order Perturbation Theory
MS-CASPT2	Multistate Complete Active Space 2^{nd} order perturbation theory
MRCI	Multireference Configuration Interaction
RDM	Reduced Density Matrix

List of Publications

Work included in this thesis has been published in the following papers:

[1] Haiwang Yong, **Nikola Zotev**, Brian Stankus, Jennifer M. Ruddock, Darren Bellshaw, Sébastien Boutet, Thomas J. Lane, Mengning Liang, Sergio Carbajo, Joseph S. Robinson, Wenpeng Du, Nathan Goff, Yu Chang, Jason E. Koglin, Max D. J. Waters, Theis I. Sølling, Michael P. Minitti, Adam Kirrander and Peter M. Weber. "Determining Orientations of Optical Transition Dipole Moments using Ultrafast X-Ray Scattering", *The Journal of Physical Chemistry Letters* **9**, 6556 (2018)

[2] Jennifer M. Ruddock, **Nikola Zotev**, Brian Stankus, Haiwang Yong, Darren Bellshaw, Sébastien Boutet, Thomas J. Lane, Mengning Liang, Sergio Carbajo, Wenpeng Du, Adam Kirrander, Michael P. Minitti and Peter M. Weber. "Simplicity beneath Complexity: Counting Molecular Electrons Reveals Transients and Kinetics of Photodissociation Reactions", *Angewandte Chemie International Edition* **58**, 6371 (2019)

[3] Brian Stankus, Haiwang Yong, **Nikola Zotev**, Jennifer Ruddock, Darren Bellshaw, Thomas J. Lane, Mengning Liang, Sébastien Boutet, Sergio Carbajo, Joseph S. Robinson, Wenpeng Du, Nathan Goff, Yu Chang, Jason E. Koglin, Michael P. Minitti, Adam Kirrander and Peter M. Weber. "Ultrafast X-Ray Scattering Reveals Vibrational Coherence Following Rydberg Excitation", *Nature Chemistry*, **11**, 716 (2019)

[4] **Nikola Zotev**, Andrés Moreno Carrascosa, Mats Simmermacher and Adam Kirrander. "Excited Electronic States in Total Isotropic Scattering from Molecules", *Journal of Chemical Theory and Computation*, **16**, 2594 (2020)

Further work not included in this thesis has been published in the following papers:

[5] Thomas Northey, **Nikola Zotev**, and Adam Kirrander. "*Ab initio* Calculation of Molecular Diffraction", *Journal of Chemical Theory and Computation* **10**, 4911 (2014)

[6] Brian Stankus, **Nikola Zotev**, David M. Rogers, Yan Gao, Asami Odate, Adam Kirrander and Peter M. Weber. "Ultrafast photodissociation dynamics of 1,4-diiodobenzene", The Journal of Chemical Physics **148**, 194306 (2018)

[7] Jennifer M. Ruddock, Haiwang Yong, Brian Stankus, Wenpeng Du, Nathan Goff, Yu Chang, Andrés Moreno Carrascosa, Darren Bellshaw, **Nikola Zotev**, Mengning Liang, Sergio Carbajo, Jason Koglin, Joseph S. Robinson, Sébastien Boutet, Adam Kirrander, Michael P. Minitti and Peter M. Weber. "The Deep-UV, Photo-Induced Ring-Opening Dynamics of 1,3-Cyclohexadiene", *Science Advances* **5**, eaax6625 (2019)

[8] Haiwang Yong, Jennifer M. Ruddock, Brian Stankus, Lingyu Ma, Wenpeng Du, Nathan Goff, Yu Chang, **Nikola Zotev**, Darren Bellshaw, Sébastien Boutet, Sergio Carbajo, Jason E. Koglin, Mengning Liang, Joseph S. Robinson, Adam Kirrander, Michael P. Minitti, and Peter M. Weber. "Scattering off molecules far from equilibrium", *Journal of Chemical Physics* **151**, 084301 (2019)

[9] Haiwang Yong, **Nikola Zotev**, Jennifer M. Ruddock, Brian Stankus, Mats Simmermacher, Andrés Moreno Carrascosa, Wenpeng Du, Nathan Goff, Yu Chang, Darren Bellshaw, Mengning Liang, Sergio Carbajo, Jason Koglin, Joseph S. Robinson, Sébastien Boutet, Michael P. Minitti, Adam Kirrander and Peter M. Weber. "Observation of the molecular response to light upon photoexcitation", *Nature Communications* **11**, 2157 (2020)

Chapter 1

Introduction

1.1 Overview

Photochemical processes are central to life. They are responsible for photosynthesis, vision and sensing, many metabolic processes and even for the chemical dynamics in the Earth's atmosphere. They also offer a range of novel applications in areas such as optical switches [1], and energy capture and storage [2]. Despite their importance, the time evolution of photochemical processes is still not completely understood, and generalised mechanisms based on qualitative understanding are often missing. This demands a case-by-case approach for many individual light-molecule systems, leading to a fragmented body of knowledge with little scope for extrapolation to new reactions and chemical species [3]. The gaps in our understanding are rooted in the simple fact that photochemical dynamics pushes the boundaries of both our exprimental means and our ability to comprehend the quantum world of molecular motion. Experimentally, the most significant challenge is posed by the extremely short (pico- or femtosecond) timescale associated with the majority of photochemical processes. From a theoretical point of view, the photoinduced dynamics exhibit a rich palette of quantum mechanical effects, whose investigation requires computational techniques beyond classical molecular dynamics. More specifically, photochemistry occurs on a multitude of electronic states leading to coupling between electronic and nuclear degrees of freedom [4]. The resulting non-adiabatic dynamics manifest themselves most strongly in the regions of conical intersections or avoided crossings, where the Born-Oppenheimer approximation

(BOA) breaks down [5].

1.2 Photochemistry

Before embarking on a journey through the theory of light-matter interaction, it is worth building up an intuitive picture of photochemistry. In the most general sense, photochemistry deals with chemical transformations initiated by light. It should be acknowledged that in this thesis, and throughout the literature, the term is used in a broader sense to refer also to photophysical processes in matter, *i.e.* processes that do not lead to new chemical species. The scope of photochemistry is by no means narrow – it includes processes in the energy domain, as well as reactivity and structural reorganisation of matter [6]. As it will become evident in the following chapters, this thesis is exclusively concerned with *molecular* photochemistry.

A crucial concept in this domain of science is that of excited electronic states. In fact, excited-state chemistry is often synonymous with photochemistry despite the fact that excited electronic states can sometimes be accessed via collisional pathways [7, 8]. Leaving aside this possibility, a photochemical transformation begins by the absorption of a photon by the molecule to form an excited electronic state, or a superposition thereof if more than one state appears in the bandwidth of the absorbed light. The energy difference between the newly accessed electronic state and the ground state is that of the absorbed photon[1]. In addition, there is an associated reorganisation of the electrons of the molecule in space. The latter should be emphasised strongly at this stage as it has profound consequences to the work presented here. The Stark-Einstein law establishes the equivalence between the number of photons absorbed by a system and the number of excited molecules [9]. It holds true in the so-called linear regime, *i.e.* low intensity of light. At higher intensities, multi-photon excitations become dominant, which is referred to as nonlinear optical regime and is not going to be discussed in this thesis [10].

[1] Strictly speaking, energy may also go into vibrational or rotational modes

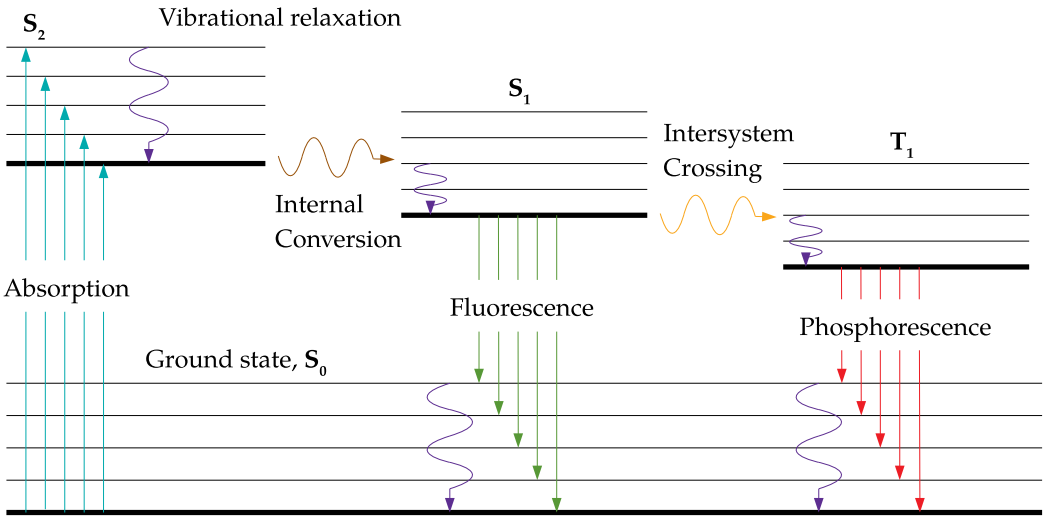

FIGURE 1.1: Jablonski diagram of a typical photophysical process, showing the possible radiative and non-radiative transitions. The molecule is excited from a singlet ground state, S_0, into a singlet excited state, S_2, where it undergoes vibrational relaxation. The population can then be transferred to the S_1 singlet state via internal conversion. The molecule can emit a photon and fluoresce to the ground state. The S_1 and the triplet T_1 states are coupled via intersystem crossing. Population trapped in the triplet state can return to the ground state via phosphorescence, which is a slow "forbidden" process.

Once the molecule is excited, it can undergo a variety of transitions that can be grouped in two categories - non-radiative and radiative, which are depicted in Figure 1.1. If energy can be dissipated to the surroundings as assumed in Figure 1.1, the first step is often vibrational relaxation in the vibrational manifold in the originally excited electronic state. In addition, the molecule may transition to another electronic state. Internal conversion (IC) is a non-radiative transition between two such states with the same spin multiplicity, while intersystem-crossing (ISC) occurs between states with different multiplicity and is driven by spin-orbit coupling (SOC). These processes also occur in collision-free gas-phase molecular systems, where energy cannot be dissipated to the surroundings. Radiative transitions to

a lower energy level involve emission of a photon. As vibrational relaxation is generally faster than radiative transitions, the energy of the emitted photon is lower than that of the absorbed by the amount of energy lost to the surroundings. Fluorescence is a radiative transition between states of the same multiplicity, while phosphorescence is a "forbidden" transition between states of different multiplicity, mediated by SOC. We are often concerned with transitions to a ground state of a singlet multiplicity, as found in most organic molecules, in which case fluorescence and phosphorescence are associated with singlet-to-singlet and triplet-to-singlet transitions, respectively. This summary of the possible photochemical outcomes is somewhat simplified and certainly applicable mainly to molecules made up of light atoms. The terminology becomes blurred in the presence of heavy atoms, where the magnitude of the SOC makes the concept of spin-multiplicity ill-defined, since the conserved quantity is the total angular momentum.

In addition, the above description puts the emphasis on the energetics of the system in the way that is useful to spectroscopy. However, it lacks a clear explanation of the underlying motion that is inherently coupled to the changes that occur in the energy domain. How are nuclei and electrons moving during a photochemical reaction? The answer to this question has a twofold significance. On the one hand, we perceive the word in terms of objects and their motion, rather than energy, which makes this description of photochemistry much more tangible. On the other hand, it has a major impact on our ability to control photochemical reactions and design new drugs, electronics and materials for the industry.

The language of photochemical dynamics in intertwined with that of time-dependent quantum mechanics. After photoexcitation, the electrons of the molecule have gained energy from the photon and have redistributed themselves in space. Being negatively charged, their new arrangement disrupts the electrostatic equilibrium that existed previously between them and the N_n nuclei of the system. As the electrons are lighter and move faster, it is convenient to adopt a formalism in which electrons and nuclei

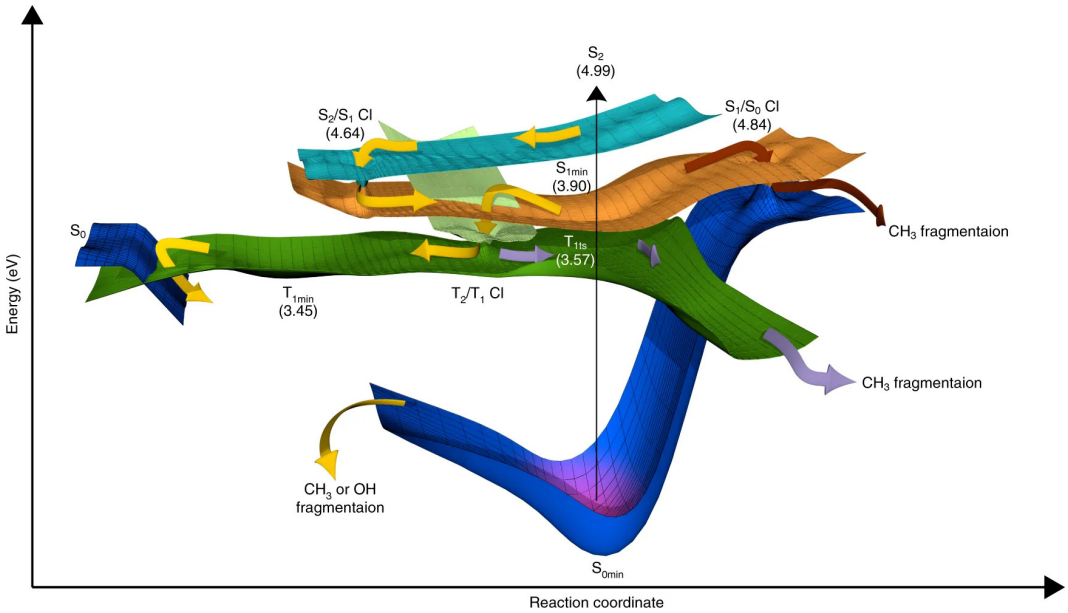

FIGURE 1.2: A schematic of the potential energy surfaces (PESs) encountered in the relaxation dynamics of acetetylaceton after a photoexcitation from the S_0 ground state (dark blue) to the S_2 state (light blue), which has $\pi\pi^*$ character. The wave packet encounters and passes through conical intersections to other electronic states as it slides down the PES manifold to form different final products. Reproduced from Ref. [11]

are treated separately. This is known as the Born-Oppenheimer approximation [12]. In this description, the nuclei experience a force from the current arrangement of electrons, move accordingly and the electrons follow instantaneously. In other words, there is no nuclear motion on the timescale of electron rearrangement. It follows that nuclear motion can be described with respect to a potential energy profile, known as a potential energy surface (PES), dictated by the forces exerted by electrons. The PES for each electronic state is characterised by its own unique topology on which nuclear dynamics evolves as depicted in Figure 1.2. There are two points of paramount importance with respect to how this happens. Firstly, the nuclei are quantum objects and their position is described by a nuclear wave

packet, *i.e.* a superposition of eigenstates of the nuclear Hamiltonian characterised by a certain degree of coherence resulting from the way the system was prepared. In accordance with the Born interpretation of quantum mechanics, the wave packet gives the probability amplitude of finding the nuclei in a given arrangement. Secondly, internal conversions and intersystem crossings occur in the vicinity of specific regions, where two (or more) PES come close together. These regions are called avoided-crossings (diatomic molecules) or conical intersections (more than two atoms) on account of their topology in 1D and 2D, respectively. This is where coupling between nuclear and electronic degrees of freedom occurs and the Born-Oppenheimer approximation breaks down, resulting in a partial or full population transfer between states. Sliding down the manifold of electronic states in this manner, potential energy is converted into kinetic, which can be lost to the surroundings, drive conformational changes, or simply be retained as vibrational motion.

Thus, it is clear that photochemistry is significantly different from ground state reactivity. The latter is characterised by products and intermediates that can be reached via a thermal barrier. In a photochemical reaction, the energy supplied by the photon is orders of magnitude larger than thermal energy, and allows for a broader scope of products and intermediates. While still in the excited state, the molecule could be quite different from the ground state both in terms of its conformation and reactivity. As we will see in the following chapters, these not-so-subtle effects can be observed in a very direct way. Last but not least, photochemistry is initiated by light, *e.g.* an optical laser, that can be easily controlled in a lab. That makes photochemistry an attractive tool for selective reactivity with far-reaching applications.

1.3 Experimental Studies of Photochemistry

Although slow photochemical reactions were studied as early as the beginning of the 19th century [13], the first major breakthrough came after the

development of flash photolysis in the 1940s and 1950s, which allowed reaction rates on the millisecond time-scale to be experimentally observed [14, 15]. Just 30 years later, Zewail and co-workers revolutionised the field by utilising femtosecond lasers to study intramolecular vibrational-energy redistribution and the dynamics of transition-state species [16, 17]. In other words, the focus moved from kinetics to the inner-workings of the ultrafast quantum world of photochemistry. Not surprisingly, this paradigm shift brought Zewail the Nobel Prize in chemistry in 1999.

Ever since flash-photolysis, the time-evolution of photochemical reactions is experimentally studied via different pump-probe schemes regardless whether they monitor reaction rates or an observable related to transient dynamics. A schematic of a prototypical pump-probe experiment is presented in Figure 1.3. The reaction is first initiated by an excitation with an optical laser, the pump pulse. The photoabsorption creates a coherent wave packet in an excited state. The shape and coherence properties of the wave packet are dictated by the pump laser for any given system. The time of the initial excitation, more specifically the time that marks the temporal centre of the pump pulse, is designated as time-zero. Then time-evolution is interrogated by a probe laser with a given time delay with respect to time-zero. This is then repeated for different time delays between the two pulses. The series of "snapshots" gives a representation of the photochemical transformation as a function of time. The procedure critically depends on the short duration of both the pump and the pulse laser, which determines the temporal resolution of the experiment. Put simply, the pulse duration needs to be short on the scale of the process of interest so as to be able to track it.

Although tremendously useful, spectroscopic techniques ultimately measure transitions between different states, and hence, only probe the molecular geometry indirectly. In contrast, rapid advances in laser technology, relativistic electron sources, and synchrotron radiation have opened the door for direct time-resolved imaging of molecular dynamics [19]. Most notably, the recent development of X-ray free-electron lasers (XFELs) provided the much-needed tools for a new type of experiments that utilise extremely short, bright and tunable X-ray pulses to image photochemical dynamics.

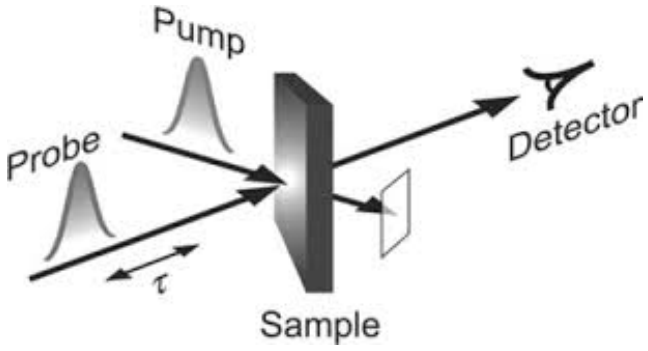

FIGURE 1.3: A simplified schematic of a pump-probe experiment. The molecule is excited by an optical pump laser; the arrival of its centre marks time-zero of the experiment. As the photochemical reaction unfolds, the sample is investigated with a probe pulse, which may or may not be another optical laser. The time-delay between the two pulses, τ, is varied in order to record a time-resolved change over the course of the reaction, *e.g.* absorption spectrum, photoelectron spectrum, scattering, *etc*. Reproduced from Ref. [18]

This fascinating new technology is discussed in the next section.

1.4 X-ray Free-Electron Lasers

XFEL operation is based on the process of self-amplified spontaneous emission (SASE) [20]. Electrons that are accelerated near the speed of light are injected in a periodic magnetic field created by alternating magnets called undulators. As a result, the electron bunch emits X-rays, which travel together with the electrons and reshape them in microbunches. The electron microbunches are spaced in accordance with the wavelength of the photons. This facilitates coordinated coherent emission of more X-rays. Figure 1.4 shows a schematic of the process.

Nine orders of magnitude brighter than synchrotron radiation and superior in terms of coherence properties [21], XFELs are an unrivalled source of soft and hard X-rays for numerous experiments such as crystal-free diffraction imaging of biological molecules [22, 23], X-ray absorption in the strong-field regime [24], and time-resolved X-ray diffraction [25]. Apart from the

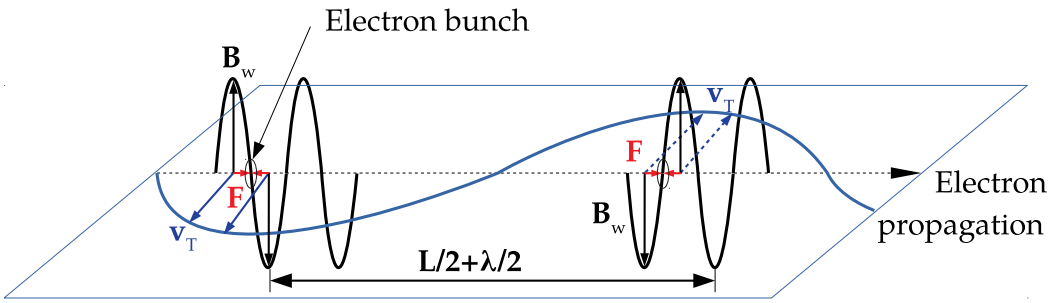

FIGURE 1.4: A schematic representation of microbunching in the undulator field at XFELs. As the electrons travel through the array of magnets, they experience a Lorentz force so that their transverse velocity, $\mathbf{v}_T$, oscillates. The emitted X-rays have a magnetic field, $\mathbf{B}_w$, and wavelength, λ. The interaction between the X-ray magnetic field and the electrons' transverse velocity results in a force that is collinear to the direction of propagation. The direction of the force is reversed each half wavelength. This causes the electrons to bunch together. Note that in the time the electrons travel half an undulator period, $L/2$, the X-rays travel $L/2 + \lambda/2$, so that the electrons' transverse velocity and the electromagnetic field change sign. As a result, the direction of the force on the electrons is preserved.

high intensity, the ultrafast time-resolution plays a critical role in the success of the type of ultrafast X-ray scattering experiments discussed in this thesis. The current minimum pulse duration is sub-femtosecond [26], which is sufficient to monitor the motion of molecular fragments or individual atoms, and is pushing towards the boundary of electron motion in some slow processes [27].

At the present time, there are five operational XFELs in the hard X-ray regime - Linear Coherent Light Source (LCLS) at Stanford [28], SACLA in Japan [29], PAL-XFEL in South Korea [30], the European XFEL in Hamburg [31], and SwissFEL in Switzerland [32]. In addition, there are two XFELs in the soft X-ray regime - FERMI in Trieste, Italy, [33] and FLASH in Hamburg [34]. Finally, the construction of the Shanghai High Repetition Rate XFEL and Extreme Light Facility (SHINE), another hard X-ray facility, began in 2018, and is scheduled to be completed by 2025 [35]. The science

case for a potential UK-based X-ray free-electron laser (XFEL) is currently being evaluated on behalf of the Science and Technology Facilities Council (STFC).

1.5 Ultrafast X-ray Scattering

The merits of XFELs open incredible opportunities for studying some of the fundamental questions in photochemistry such as how atoms move inside molecules [36], how chemical bonds are broken and formed [37], and how electrons respond to light [38]. Ultrafast imaging at XFELs brings us one step closer to thinking of the experimental process as simply making a "molecular movie".

This thesis will focus on one particular imaging technique, which became possible with the advent of XFELs – non-resonant ultrafast X-ray scattering (UXS) in dilute gas phase. In this pump-probe technique, a sample of dilute gas is photoexcited with a pulsed optical laser, and the subsequent photodynamics is probed with hard X-rays generated by an XFEL. The small number of scattering molecules in gas phase, combined with the low X-ray scattering cross section (*e.g.* low as compared to electrons) and fast dynamics, makes this type of experiments particularly challenging. They are only possible using very short and intense X-ray pulses, which currently are only available at XFELs.

It is prudent at this stage to point out certain differences between the more familiar X-ray crystallography in solid state and UXS in gas phase. The lack of a periodic lattice and the large average separation between molecules in gas phase render scattering free from interference between molecules for all detectable scattering angles [39]. The signal then becomes an incoherent sum of scattering intensities from isolated molecules. It can be argued that quantum effects are most easily observed in their pure form on this single-molecule level, making gas-phase UXS an important crossroad between theory and experiments. Furthermore, in the case of crystallography,

the periodicity of crystals leads to a coherent amplification of elastic scattering at the Bragg peaks; inelastic scattering remains incoherent [40]. In contrast, in gas phase both elastic and inelastic scattering are strictly incoherent and should be treated equivalently. As it will be discussed in Chapter 2, the latter has important implications for sensitivity to electron correlation [41, 42].

In addition, it is worth noting that X-ray crystallography is traditionally a tool for structure determination for ground-state molecules. In contrast, the dynamics studied by UXS evolves on a number of electronic states, each defined by its own PES and distinctive electron distribution. Hence, neither theory nor computational tools inherited from the last 100 years of developments in crystallography are best-suited for the interpretation and analysis of UXS experiments [43–53].

1.6 Overview

The purpose of this thesis is to present some recent advances in bridging the gap between theory and UXS experiments in gas phase. Despite being written primarily from the perspective of theory and computational methodology, it puts a strong emphasis on real-world applications. Chapter 2 summarises a number of key aspects of the theory of molecular photochemical dynamics and non-resonant X-ray scattering. It introduces important concepts such as the molecular Hamiltonian, the Born-Oppenheimer approximation, non-adiabatic dynamics, as well as vibrational and rotational molecular motion. Chapter 2 also reviews X-ray scattering in the framework of second quantisation. Chapter 3 deals with practical aspects of the analysis of experiments in connection to the underlying theory. It discusses the decomposition of the detected signal in isotropic and anisotropic components and their importance, in addition to experimentally relevant quantities such as the excitation fraction and percentage intensity change. Inversion schemes from reciprocal to real space are also discussed. Chapter 4 presents a computational methodology for calculating isotropic scattering directly from the *ab initio* wave function of the molecule. Relevant aspects

of *ab initio* calculations of excited states are also considered in the same chapter.

Once a firm theoretical and computational basis has been established, the following chapters provide examples of recent experiments that make use of that methodology. The ability to differentiate between excited states is discussed in Chapter 5. The procedure outlined there is based on the anisotropy of the detected signal, which originates from the interplay between the electronic transition dipole moment of the molecule and the laser polarisation axis. The system investigated is N-methylmorpholine (NMM) following excitation by a 200 nm linearly polarised optical pulse. The same system is used in Chapter 6, where the coherent vibrations in the Rydberg manifold are tracked with a high degree of spatial and temporal resolution. Chapter 7 is devoted to the kinetics of photodissociation of trimethylamine (TMA) with an emphasis on the loss of coherence between the molecular fragments, and its fingerprint in the detected signal.

Chapter 2

Theory

2.1 Overview

This chapter aims to give a comprehensive, yet concise, overview of the theory behind UXS experiments in the gas phase. From a theoretical point of view, any UXS scattering experiment can be thought of as three interconnected processes – molecular dynamics, photoexcitation and X-ray scattering – which are described here in turns. The treatment of the molecular motion relies on a high-level description of the molecular Hamiltonian that includes coupling between electronic and nuclear degrees of freedom, *i.e.* non-adiabatic dynamics. A substantial part of the discussion is devoted to light-matter interaction. The excitation with an optical laser and the X-ray scattering process are dealt with in the framework of first-order perturbation theory, with explicit quantisation of the electromagnetic (EM) field.

Generally, this thesis is concerned with non-relativistic radiation field description and molecular dynamics. The former is well justified in the case of small photon energy (100 eV–100 keV for X-rays) compared to the rest mass of the electron (511 keV). Relativistic effects on the electronic structure depend on the mass of the nuclei involved. The work presented in later chapters does not involve heavy nuclei so a detailed discussion of relativistic corrections such as SOC is not given. However, the reader is reminded that such effects cannot be ignored in heavy atoms.

Since the focus of this thesis is to bridge the gap between theory and experiments, there is a strong emphasis on the connection between the two. In

other words, how theory manifests itself in the experiments, and what levels of approximations might be suitable for different experimental scenarios. However, discussions of more practical matters concerning the experimental design and analysis are left for Chapter 3. Given the broad scope of the theoretical framework, it is inevitable that certain aspects are not derived *de novo* and the reader is directed to the appropriate resources.

2.2 Time-Dependent Schrödinger Equation

The time-dependent Schrödinger equation (TDSE) governs the evolution of the photochemical system and, in a broader sense, is the basis of all non-relativistic[1] quantum dynamics:

$$\imath\hbar\frac{\partial|\Psi(t)\rangle}{\partial t} = \hat{H}|\Psi(t)\rangle. \tag{2.1}$$

In Eq. (2.1), $|\Psi(t)\rangle$ is the total time-dependent wave function of the system, $\imath$ is the imaginary unit, $\hbar$ is the reduced Planck's constant and $\hat{H}$ is the Hamiltonian operator. An excellent and thorough discussion of the TDSE and its pivotal role in atomic and molecular chemistry and physics can be found in Ref. [54]. The TDSE can be classified as a diffusion equation with a complex diffusion coefficient, whose solution is the wave function. In reference to the Born interpretation, the wave function of the system is a probabilistic all-encompassing description of its state. For example, famously, the probability of finding a particle in a volume of space at position $\boldsymbol{r}$ at time t is given by $|\Psi(\boldsymbol{r},t)|^2 d\boldsymbol{r}$. In quantum mechanics, a physical observable is associated with a Hermitian operator whose eigenvalues are the possible outcomes of the measurement of that observable. A measurement collapses the wave function to a single eigenstate of the corresponding operator. One such operator is the Hamiltonian operator, which gives the total energy of the system, E. For a system of N_{en} interacting particles, *e.g.* the nuclei (n) and electrons (e) constituting a molecule, described by a set of coordinates,

[1] Eq. (2.1) is also valid in the relativistic limit of the Dirac equation but its interpretation is slightly different on account of the symmetric treatment of space and time.

$\bar{\boldsymbol{r}} = \{\boldsymbol{r}_1, \boldsymbol{r}_2, ..., \boldsymbol{r}_{N_{\text{en}}}\}$, its most generic form is

$$\hat{H} = -\sum_{i=1}^{N_{\text{en}}} \frac{\hbar^2}{2m_i} \nabla_i^2 + V(\bar{\boldsymbol{r}}, t), \tag{2.2}$$

where $V(\bar{\boldsymbol{r}}, t)$ is the potential, m_i is the mass of particle i, and $\nabla_i^2 = \partial^2/\partial x_i^2 + \partial^2/\partial y_i^2 + \partial^2/\partial z_i^2$ is the Laplacian. The first term is readily understood to be the sum of the kinetic energies of the particles. Eq. (2.1) and Eq. (2.2) are, in fact, quite general and can accept any form of potential. However, it is prudent to differentiate between the possible scenarios.

In the first, the potential is independent of time. That is, the particles experience a static potential, *e.g.* as a result of their pairwise interactions or the presence of a static field. This situation corresponds to, for example, an isolated molecule, as discussed in Section 2.7. In that case, we can approach the solution of Eq. (2.1) by separation of variables using $\Psi(\bar{\boldsymbol{r}}, t) = \psi(\bar{\boldsymbol{r}})\theta(t)$:

$$\frac{\imath\hbar}{\theta(t)} \frac{\partial\theta(t)}{\partial t} = \frac{1}{\psi(\bar{\boldsymbol{r}})} \hat{H}\psi(\bar{\boldsymbol{r}}) = E, \tag{2.3}$$

where E is the energy of the system, here acting as a separation constant. That leads to two simultaneous equations:

$$\hat{H}\psi(\bar{\boldsymbol{r}}) = E\psi(\bar{\boldsymbol{r}}), \tag{2.4}$$

$$\imath\hbar \frac{\partial\theta(t)}{\partial t} = E\theta(t). \tag{2.5}$$

Eq. (2.4) is the time-independent Schrödinger equation (TISE), while Eq. (2.5) is a first-order differential equation with solutions:

$$\theta(t) = \theta_0 e^{-\imath Et/\hbar}. \tag{2.6}$$

Therefore, the particular solutions of the TDSE are given by:

$$\Psi(\bar{\boldsymbol{r}}, t) = \psi(\bar{\boldsymbol{r}}) e^{-\imath Et/\hbar}, \tag{2.7}$$

where we require that the wave function is normalised. The general solution of the TDSE is then given by a linear superposition of the solutions in Eq. (2.7):

$$|\Psi(t)\rangle = \sum_i c_i e^{-\imath E_i t/\hbar} |\psi_i\rangle, \tag{2.8}$$

where c_i are expansion coefficients determined by the initial conditions, and $|\psi_i\rangle$ are the eigenstates of the Hamiltonian, *i.e.* the solutions of the corresponding TISE. Eq. (2.8) is referred to as a wave packet because it represents the coherent superposition of the eigenstates of the TISE with their associated time evolution, trivially manifested as complex phase factors that oscillate in time.

In the case when the Hamiltonian is time-dependent, *e.g.* when the molecule interacts with a time-varying electromagnetic field, simple separation of variables does not work any more. The solution of the TDSE is then approached by perturbation theory as discussed in the following section.

2.3 Time-Dependent Perturbation Theory

Time-Dependent Perturbation Theory (TDPT) is a technique used to obtain approximate solutions for quantum mechanical systems that cannot be solved exactly. A critical requirement for the validity of the approach is to be able to represent the Hamiltonian as a sum of two parts – a time-independent Hamiltonian with known eigenfunctions, and a small perturbation. We start off by considering a Hamiltonian of the form $\hat{H} = \hat{H}_0 + \hat{V}$, where $\hat{V}$ is the small perturbation, and $\hat{H}_0$ is a time-independent Hamiltonian. Although TDPT is primarily used for time-dependent perturbations, as its name suggests, the method is equally useful if $\hat{V}$ does not depend on time. For the purposes of TDPT, it is helpful to introduce the so-called interaction picture by defining a wave function, $|\Psi_{\mathrm{I}}(t)\rangle$:

$$|\Psi_{\mathrm{I}}(t)\rangle = e^{\imath \hat{H}_0 t/\hbar} |\Psi(t)\rangle = \hat{U}_0^\dagger(t) |\Psi(t)\rangle, \tag{2.9}$$

where $|\Psi(t)\rangle$ refers to the Schrödinger representation of the wave function defined as a solution to Eq. (2.1). The operator $\hat{U}_0(t)$ is the time-evolution

operator, also known as the propagator, for the unperturbed system in the Schrödinger representation. In essence, the definition of the interaction wave function in Eq. (2.9) eliminates the time dependence of the Schrödinger wave function associated with the unperturbed motion encoded in $\hat{H}_0$. The wave function in the interaction representation obeys the following equation of motion:

$$\begin{aligned}
\imath\hbar\frac{\partial|\Psi_{\mathrm{I}}(t)\rangle}{\partial t} &= \imath\hbar\frac{\partial\hat{U}_0^\dagger(t)}{\partial t}|\Psi(t)\rangle + \imath\hbar\hat{U}_0^\dagger(t)\frac{\partial|\Psi(t)\rangle}{\partial t} \\
&= -\hat{H}_0\hat{U}_0^\dagger(t)|\Psi(t)\rangle + \hat{U}_0^\dagger(t)\hat{H}|\Psi(t)\rangle \\
&= \hat{U}_0^\dagger(t)(\hat{H}-\hat{H}_0)|\Psi(t)\rangle \\
&= \hat{U}_0^\dagger(t)\hat{V}|\Psi(t)\rangle \\
&= \hat{U}_0^\dagger(t)\hat{V}\hat{U}_0(t)\hat{U}_0^\dagger(t)|\Psi(t)\rangle \\
&= \hat{V}_{\mathrm{I}}|\Psi_{\mathrm{I}}(t)\rangle,
\end{aligned} \tag{2.10}$$

where $\hat{V}_{\mathrm{I}} = \hat{U}_0^\dagger(t)\hat{V}\hat{U}_0(t)$ is the interaction picture Hamiltonian, and we have used the fact that $\hat{H}_0$ and $\hat{U}_0^\dagger(t)$ commute, and the relationship between $\hat{H}$ and the time derivative implied by the TDSE. Eq. (2.10) is equivalent to the TDSE but expressed in the interaction picture. If we define an interaction propagator operator $\hat{U}_{\mathrm{I}}(t,t_0)$ that propagates the wave function from an initial time t_0 to t:

$$\begin{aligned}
|\Psi_{\mathrm{I}}(t)\rangle = \hat{U}_{\mathrm{I}}(t,t_0)|\Psi_{\mathrm{I}}(t_0)\rangle &= \hat{U}_0^\dagger(t,t_0)\hat{U}(t,t_0)|\Psi(t_0)\rangle \\
&= e^{\imath\hat{H}_0(t-t_0)/\hbar}e^{-\imath\hat{H}(t-t_0)/\hbar}|\Psi(t_0)\rangle,
\end{aligned} \tag{2.11}$$

this operator obeys the interaction TDSE in Eq. (2.10):

$$\imath\hbar\frac{\partial\hat{U}_{\mathrm{I}}(t,t_0)}{\partial t} = \hat{V}_{\mathrm{I}}\hat{U}_{\mathrm{I}}(t,t_0). \tag{2.12}$$

Eq. (2.12) can be dealt with by integration, which leads to a self-consistent solution of the form:

$$\hat{U}_{\mathrm{I}}(t,t_0) = \hat{1} - \frac{\imath}{\hbar}\int_{t_0}^{t} dt'\hat{V}_{\mathrm{I}}(t')\hat{U}_{\mathrm{I}}(t',t_0). \tag{2.13}$$

Iterative expansion of Eq. (2.13) results in the Dyson series:

$$\hat{U}_{\mathrm{I}}(t,t_0) = \hat{1} + \sum_{n=1}^{\infty} \left(-\frac{\iota}{\hbar}\right)^n \int_{t_0}^{t} dt_n ... \int_{t_0}^{t_2} dt_1 \hat{V}_{\mathrm{I}}(t_n) ... \hat{V}_{\mathrm{I}}(t_1) \hat{U}_{\mathrm{I}}(t_1,t_0), \quad (2.14)$$

which is subject to the time-ordering constraint $t > t_n > ... > t_1 > t_0$. We now seek to transform Eq. (2.14) to the Schrödinger picture. First, we note that ignoring the effect of the perturbation between t_0 and t_1 sets $\hat{U}_{\mathrm{I}}(t_1,t_0)$ to 1. We then use Eq. (2.11) in combination with the definition of potential in the interaction picture, $\hat{V}_{\mathrm{I}}(t) = \hat{U}_0^{\dagger}(t,t_0)\hat{V}(t)\hat{U}_0(t,t_0)$, to arrive at:

$$\begin{aligned}\hat{U}(t,t_0) = \hat{U}_0(t,t_0) + \sum_{n=1}^{\infty} \left(-\frac{\iota}{\hbar}\right)^n \int_{t_0}^{t} dt_n ... \int_{t_0}^{t_2} dt_1 \hat{U}_0(t,t_n)\hat{V}(t_n)\hat{U}_0(t_n,t_{n-1}) \\ \times \hat{V}(t_{n-1}) ... \hat{U}_0(t_2,t_1)\hat{V}(t_1)\hat{U}_0(t_1,t_0).\end{aligned} \quad (2.15)$$

With reference to the structure of Eq. (2.15), the following picture emerges. The system evolves unperturbed between t_0 and t_1, at which time perturbation $\hat{V}(t_1)$ is applied, which is then followed by another period of unperturbed evolution between t_2 and t_1, followed by another perturbation, and so on. If the perturbation is small, we can truncate the series to first order, which gives the first-order correction to the wave function:

$$|\Psi^{(1)}(t)\rangle = -\frac{\iota}{\hbar} \int_{t_0}^{t} dt' \hat{U}_0(t,t')\hat{V}(t')\hat{U}_0(t',t_0)|\Psi_0(t_0)\rangle, \quad (2.16)$$

where the propagator has been applied to $|\Psi_0(t_0)\rangle$, the wave function at time t_0 before the system was perturbed. The first-order probability amplitude of finding the system in a final state of the unperturbed Hamiltonian, $\langle f|$, at time t is given by:

$$\langle f(t)|\Psi(t)\rangle = \langle f(t)|\Psi_0(t)\rangle + \langle f(t)|\Psi^{(1)}(t)\rangle. \quad (2.17)$$

In the case where the system is initially in a single eigenstate, $|i\rangle$, the first-order transition amplitude, $S_{fi}(t)$, is then:

$$\begin{aligned} S_{fi}(t) &= \delta_{fi} - \frac{\iota}{\hbar}\langle f(t)| \int_{t_0}^{t} dt' \hat{U}_0(t,t')\hat{V}(t')\hat{U}_0(t',t_0)|i(t_0)\rangle \\ &= \delta_{fi} - \frac{\iota}{\hbar}\int_{t_0}^{t} dt' e^{\iota(E_f - E_i)t'/\hbar}\langle f|\hat{V}(t')|i\rangle. \end{aligned} \tag{2.18}$$

In the context of this thesis, TDPT theory is used to treat the interaction between light and matter as discussed in Sections 2.6 and 2.8. In that case, the unperturbed Hamiltonian is the sum of the Hamiltonian of the molecule and that of the EM field. While it is easy to recognise the former in Eq. (2.2), it is harder to see the connection between the electromagnetic waves and quantum particles. The following section aims to provide the missing pieces of the puzzle.

2.4 Quantisation of the Electromagnetic Field

The discussion of light-matter interaction starts with the classical description of electromagnetic (EM) fields in terms of Maxwell's equations:

$$\nabla \cdot \mathbf{E} = \frac{\rho}{\varepsilon_0} \tag{2.19}$$

$$\nabla \cdot \mathbf{B} = 0 \tag{2.20}$$

$$\nabla \times \mathbf{E} = -\frac{\partial \mathbf{B}}{\partial t} \tag{2.21}$$

$$\nabla \times \mathbf{B} = \mu_0 \left(\mathbf{J} + \varepsilon_0 \frac{\partial \mathbf{E}}{\partial t} \right), \tag{2.22}$$

where $\mathbf{E}$ and $\mathbf{B}$ are the electric and magnetic fields, respectively. The scalar constants ε_0 and μ_0 are the permittivity and permeability of free space, respectively, and are related to the speed of light, c, via $c^2 = (\varepsilon_0 \mu_0)^{-1}$. In addition, Maxwell's equations feature the charge density distribution, ρ, and the current density, $\mathbf{J}$. Although not explicitly shown, the electric and magnetic fields are time-dependent. An alternative but equivalent definition of

this set of equations can be achieved by defining a vector potential, $\mathbf{A}$, and a scalar potential Φ that are related to the electric and magnetic fields by:

$$\mathbf{B} = \nabla \times \mathbf{A} \tag{2.23}$$

$$\mathbf{E} = -\nabla\Phi - \frac{\partial \mathbf{A}}{\partial t}. \tag{2.24}$$

The resulting field equations are:

$$\nabla^2\Phi + \frac{\partial}{\partial t}(\nabla \cdot \mathbf{A}) = -\frac{\rho}{\varepsilon_0} \tag{2.25}$$

$$\left(-\nabla^2 + \frac{1}{c^2}\frac{\partial^2}{\partial t^2}\right)\mathbf{A} + \nabla\left(\nabla \cdot \mathbf{A} + \frac{1}{c^2}\frac{\partial \Phi}{\partial t}\right) = \mu_0 \mathbf{J}. \tag{2.26}$$

The potentials $\mathbf{A}$ and Φ are not uniquely defined. More specifically, a gauge transformation with respect to an arbitrary scalar function, Ω:

$$\mathbf{A} \to \mathbf{A} + \nabla\Omega \tag{2.27}$$

$$\Phi \to \Phi + \frac{\partial \Omega}{\partial t}, \tag{2.28}$$

still fulfils Eq. (2.23) and Eq. (2.24). Different choices of Ω can be used to bring the field equations, Eq. (2.25) and Eq. (2.26), into a form that is suitable for further calculations. Here, we choose the Coulomb gauge defined by:

$$\nabla^2\Omega = -\nabla \cdot \mathbf{A}, \tag{2.29}$$

so that $\nabla \cdot \mathbf{A} = 0$. *In vacuo*, *i.e.* when $\rho = 0$ and $\mathbf{J} = 0$, with $\Phi = 0$, this results in a wave equation of the form:

$$\nabla^2\mathbf{A} = \frac{1}{c^2}\frac{\partial^2 \mathbf{A}}{\partial t^2}. \tag{2.30}$$

The Coulomb gauge condition implies that the vector potential, $\mathbf{A}$, is entirely transversal. Inside a cavity of volume $L^3 = V$ subject to periodic

boundary conditions, it can be expanded as a Fourier series of plane waves:

$$\mathbf{A}(\mathbf{r},t) = \sum_{\boldsymbol{k}} \mathbf{A}_{\boldsymbol{k}}(t) e^{\imath \boldsymbol{k}\cdot\mathbf{r}}, \tag{2.31}$$

where the wave vectors are given by $\boldsymbol{k} = \sum_{i=x,y,z} 2\pi n_i \mathbf{e}_i / L$ with $n_i \in \mathbb{Z}$. Since $\mathbf{A}$ is real, we can rewrite Eq. (2.31) as:

$$\mathbf{A}(\mathbf{r},t) = \sum_{\boldsymbol{k}} \mathbf{a}_{\boldsymbol{k}}(t) e^{\imath \boldsymbol{k}\cdot\mathbf{r}} + \mathbf{a}^*_{\boldsymbol{k}}(t) e^{-\imath \boldsymbol{k}\cdot\mathbf{r}}. \tag{2.32}$$

The time-dependence of the Fourier coefficients can easily be found by substitution in Eq. (2.30) to be:

$$\mathbf{a}_{\boldsymbol{k}}(t) = \mathbf{a}_{\boldsymbol{k}} e^{\imath \omega_k t}, \tag{2.33}$$

where $\omega_{\boldsymbol{k}} = c|\boldsymbol{k}|$. On the other hand, the Coulomb gauge condition implies that $\boldsymbol{k} \cdot \mathbf{a}_{\boldsymbol{k}} = 0$, which means that the wave amplitude is perpendicular to the direction of propagation given by $\boldsymbol{k}$. In the plane perpendicular to the propagation, $\mathbf{a}_{\boldsymbol{k}}(t)$ is uniquely specified with respect to (any) two mutually orthogonal vectors, $\mathbf{e}_{k1}$ and $\mathbf{e}_{k2}$. These vectors can be chosen to be complex or real as long as they fulfil the orthonormalisation condition, $\mathbf{e}_{k\sigma}\mathbf{e}_{k\sigma'} = \delta_{\sigma\sigma'}$. With that, the vector potential can be rewritten as:

$$\mathbf{A}(\mathbf{r},t) = \sum_{\boldsymbol{k}} \sum_{\sigma} a_{k\sigma}(t) \mathbf{e}_{k\sigma} e^{\imath \boldsymbol{k}\cdot\mathbf{r}} + a^*_{k\sigma}(t) \mathbf{e}^*_{k\sigma} e^{-\imath \boldsymbol{k}\cdot\mathbf{r}}. \tag{2.34}$$

The quantum limit of Eq. (2.34) is obtained by the following substitutions:

$$a_{k\sigma} \to \sqrt{\frac{\hbar}{2\varepsilon_0 V \omega_{\boldsymbol{k}}}} \hat{a}_{k\sigma} \tag{2.35}$$

$$a^*_{k\sigma} \to \sqrt{\frac{\hbar}{2\varepsilon_0 V \omega_{\boldsymbol{k}}}} \hat{a}^\dagger_{k\sigma}, \tag{2.36}$$

where the operators $\hat{a}_{k\sigma}$ and $\hat{a}^\dagger_{k\sigma}$ are subject to the commutator rules:

$$\left[\hat{a}_{k\sigma}\,,\, \hat{a}^\dagger_{k'\sigma'}\right] = \delta_{kk'}\delta_{\sigma\sigma'} \tag{2.37}$$

$$[\hat{a}_{k\sigma}\,,\,\hat{a}_{k'\sigma'}] = \left[\hat{a}^{\dagger}_{k\sigma}\,,\,\hat{a}^{\dagger}_{k'\sigma'}\right] = 0. \tag{2.38}$$

The operators $\hat{a}_{k\sigma}$ and $\hat{a}^{\dagger}_{k\sigma}$ are nothing but the bosonic annihilation and creation operators for a field mode $(\boldsymbol{k}, \sigma)$, respectively. Their action is defined by:

$$\hat{a}_{k\sigma}|n_{k\sigma}\rangle = \sqrt{n_{k\sigma}}|n_{k\sigma} - 1\rangle, \tag{2.39}$$

$$\hat{a}^{\dagger}_{k\sigma}|n_{k\sigma}\rangle = \sqrt{n_{k\sigma} + 1}|n_{k\sigma} + 1\rangle. \tag{2.40}$$

The reason why the Fourier coefficients in classical theory should be replaced by photon creation and annihilation operators can be seen by examining the classical Hamiltonian of the EM field:

$$\mathbb{H} = \frac{1}{2}\int d^3\mathbf{r}\left[\varepsilon_0\mathbf{E}^2 + \mathbf{B}^2/\mu_0\right] = \sum_{\boldsymbol{k}}\sum_{\sigma}\mathbb{H}_{k\sigma} = 2V\varepsilon_0\sum_{\boldsymbol{k}}\sum_{\sigma}a_{k\sigma}(t)a^{*}_{k\sigma}(t). \tag{2.41}$$

The second equality in Eq. (2.41) follows, after some work, from the orthogonality of the different modes. By introducing the conjugate position and momentum $q_{k\sigma}$ and $p_{k\sigma}$:

$$q_{k\sigma}(t) = \sqrt{V\varepsilon_0}\,[a_{k\sigma}(t) + a_{k\sigma}(t)^{*}] \tag{2.42}$$

$$p_{k\sigma}(t) = -\imath\omega_k\sqrt{V\varepsilon_0}\,[a_{k\sigma}(t) - a_{k\sigma}(t)^{*}]\,, \tag{2.43}$$

the classical Hamiltonian takes a form:

$$\mathbb{H}_{k\sigma} = \frac{1}{2}\left[p^2_{k\sigma}(t) + \omega^2_{bk}q_{k\sigma}(t)^2\right]. \tag{2.44}$$

This expression is similar to the Hamiltonian of a harmonic oscillator, whose quantum description features the creation and annihilation operators in a similar fashion. Following the definitions in Eq. (2.35) and Eq. (2.36), the quantum mechanical operators for the field and the Hamiltonian are:

$$\hat{\mathbf{A}}(\mathbf{r}) = \sum_{\boldsymbol{k}}\sum_{\sigma}\sqrt{\frac{\hbar}{2\varepsilon_0 V\omega_{\boldsymbol{k}}}}\left(\hat{a}_{k\sigma}\mathbf{e}_{k\sigma}e^{\imath\boldsymbol{k}\cdot\mathbf{r}} + \hat{a}^{\dagger}_{k\sigma}\mathbf{e}^{*}_{k\sigma}e^{-\imath\boldsymbol{k}\cdot\mathbf{r}}\right) \tag{2.45}$$

and

$$\hat{H}_{\text{rad}} = \sum_{\boldsymbol{k}} \sum_{\sigma} \hat{H}_{\boldsymbol{k}\sigma} = \sum_{\boldsymbol{k}} \sum_{\sigma} \hbar\omega_{\boldsymbol{k}} \left(\hat{a}^{\dagger}_{\boldsymbol{k}\sigma} \hat{a}_{\boldsymbol{k}\sigma} + \frac{1}{2} \right). \tag{2.46}$$

Note that in Eq. (2.45) and Eq. (2.46) the creation and annihilation operators are no longer time-dependent in accordance with the Schrödinger representation, in which the time-dependence is carried by the wave function, not by the operators. The time-dependence of the operators, specified by analogy to Eq. (2.33), is restored in the Heisenberg representation,[2] which appears to be the natural representation when transitioning to the classical limit.

2.5 Interaction Hamiltonian

Having established a quantum mechanical description of both light and matter, we move on to see how they interact. In that case, the total composite Hamiltonian of the system is given by three terms:

$$\hat{H} = \hat{H}_{\text{mol}} + \hat{H}_{\text{rad}} + \hat{H}_{\text{int}}, \tag{2.47}$$

where the terms from left to right are the molecular Hamiltonian, which is discussed in more detail in Section 2.7, the radiation Hamiltonian, given by Eq. (2.46), and an interaction term, which is assumed to be small. The eigenstates of the full Hamiltonian are then described by $|\text{mol}\rangle \otimes |\text{rad}\rangle$, sometimes abbreviated as $|\text{mol}, \text{rad}\rangle$. To find out the form of the interaction Hamiltonian, we use a minimal coupling procedure and substitute the momentum of a particle with charge q_i by $\mathbf{p}_i \rightarrow \mathbf{p}_i - q_i \hat{\mathbf{A}}(\mathbf{r}_i)$. The kinetic terms (nuclear and electronic) in the molecular Hamiltonian then become:

$$\hat{H}_{\text{kin}} = \sum_{i=1}^{N_{\text{en}}} \frac{1}{2m_i} (\hat{\mathbf{p}}_i - q_i \hat{\mathbf{A}}(\mathbf{r}_i))^2 = \sum_{i=1}^{N_{\text{en}}} \frac{1}{2m_i} (\hat{\mathbf{p}}_i^2 - 2q_i \hat{\mathbf{A}}(\mathbf{r}_i) \cdot \hat{\mathbf{p}}_i + q_i^2 \hat{\mathbf{A}}^2(\mathbf{r}_i)), \tag{2.48}$$

[2] In the Heisenberg representation, the time evolution is carried by the operators, while the wave functions are time-independent. Formal definition of the operators with respect to the Schrödinger representation is achieved by $\hat{A}_{\text{H}} = e^{\imath \hat{H} t/\hbar} \hat{A}_{\text{S}} e^{-\imath \hat{H} t/\hbar}$, where $\hat{H}$ is the Hamiltonian of the system.

where we have used the fact that the momentum and the radiation field operators commute in the Coulomb gauge. The first term in Eq. (2.48) is simply the combined kinetic energy of all particles. The interaction of the molecule with the electromagnetic field is then given by:

$$\hat{H}_{\text{int}} = \sum_{i=1}^{N_{\text{en}}} \frac{1}{2m_i} (q_i^2 \hat{\mathbf{A}}^2(\mathbf{r}_i) - 2q_i \hat{\mathbf{A}}(\mathbf{r}_i) \cdot \hat{\mathbf{p}}_i). \tag{2.49}$$

In the above description, we have omitted the interaction of the magnetic field of light with the spin of the particles in the molecule. Note that Eq. (2.49) does not depend on time as implied by the Schrödinger representation of the operator.

2.6 Photoexcitation

In this section, we consider the process of photoexcitation. The theoretical framework follows partially Ref. [55] and Ref. [56]. For simplicity we will consider a single-mode state of radiation. If initially there are n photons defined by momentum $\boldsymbol{k}$ and polarisation σ, the corresponding (Fock) eigenstate of the radiation Hamiltonian is $|n_{\boldsymbol{k}\sigma}\rangle$. Furthermore, let us assume that the molecule exists in an initial state $|i\rangle$, normally the ground state before excitation. The molecular wave function is then $|i\rangle = |\chi_i\rangle|\psi_i(\bar{\mathbf{R}})\rangle$, where $|\chi_i\rangle$ is the nuclear and $|\psi_i(\bar{\mathbf{R}})\rangle$ is the electronic wave function (see also Section 2.7). Absorption of light is then associated with removal of a photon so that the final radiation state is going to be $|n_{\boldsymbol{k}\sigma} - 1\rangle$. We want to find out what the probability of finding the molecule in another electronic state f at time t is going to be. Using Eq. (2.18), the amplitude in first order perturbation theory is given by:

$$S_{\text{abs}} = -\frac{\iota}{\hbar} \int_{-\infty}^{\infty} dt' e^{\iota(\omega_f - \omega_i - \omega_{\boldsymbol{k}})t'} \langle f, n_{\boldsymbol{k}\sigma} - 1 | \hat{H}_{\text{int}} | n_{\boldsymbol{k}\sigma}, i \rangle, \tag{2.50}$$

where $\omega_f = E_f/\hbar$ and $\omega_i = E_i/\hbar$. Comparing with Eq. (2.18), the zeroth-order contribution to the amplitude in Eq. (2.50) disappears because of the

orthogonality of the number states of the electromagnetic field. As the interaction Hamiltonian is time-independent, the matrix element in Eq. (2.50) can be taken outside the integral. We then notice that the time integration reduces to a delta function. With that, the transition rate that corresponds to this amplitude is:

$$\Gamma_{\text{abs}} = \frac{|S_{\text{abs}}|^2}{T} = \frac{2\pi}{\hbar^2}|\langle f, n_{k\sigma} - 1|\hat{H}_{\text{int}}|n_{k\sigma}, i\rangle|^2 \delta(\omega_f - \omega_i - \omega_{\boldsymbol{k}}), \tag{2.51}$$

where we let $T \to \infty$ and used the trick:

$$\delta^2(\omega) = \delta(\omega) \lim_{T\to\infty} \int_{-T/2}^{T/2} \frac{dt'}{2\pi} e^{\imath\omega t'} = \delta(\omega) \lim_{T\to\infty} \frac{T}{2\pi}, \tag{2.52}$$

with $\omega = \omega_f - \omega_i - \omega_{\boldsymbol{k}}$. Eq. (2.51) is nothing but the famous Fermi's golden rule. To deal with the matrix element of the interaction Hamiltonian between the initial and the final states, first we need to note that the $\hat{\mathbf{A}}^2$ term in Eq. (2.49) changes the total number of photons by 0 or 2 so it is not responsible for absorption. Hence, using Eq. (2.45) we have:

$$\langle f, n_{k\sigma} - 1|\hat{H}_{\text{int}}|n_{k\sigma}, i\rangle = \frac{-e}{m_{\text{e}}} \sqrt{\frac{\hbar n_{k\sigma}}{2\varepsilon_0 V \omega_{\boldsymbol{k}}}} \sum_{\alpha=1}^{N_{\text{e}}} \langle f|e^{\imath \boldsymbol{k}\cdot\mathbf{r}_\alpha} \mathbf{e}_{k\sigma} \cdot \hat{\mathbf{p}}_\alpha|i\rangle, \tag{2.53}$$

where the nuclei can be excluded from the sum on account of their mass being much larger than the mass of the electron m_{e}. The electron charge is $-e$. In order to simplify further, we note that in the optical regime the typical wavelength of light is much larger than the size of the atom. That implies that we can approximate $e^{\imath \boldsymbol{k}\cdot\mathbf{r}_\alpha}$ to unity. This is known as the dipole approximation for reasons that will now become evident. We use the commutator relation:

$$\hat{\mathbf{p}}_\alpha = \imath \frac{m_\alpha}{\hbar} \left[\hat{H}_{\text{mol}}, \hat{\mathbf{r}}_\alpha\right], \tag{2.54}$$

to rewrite Eq. (2.53) as:

$$\langle f, n_{k\sigma} - 1|\hat{H}_{\text{int}}|n_{k\sigma}, i\rangle = -\imath \frac{e}{\hbar} \sqrt{\frac{\hbar n_{k\sigma}}{2\varepsilon_0 V \omega_{\boldsymbol{k}}}} (\omega_f - \omega_i) \mathbf{e}_{k\sigma} \cdot \langle f| \sum_{\alpha=1}^{N_{\text{e}}} \hat{\mathbf{r}}_\alpha |i\rangle. \tag{2.55}$$

Using the definition of the molecular wave function in terms of nuclear, $|\chi_i\rangle$, and electronic, $|\psi_i(\bar{\mathbf{R}})\rangle$, components, we can rewrite the previous equation as:

$$\langle f, n_{k\sigma} - 1|\hat{H}_{\text{int}}|n_{k\sigma}, i\rangle = -\iota\frac{e}{\hbar}\sqrt{\frac{\hbar n_{k\sigma}}{2\varepsilon_0 V\omega_{\boldsymbol{k}}}}(\omega_f - \omega_i)\mathbf{e}_{k\sigma}\cdot\langle\chi_f|\boldsymbol{\mu}_{fi}(\bar{\mathbf{R}})|\chi_i\rangle, \tag{2.56}$$

where we have introduced the molecular electronic transition dipole moment (TDM):

$$\boldsymbol{\mu}_{fi}(\bar{\mathbf{R}}) = \langle\psi_f(\bar{\mathbf{R}})|\sum_{\alpha}^{N_e}\hat{\mathbf{r}}_\alpha|\psi_i(\bar{\mathbf{R}})\rangle. \tag{2.57}$$

Going back to the expression for the Fermi's golden rule in Eq. (2.51), we see that the transition rate is now given by:

$$\Gamma_{\text{abs}} \propto \left|\langle\chi_f|\mathbf{e}_{k\sigma}\cdot\boldsymbol{\mu}_{fi}(\bar{\mathbf{R}})|\chi_i\rangle\right|^2. \tag{2.58}$$

Eq. (2.58) shows that the transition rate depends on the magnitude and orientation of the TDM between the initial and final electronic states. This is the essence of the dipole approximation. Going further, we can write the nuclear wave function as a product of a rotational, $|\theta_i^{\text{r}}\rangle$, and a vibrational wave function, $|\chi_i^{\text{v}}\rangle$. In addition, it is often reasonable to treat the electronic TDM as independent of the nuclear coordinates for small displacement around the equilibrium geometry of the molecule in the ground state. This is known as the Franck-Condon approximation, in which the transition rate is proportional to the square of the overlap between the vibrational wave functions on the initial and final electronic states:

$$\Gamma_{\text{abs}} \propto \left|\langle\chi_f^{\text{v}}|\chi_i^{\text{v}}\rangle\right|^2\left|\langle\theta_f^{\text{r}}|\mathbf{e}_{k\sigma}\cdot\boldsymbol{\mu}_{fi}|\theta_i^{\text{r}}\rangle\right|^2. \tag{2.59}$$

In the classical limit of rotational motion, Eq. (2.59) readily shows that the probability of absorption of linearly polarised light is proportional to the cosine squared of the angle between the laser polarisation axis and the TDM to the excited state resonant with the EM field, *e.g.* $|\mathbf{e}_{k\sigma}\cdot\boldsymbol{\mu}_{fi}|^2 = \cos^2\theta$. As the TDM is fixed in the molecular frame, the electric dipole excitation

also amounts to preferential distribution of the molecular axes in space [57]. The manifestation of this anisotropy in the context of UXS is going to be discussed in Chapter 5 and Section 3.2.

We now move on to examine more carefully the alignment of the molecule from the perspective of the rotational wave function. We aim to answer the questions – which rotational eigenstates have an appreciable chance of leading to electronic excitation, and what is the angular distribution resulting from their superposition. The treatment below closely follows Ref. [58] and Ref. [59]. Assuming linearly polarised light and taking the polarisation vector of the EM field as the laboratory $\hat{\mathbf{Z}}$ axis, we have that $\mathbf{e}_{k\sigma} \cdot \boldsymbol{\mu}_{fi} = \mu_Z$, where μ_Z is the Z-component of the TDM. However, the TDM in Eq. (2.57) is an intrinsic property of the molecule and is most naturally evaluated in the molecular frame. The two frames are related by the Euler angles, $\alpha\beta\gamma$. The connection between the components of the TDM in the two reference frames is given by the Wigner D-matrix, a function of the Euler angles, as follows:

$$\mu_Z = \sum_{p}^{-1,0,1} D^1_{0,p} \mu^1_p \,, \tag{2.60}$$

where we use a spherical representation for μ_x, μ_y and μ_z, the components of the TDM in the molecular frame:

$$\begin{aligned} \mu^1_0 &= \mu_z \\ \mu^1_{\pm 1} &= \mp \frac{1}{\sqrt{2}} (\mu_x \pm \imath \mu_y). \end{aligned} \tag{2.61}$$

For simplicity, let us assume that the molecule is a symmetric top. The symmetry of the molecule then restricts the allowed transitions to either parallel ($p = 0$) or perpendicular ($p = \pm 1$). In reference to Eq. (2.59), the probability amplitude of transitions between a rotational eigenstate on the ground electronic state, $|J_0 K_0 M_0\rangle$, specified by quantum numbers J_0, K_0 and M_0, and rotational eigenstate on the excited electronic state, $|JKM\rangle$, is given by:

$$c_{JKM \leftarrow J_0 K_0 M_0} = \langle JKM | \mathbf{e}_{k\sigma} \cdot \boldsymbol{\mu}_{fi} | J_0 K_0 M_0 \rangle = \sum_{p}^{-1,0,1} \langle JKM | D^1_{0,p} \mu^1_p | J_0 K_0 M_0 \rangle. \tag{2.62}$$

Using the explicit form of the rotational eigenstates:

$$|JKM\rangle = \left[\frac{2J+1}{8\pi^2}\right]^{1/2} D^{J*}_{M,K}(\alpha,\beta,\gamma) \tag{2.63}$$

we can evaluate the probability amplitude as follows:

$$\begin{aligned} c_{JKM\leftarrow J_0K_0M_0} &= \sum_p^{-1,0,1} \mu_p^1 \left[\frac{2J+1}{8\pi^2}\right]^{1/2} \left[\frac{2J_0+1}{8\pi^2}\right]^{1/2} \int d\Omega\, D^J_{M,K} D^{1*}_{0,p} D^{J_0*}_{M_0,K_0} \\ &= \sum_p^{-1,0,1} \mu_p^1 \left[\frac{2J+1}{8\pi^2}\right]^{1/2} \left[\frac{2J_0+1}{8\pi^2}\right]^{1/2} \left[\int d\Omega\, D^{J*}_{M,K} D^{1}_{0,p} D^{J_0}_{M_0,K_0}\right]^* \\ &= \sum_p^{-1,0,1} \mu_p^1 \left[\frac{2J_0+1}{2J+1}\right]^{1/2} \langle J_0M_0, 10|JM\rangle \langle J_0K_0, 1p|JK\rangle. \end{aligned} \tag{2.64}$$

In Eq. (2.64), the angular integral over the D-matrices is evaluated as products of two Clebsch–Gordan coefficients as detailed in standard textbooks on angular momentum [58]. The experiments described in this thesis are performed in gas phase, at or close to room temperature, and without alignment of the molecules in the ground state. Hence, the corresponding ground state rotational wave packet is an incoherent sum over $|J_0K_0M_0\rangle$, where different M_0 states are equally populated (isotropic distribution of states):

$$|\theta_i^{\mathrm{r}}\rangle = \sum_{J_0K_0M_0} w_{J_0K_0M_0} |J_0K_0M_0\rangle, \tag{2.65}$$

where the coefficients $w_{J_0K_0M_0}$ contain a random phase factor that ensures the sum is incoherent. The combined probability amplitude of excitation to $|JKM\rangle$ is then given by:

$$c_{JKM} = \sum_{J_0K_0M_0} w_{J_0K_0M_0} \sum_p^{-1,0,1} \mu_p^1 \left[\frac{2J_0+1}{2J+1}\right]^{1/2} \langle J_0M_0, 10|JM\rangle \langle J_0K_0, 1p|JK\rangle. \tag{2.66}$$

Now we can write the excited state angular distribution, $P(\beta)$, as:

$$\begin{aligned} P(\beta) &= \left| \sum_{JKM} c_{JKM} |JKM\rangle \right|^2 \\ &= \left| \sum_{JKM} c_{JKM} \left[\frac{2J+1}{8\pi^2} \right]^{1/2} D^{J*}_{M,K} \right|^2 \\ &= \left| \sum_{J_0K_0M_0} w_{J_0K_0M_0} \sum_{p}^{-1,0,1} \mu^1_p \sqrt{\frac{2J_0+1}{8\pi^2}} \sum_{JKM} \langle J_0M_0, 10|JM\rangle \langle J_0K_0, 1p|JK\rangle D^{J*}_{M,K} \right|^2 . \end{aligned} \tag{2.67}$$

To simplify further, we can use the Clebsch-Gordon series:

$$\sum_J \langle j_1m_1, j_2m_2|JM\rangle \langle j_1k_1, j_2k_2|JK\rangle D^J_{KM} = D^{j_1}_{k_1m_1} D^{j_2}_{k_2m_2}. \tag{2.68}$$

This allows us to eliminate the Clebsch-Gordon coefficients from Eq. (2.67):

$$P(\beta) = \left| \sum_{J_0K_0M_0} w_{J_0K_0M_0} \sqrt{\frac{2J_0+1}{8\pi^2}} \sum_{p}^{-1,0,1} \mu^1_p D^{1*}_{p0} D^{J_0*}_{K_0M_0} \right|^2, \tag{2.69}$$

where we have removed the redundant summations. Performing the sum incoherently leads to:

$$P(\beta) = \sum_{J_0K_0} P_{J_0K_0} \frac{2J_0+1}{8\pi^2} \sum_{p}^{-1,0,1} |\mu^1_p|^2 |D^1_{p0}|^2 \sum_{M_0} |D^{J_0}_{K_0M_0}|^2, \tag{2.70}$$

where we have used the fact that all M_0 states have equal probability, *e.g.* $P_{J_0K_0} = |w_{J_0K_0M_0}|^2$. Going further, we note that $\sum_{M_0} |D^{J_0}_{K_0M_0}|^2 = 1$, because the rotational matrices are unitary. Finally, expressing the angular distribution in terms of the small Wigner D-matrices, $d^J_{MK}(\beta)$, we have:

$$P(\beta) \propto \sum_{p}^{-1,0,1} |\mu^1_p|^2 |d^1_{p0}|^2 \propto \begin{cases} \cos^2\beta, & \text{parallel transition } (p=0) \\ \sin^2\beta, & \text{perpendicular transition } (p=\pm1) \end{cases} . \tag{2.71}$$

The orientation of the TDM uniquely specifies the alignment of the molecular axes. The lack of phase relation between the different M_0 states and their equal weight effectively reduce the quantum treatment to a result equivalent to the classical limit. Eq. (2.71) does not carry dependence on the quantum numbers but solely depends on the orientation of the TDM in the molecular frame. As well as to symmetric tops, the result is also applicable to linear molecules. Extension of this quantum treatment is also possible to asymmetric top molecules [59]. It should be pointed out that, the dipole excitation also creates a "hole" in the ground electronic state probability, which means that the ground state molecules also exhibit preferential alignment after the photoexcitation.

By assuming a single mode of the EM radiation, we have implicitly ignored the time-dependence of the excitation pulse. In reality, the laser that initiates the photochemical reaction in pump-probe experiments is always pulsed and characterised by a finite envelope in time. After the pulse has passed, the interaction term in the total Hamiltonian vanishes, and the molecular motion is solely governed by the molecular Hamiltonian, which is discussed in more detail in the following section. Both the vibrational and the rotational wave packets of the molecules begin to evolve.

2.7 The Molecular Hamiltonian

The molecular Hamiltonian is a fascinating subject of pivotal importance to all branches of chemistry. Various levels of approximations applicable in different regimes have been devised since quantum mechanics first appeared. This section summarises some of the important concepts without attempting to be all-encompassing. A structured discussion on the subject of the molecular Hamiltonian can be found in many standard textbooks such as Ref. [60]. For the purposes of this work, a general form of the molecular Hamiltonian in the laboratory frame of reference is given by:

$$\hat{H}_{\mathrm{mol}} = \hat{T}_{\mathrm{n}}(\bar{\mathbf{R}}) + \hat{V}_{\mathrm{n}}(\bar{\mathbf{R}}) + \hat{T}_{\mathrm{e}}(\bar{\mathbf{r}}) + \hat{V}_{\mathrm{e}}(\bar{\mathbf{r}}) + \hat{V}_{\mathrm{en}}(\bar{\mathbf{R}}, \bar{\mathbf{r}}) + \hat{H}_{\mathrm{cor}}(\bar{\mathbf{R}}, \bar{\mathbf{r}}), \quad (2.72)$$

where $\bar{\mathbf{r}} = \{\mathbf{r}_1, \mathbf{r}_2, ...\mathbf{r}_{N_e}\}$ and $\mathbf{R} = \{\mathbf{R}_1, \mathbf{R}_2, ..., \mathbf{R}_{N_n}\}$ are the coordinates of the N_e electrons and the N_n nuclei, respectively, and the operators correspond (from left to right) to the nuclear kinetic energy, nuclear-nuclear repulsion, electron kinetic energy, electron-electron repulsion, electron-nuclear interaction, and a relativistic correction term. The final term describes a series of effects divided into spin-dependent and scalar relativistic corrections.[3] While most of those would only have niche applications, the electron SOC becomes sizeable for heavy atoms and could also have a non-negligible manifestation in the context of photochemical reactions of light molecules where it is responsible for ISC. Nevertheless, examples of strong SOC are not encountered in the following chapters, so the correction term in Eq. (2.72) is going to be omitted altogether. The remaining terms are often collectively referred to as the Molecular Coulomb Hamiltonian.

Approaching Eq. (2.72) in the general case poses challenges and to tackle this many-body problem, sensible approximations are needed. Given the large difference between the nuclear and electron mass, it is natural to seek an approach that allows us to treat separately the two sets of coordinates. The first step would then be to define a clamped-nuclei electronic Hamiltonian, $\hat{H}_e$, that contains all terms from the molecular Hamiltonian except the nuclear kinetic energy. The $\hat{H}_e$ can be evaluated numerically in an *ab initio* electronic structure calculation, where the nuclear positions are held fixed, hence the name clamped-nuclei Hamiltonian. In other words, the electronic Hamiltonian has only parametric dependence on the nuclear coordinates. The corresponding eigenvalue equation is:

$$\hat{H}_e|\psi_i(\bar{\mathbf{R}})\rangle = V_i(\bar{\mathbf{R}})|\psi_i(\bar{\mathbf{R}})\rangle, \tag{2.73}$$

where $|\psi_i(\bar{\mathbf{R}})\rangle$ is i^{th} electronic eigenstate and $V_i(\bar{\mathbf{R}})$ is the electronic energy, which both carry the above-mentioned parametric dependence on the nuclear coordinates. An overview of the methods used in this thesis to solve the electronic problem is given in Section 4.2.

[3] The origin of these correction terms can be traced to the solution of the Dirac-Coulomb or Dirac-Coulomb-Breit equation by means of various reduction schemes [61].

As a side note, it should be pointed out that the clamped-nuclei Hamiltonian is already an approximation. While it is a well-defined Hamiltonian on its own right, it is only a convenient way to approach the problem of separating nuclei and electrons. The correct treatment would first involve a separation of the centre of mass of the molecule and then choosing a suitable set of internal coordinates to express the Hamiltonian. The discrepancies between the full-electronic Hamiltonian and the clamped-nuclei one are discussed in Ref. [62]. Only a small number of examples of the full treatment exist in the literature and they are restricted to small molecules [63–65].

Once the eigenstates of the electronic Hamiltonian are known, we write the total wave function of the molecular Hamiltonian as a Born-Huang expansion over the electronic states of the molecule [66]:

$$|\Psi(\bar{\mathbf{R}},t)\rangle = \sum_{i=1}^{\infty} |\chi_i(t)\rangle|\psi_i(\bar{\mathbf{R}})\rangle. \tag{2.74}$$

In Eq. (2.74), the nuclear wave packet, $|\chi_i(t)\rangle$, fulfils the role of a time-dependent expansion coefficient. Introducing Eq. (2.74) into the TDSE with $\hat{H} = \hat{T}_\mathrm{n} + \hat{H}_\mathrm{e}$ results in:

$$\imath\hbar \sum_{i}^{\infty} \frac{\partial|\chi_i(t)\rangle}{\partial t}|\psi_i(\bar{\mathbf{R}})\rangle = \big(\hat{T}_\mathrm{n} + \hat{H}_\mathrm{e}\big) \sum_{i=1}^{\infty} |\chi_i(t)\rangle|\psi_i(\bar{\mathbf{R}})\rangle.$$

Multiplying from the left by $\langle\psi_j(\bar{\mathbf{R}})|$ yields:

$$\imath\hbar\frac{\partial|\chi_j(t)\rangle}{\partial t} = \sum_{i=1}^{\infty}\langle\psi_i(\bar{\mathbf{R}})|\hat{T}_\mathrm{n}|\chi_i(t)\rangle|\psi_i(\bar{\mathbf{R}})\rangle + V_j(\bar{\mathbf{R}})|\chi_j(t)\rangle,$$

where we have used Eq. (2.73) and the orthogonality of the electronic wave functions. Now, using the form of the nuclear kinetic energy operator,

$$\hat{T}_\mathrm{n} = -\sum_{a=1}^{N_\mathrm{n}} \frac{\hbar^2}{2m_a}\nabla_a^2\,, \tag{2.75}$$

and by expanding through the derivatives of the nuclear coordinates, we arrive at:

$$\imath\hbar\frac{\partial|\chi_j(t)\rangle}{\partial t} = \left(\hat{T}_{\mathrm{n}} + V_j(\bar{\mathbf{R}})\right)|\chi_j(t)\rangle - \sum_{i=1}^{\infty}\hat{C}_{ji}|\chi_i(t)\rangle, \tag{2.76}$$

where

$$\hat{C}_{ji} = \sum_{a=1}^{N_{\mathrm{n}}}\frac{\hbar^2}{2m_a}\left(2\underbrace{\langle\psi_j(\bar{\mathbf{R}})|\nabla_a|\psi_i(\bar{\mathbf{R}})\rangle}_{A_{jai}}\nabla_a + \underbrace{\langle\psi_j(\bar{\mathbf{R}})|\nabla_a^2|\psi_i(\bar{\mathbf{R}})\rangle}_{B_{jai}}\right). \tag{2.77}$$

The two terms, $A_{jai}(\bar{\mathbf{R}})$ and $B_{jai}(\bar{\mathbf{R}})$, are referred to as derivative and scalar non-adiabatic coupling matrix elements (NACMEs), respectively. Their importance lies in the fact that their off-diagonal terms couple nuclear wave packets that propagate on different electronic states. In other words, they are responsible for IC (similarly, they describe ISC in the presence of SOC).

It is instructive to show the behaviour of the derivative NACME. Straightforward application of the off-diagonal Hellmann-Feynman theorem [67] shows that: [4]

$$A_{jai}(\bar{\mathbf{R}}) = \frac{\langle\psi_j(\bar{\mathbf{R}})|(\nabla_a\hat{H}_e)|\psi_i(\bar{\mathbf{R}})\rangle}{V_j(\bar{\mathbf{R}}) - V_i(\bar{\mathbf{R}})}. \tag{2.78}$$

Now it can be seen that the coupling depends inversely on the gap between energy levels. While for well-separated energy surfaces, the term is negligibly small, in regions where the gap narrows the coupling could be substantial even for heavy nuclei. The ground state is usually separated from the excited states by a large energy gap at the molecular equilibrium geometry so it is safe to assume that there is no appreciable coupling in the case of ground-state chemistry. However, after photoexcitation the molecule exists in one or more excited states, which could be coupled somewhere along their PESs. The excess energy provided by the photon absorbed can be transformed into kinetic energy to explore the PES. When such a coupling region is encountered, a nonradiative population transfer can occur

[4] The proof of the theorem is simple; it starts from the derivative of $\langle\psi_j|\hat{H}|\psi_i\rangle$.

between the electronic states. Such regions are the conical intersections and avoided crossings.

Ignoring the coupling between different states in Eq. (2.77) constitutes the adiabatic approximation, and results in an equation of motion of the form:

$$\imath\hbar\frac{\partial|\chi_j(t)\rangle}{\partial t} = \left(\hat{T}_\mathrm{n} + V_j(\bar{\mathbf{R}}) + \sum_{a=1}^{N_\mathrm{n}} \frac{\hbar^2}{2m_a} B_{jaj}(\bar{\mathbf{R}})\right)|\chi_j(t)\rangle. \tag{2.79}$$

Note that the diagonal terms $A_{jaj}(\bar{\mathbf{R}})$ are zero because the derivative operator is anti-Hermitian. Now we can appreciate that the second and the third term in Eq. (2.79) collectively play the role of an adiabatic potential for the nuclear propagation. Further simplification can be achieved if one ignores the diagonal scalar coupling, which is generally small. This amounts to removing the effect of the electronic wave function on the nuclear momentum. The resulting equation,

$$\imath\hbar\frac{\partial|\chi_j(t)\rangle}{\partial t} = \left(\hat{T}_\mathrm{n} + V_j(\bar{\mathbf{R}})\right)|\chi_j(t)\rangle, \tag{2.80}$$

appears similar to the TDSE, and provides the solution for the nuclear motion. The potential is solely provided by the solution of the electronic Hamiltonian. Eq. (2.80) is the result that Born and Oppenheimer reached in their original perturbation theory treatment [12]. The equation has solutions of the form $|\chi_j(t)\rangle|\psi_j(\bar{\mathbf{R}})\rangle$, *e.g.* the electron and nuclear motion have been decoupled.

The Born-Oppenheimer approximation (BOA) is a fundamental achievement that has propelled the field of chemistry since it first came to light. However, the dynamics seen after photoexcitation are inherently non-adiabatic, that is, the different electronic states are coupled somewhere along the PESs. UXS is one experimental technique that provides the means of observing this complicated motion, where nuclear and electronic degrees of freedom are intertwined. Unlike crystallography or ground state scattering, the molecule now exists as a superposition of electronic states. The next section aims to provide the theoretical description of how the excited molecule interacts with a short probe pulse of X-ray radiation. While the physics is

not new, special attention is given to the role of electronic states and the time dependence of the recorded signal.

2.8 X-ray Scattering

In the classical treatment of scattering, molecules and atoms are treated as a non-reactive time-independent potential in the Schrödinger equation of the scattered particle. Here, we seek a more detailed solution of the X-ray scattering problem that fully accounts for the quantum nature of both X-ray photons and molecules. The final goal is to derive a formula similar to the famous Kramers-Heisenberg formula but beyond the dipole approximation (the relevant regime for X-ray scattering), and which accounts for the time-evolution of the system and the X-ray profile. The treatment of the X-ray field follows closely Ref. [68] and Ref. [69], while the general methodology borrows ideas from Ref. [70] and Ref. [71].

The non-resonant scattering of X-rays from matter can be understood as a momentum transfer process. In the framework of quantum electrodynamics (QED), this is equivalent to the annihilation of a photon in an initial state, $|\boldsymbol{k}_0\sigma_0\rangle$, and the creation of another photon in a state $|\boldsymbol{k}_s\sigma_s\rangle$. Without a loss of generality, we can assume that the final state of the detected photon is a single-photon Fock state. We will take care to integrate over all possible such photons in the calculation of the differential scattering cross-section. On the other hand, the incoming XFEL field is pulsed and has a well-defined polarisation axis. It is then appropriate to choose a single-photon localised multi-mode state [68],

$$|\boldsymbol{k}_0\sigma_0\rangle = \sum_{\boldsymbol{k}} c_{\boldsymbol{k}} |\boldsymbol{k}\sigma_0\rangle, \tag{2.81}$$

so that the expansion coefficients have a narrow spread around $\boldsymbol{k}_0$ and are normalised to unity, $\sum_{\boldsymbol{k}} |c_{\boldsymbol{k}}|^2 = 1$. The states, $|\boldsymbol{k}\sigma_0\rangle$, have the same polarisation and direction of propagation but different angular frequencies, $\omega_{\boldsymbol{k}} = c|\boldsymbol{k}|$. In accordance with Eq. (2.17) and Eq. (2.18), the probability amplitude, $S_{f\Psi}$, of a scattering event to a final eigenstate of the material system,

f, is:

$$\begin{aligned} S_{f\Psi}(t) = &\sum_{\boldsymbol{k}} c_{\boldsymbol{k}} \langle f(t)|\Psi(t)\rangle \langle \boldsymbol{k}_s \sigma_s(t)|\boldsymbol{k}\sigma_0(t)\rangle \\ &- \frac{\iota}{\hbar}\int_{t_0}^{t} dt' \langle f(t)|\hat{U}_0(t,t')\hat{O}(t')\hat{U}_0(t',t_0)|\Psi(t_0)\rangle, \end{aligned} \tag{2.82}$$

where $\Psi(t_0)$ is the superposition of molecular eigenstates prepared by the pump laser, $\hat{U}_0(t,t')$ is the time-evolution operator of the molecular system, and $\hat{O}(t')$ is the perturbation operator for the material system. The latter is obtained by resolving through the sub-space of the EM radiation:

$$\begin{aligned} \hat{O}(t') &= \sum_{\boldsymbol{k}} c_{\boldsymbol{k}} \langle \boldsymbol{k}_s \sigma_s(t)|\hat{U}_{0,\mathrm{EM}}(t,t')\hat{H}_{\mathrm{int}}\hat{U}_{0,\mathrm{EM}}(t',t_0)|\boldsymbol{k}\sigma_0(t_0)\rangle \\ &= \sum_{\boldsymbol{k}} c_{\boldsymbol{k}} e^{\iota(\omega_{\boldsymbol{k}_s}-\omega_{\boldsymbol{k}})t'} \langle \boldsymbol{k}_s \sigma_s|\hat{H}_{\mathrm{int}}|\boldsymbol{k}\sigma_0\rangle, \end{aligned} \tag{2.83}$$

where $\hat{U}_{0,\mathrm{EM}}(t',t_0)$ is the time-evolution operator of the EM field. We note that the first term in Eq. (2.82) is zero if the momentum vector of the scattered photon is significantly different from that of the incoming X-ray beam. In practice, in the direction of the X-ray beam it describes transmission and phase contrast and, hence, does not contribute to scattering. In order to deal with the second term in Eq. (2.82), we examine the behaviour of the terms present in the interaction Hamiltonian specified by Eq. (2.49). The absorption term, $\hat{\mathbf{A}}(\mathbf{r}_i)\cdot\hat{\mathbf{p}}_i$, changes the total number of photons by one so it cannot be responsible for scattering in first order as the number of photons needs to be conserved. In second-order TDPT, it gives rise to resonant scattering but this effect is negligible away from atomic absorption edges in the hard X-ray regime. That means that only the $\hat{\mathbf{A}}^2(\mathbf{r}_i)$ term in Eq. (2.49) needs to be considered. With reference to Eq. (2.45), taking the square of the potential operators leads to four terms, two of which do not conserve the number of photons, and should be ignored again. The remaining two terms form a symmetric sum under exchange of indices, a manifestation of the bosonic symmetry under particle exchange, so that the interaction Hamiltonian can

be rewritten as:

$$\begin{aligned}\hat{H}_{\text{int}} = \sum_{i=1}^{N_{\text{ne}}} \frac{q_i^2}{2m_i}\hat{\mathbf{A}}^2(\mathbf{r}_i) \approx 2\frac{e^2}{2m_e}\sum_{\boldsymbol{k}'}\sum_{\boldsymbol{k}''}\sum_{\sigma'}\sum_{\sigma''}\sum_{\alpha=1}^{N_{\text{e}}} \\ \times\sqrt{\frac{\hbar}{2\varepsilon_0 V\omega_{\boldsymbol{k}'}}}\sqrt{\frac{\hbar}{2\varepsilon_0 V\omega_{\boldsymbol{k}''}}}\hat{a}^\dagger_{\boldsymbol{k}'\sigma'}\hat{a}_{\boldsymbol{k}''\sigma''}\mathbf{e}_{\boldsymbol{k}'\sigma'}\cdot\mathbf{e}_{\boldsymbol{k}''\sigma''}e^{\iota(\boldsymbol{k}''-\boldsymbol{k}')\cdot\mathbf{r}_\alpha}\,,\end{aligned} \tag{2.84}$$

where we have reduced the sum to the electrons only on account of the much greater mass of nuclei. Substituting in Eq. (2.83), we find the perturbation operator of the material system, $\hat{O}(t')$, to be:

$$\begin{aligned}\hat{O}(t') = \sum_{\boldsymbol{k}} c_{\boldsymbol{k}}e^{\iota(\omega_{\boldsymbol{k}_s}-\omega_{\boldsymbol{k}})t'}\frac{\hbar}{V\varepsilon_0}\frac{e^2}{2m_e} \\ \times\sum_{\boldsymbol{k}'}\sum_{\boldsymbol{k}''}\sum_{\sigma'}\sum_{\sigma''}\frac{P_{\sigma'\sigma''}}{\sqrt{\omega_{\boldsymbol{k}'}\omega_{\boldsymbol{k}''}}}\langle\boldsymbol{k}_s\sigma_s|\hat{a}^\dagger_{\boldsymbol{k}'\sigma'}\hat{a}_{\boldsymbol{k}''\sigma''}|\boldsymbol{k}\sigma_0\rangle\sum_{\alpha=1}^{N_{\text{e}}}e^{\iota(\boldsymbol{k}''-\boldsymbol{k}')\cdot\mathbf{r}_\alpha}\,,\end{aligned} \tag{2.85}$$

where $P_{\sigma'\sigma''} = \mathbf{e}_{\boldsymbol{k}'\sigma'}\cdot\mathbf{e}_{\boldsymbol{k}''\sigma''}$ is the polarisation factor of the X-rays and $\hat{U}_{0,\text{EM}}$ is the propagator for the EM field only. To simplify this expression, we resolve the matrix elements of the creation and annihilation operators:

$$\langle\boldsymbol{k}_s\sigma_s|\hat{a}^\dagger_{\boldsymbol{k}'\sigma'}\hat{a}_{\boldsymbol{k}''\sigma''}|\boldsymbol{k}\sigma_0\rangle = \delta_{\boldsymbol{k}_s\boldsymbol{k}'}\delta_{\boldsymbol{k}''\boldsymbol{k}}\delta_{\sigma_s\sigma'}\delta_{\sigma''\sigma_0}\,, \tag{2.86}$$

as we again require a non-zero momentum transfer, $\boldsymbol{k}' \neq \boldsymbol{k}''$, in the scattering process. Then, Eq. (2.85) reduces to:

$$\hat{O}(t') = \sum_{\boldsymbol{k}} c_{\boldsymbol{k}}e^{\iota(\omega_{\boldsymbol{k}_s}-\omega_{\boldsymbol{k}})t'}\frac{\hbar}{V\varepsilon_0}\frac{e^2}{2m_e}\frac{P_{\sigma_s\sigma_0}}{\sqrt{\omega_{\boldsymbol{k}}\omega_{\boldsymbol{k}_s}}}\sum_{\alpha=1}^{N_{\text{e}}}e^{\iota(\boldsymbol{k}-\boldsymbol{k}_s)\cdot\mathbf{r}_\alpha}\,. \tag{2.87}$$

At this stage, we use the fact that the incoming X-ray beam is comprised of a narrow spread of wave vectors around $\boldsymbol{k}_0$, so that $\boldsymbol{k} = \boldsymbol{k}_0 + \delta\boldsymbol{k}$ and $\omega_{\boldsymbol{k}} = c|\boldsymbol{k}_0 + \delta\boldsymbol{k}|$, to rewrite the perturbation operator $\hat{O}(t')$ as:

$$\hat{O}(t') = e^{\iota(\omega_{\boldsymbol{k}_s}-\omega_0)t'}\frac{\hbar}{V\varepsilon_0}\frac{e^2}{2m_e}\frac{P_{\sigma\sigma_0}}{\sqrt{\omega_{\boldsymbol{k}_s}}}\sum_{\alpha=1}^{N_{\text{e}}}e^{\iota\boldsymbol{q}\cdot\mathbf{r}_\alpha}\sum_{\boldsymbol{k}}c_{\boldsymbol{k}}\frac{e^{\iota(\delta\boldsymbol{k}\cdot\mathbf{r}_\alpha-\delta\omega_{\boldsymbol{k}}t')}}{\sqrt{\omega_0+\delta\omega_{\boldsymbol{k}}}}, \tag{2.88}$$

where we have also introduced the momentum transfer vector, $\boldsymbol{q} = \boldsymbol{k}_0 - \boldsymbol{k}_s$.

To simplify further, we note that $\omega_0 \gg \delta\omega_{\boldsymbol{k}}$ so that $\sqrt{\omega_0 + \delta\omega_{\boldsymbol{k}}} \approx \sqrt{\omega_0}$. We also use the classical definition of the electric field:

$$\mathbf{E}_0(\mathbf{r}_\alpha, t') = |E_0| h(\mathbf{r}_\alpha, t') e^{-\imath\omega_0 t'}, \tag{2.89}$$

with an amplitude:

$$|E_0| = \sqrt{\frac{\hbar\omega_0}{2\varepsilon_0 V}} \tag{2.90}$$

and a field envelope:

$$h(\mathbf{r}_\alpha, t') = \sum_{\boldsymbol{k}} c_{\boldsymbol{k}} e^{\imath(\delta\boldsymbol{k}\cdot\mathbf{r}_\alpha - \delta\omega_{\boldsymbol{k}} t')}. \tag{2.91}$$

If we further assume that the coherence length of the X-ray pulse is long compared to the size of the molecule, we can drop the explicit dependence of the electric field on the electronic coordinates. With that Eq. (2.88) reduces to:

$$\hat{O}(t') = \sqrt{\frac{2\hbar}{V\varepsilon_0\omega_{\boldsymbol{k}_s}}} \frac{Pe^2}{2\omega_0 m_e} E_0(t') \hat{L} e^{\imath\omega_{\boldsymbol{k}_s} t'}, \tag{2.92}$$

where we have introduced the scattering operator:

$$\hat{L} = \sum_{\alpha=1}^{N_e} e^{\imath\boldsymbol{q}\cdot\mathbf{r}_\alpha}. \tag{2.93}$$

We now move on to the evaluation of the differential scattering cross-section, which gives the probability of scattering into a solid angle $d\Omega$, in absence of energy resolution on the detector. It is given by the sum of the probabilities of transition from Ψ to all possible final bound states of the molecule across all scattering frequencies:

$$\frac{dS}{d\Omega} = \int_0^\infty d\omega_{\mathbf{k}_s} \rho(\omega_{\mathbf{k}_s}) \lim_{\substack{t\to\infty \\ t_0\to-\infty}} \sum_{f=1}^{\infty} |S_{f\psi}|^2, \tag{2.94}$$

where the limits ensure the corresponding integrals capture the full dynamics over the duration of the pulse, and $\rho(\omega_{\mathbf{k}_s}) = \frac{\omega_{\mathbf{k}_s}^2 V}{(2\pi c)^3}$ is the density of photon states within a quantization volume V. Using the resolution of the identity, $\hat{1} = \sum_f |f\rangle\langle f|$, and Eq. (2.82), the differential scattering cross-section becomes:

$$\begin{aligned}\frac{dS}{d\Omega} = &\lim_{\substack{t\to\infty \\ t_0\to-\infty}} \int_0^\infty d\omega_{\mathbf{k}_s} \frac{\omega_{\mathbf{k}_s}^2 V}{(2\pi c)^3} \\ &\times \frac{1}{\hbar^2} \int_{t_0}^{t} dt' \int_{t_0}^{t} dt'' \langle \Psi(t'')|\hat{O}^\dagger(t'')\hat{U}_0^\dagger(t,t'')\hat{U}_0(t,t')\hat{O}(t')|\Psi(t')\rangle.\end{aligned} \tag{2.95}$$

Using the exact form of the time-evolution operator of the molecular system given in Eq. (2.92), the differential scattering cross-section becomes:

$$\begin{aligned}\frac{dS}{d\Omega} = &\frac{1}{2\pi}\frac{d\sigma_{\mathrm{Th}}}{d\Omega} \lim_{\substack{t\to\infty \\ t_0\to-\infty}} \int_0^\infty d\omega_{\mathbf{k}_s} \int_{t_0}^{t} dt' \int_{t_0}^{t} dt'' \frac{\omega_{\mathbf{k}_s}}{\omega_0} \\ &\times \frac{2c\varepsilon_0}{\hbar\omega_0} E_0^*(t'')E_0(t')e^{-\imath\omega_{k_s}(t''-t')} \langle \Psi(t'')|\hat{L}^\dagger \hat{U}_0(t'',t')\hat{L}|\Psi(t')\rangle,\end{aligned} \tag{2.96}$$

where we have identified the Thomson scattering cross-section of a free electron:

$$\frac{d\sigma_{\mathrm{Th}}}{d\Omega} = \frac{e^4 P^2}{16\pi^2\varepsilon_0^2 m_e^2 c^4}. \tag{2.97}$$

As a side note, it should be pointed out that the presence of the Thomson cross-section should not be a surprise as we work in the framework of non-relativistic quantum dynamics. At higher X-ray energies, however, relativistic effects become important. Working in this regime naturally gives rise to the Klein–Nishina formula for the Compton cross-section of a free electron instead [72]. While it is common to refer to inelastic X-ray scattering from molecules as Compton scattering, strictly speaking Compton scattering is a relativistic phenomenon. The formalism presented here fully accounts for inelastic effects in molecules despite being restricted to a non-relativistic description.

Clearly, the two integrals over time and the one over the frequency of the scattered radiation in Eq. (2.96) are entangled via the action of the scattering

operator on the time-dependent wave functions. The way to solve this issue is to invoke the so-called Waller-Hartree approximation [73], which states that $\omega_{\boldsymbol{k}_s} \approx \omega_0$. The justification of this approximation is that any difference between the frequencies of the incoming and scattered radiation is on the order of the transitions in the material system, so somewhere on the order of a few eV. This difference is small on the scale of the absolute energy of a hard X-ray photon, which is a few keV. A qualitative discussion can be found in Ref [69]. After making this approximation, we are allowed to do two things. Firstly, we set $\omega_{\boldsymbol{k}_s}/\omega_0 \approx 1$. Secondly, we can treat the scattering operators as independent of the wavelength of the scattered photon. Note that the latter does not mean that we will only consider elastic scattering. The approximation only implies that the direction of scattering is unaffected by $\omega_{\boldsymbol{k}_s}$. The integral over the scattered radiation can then be dealt with independently. We first note that in a real experiment, the detector would inevitably operate over a restricted window of frequencies, $2\Delta\omega$, which we will assume to be centred at the frequency of the incident X-rays, ω_0. The integral over $\omega_{\boldsymbol{k}_s}$ then becomes:

$$\int_{\omega_0-\Delta\omega}^{\omega_0+\Delta\omega} d\omega_{\boldsymbol{k}_s} e^{\imath\omega_{\boldsymbol{k}_s}(t''-t')} = 2\Delta\omega \mathrm{sinc}\big(\Delta\omega(t''-t')\big) e^{-\imath\omega_0(t''-t')}. \tag{2.98}$$

For a small value of $\Delta\omega$, this integral effectively introduces a window function that accounts for the number of photons captured in the permissible range [74]. However, for sufficiently large values of $\Delta\omega$ the integral reduces to a delta function, $2\Delta\omega\mathrm{sinc}(\Delta\omega(t''-t')) \rightarrow 2\pi\delta(t'-t'')$. Eq. (2.96) then greatly simplifies to:

$$\frac{dS}{d\Omega} = \frac{d\sigma_{\mathrm{Th}}}{d\Omega} \int_{-\infty}^{\infty} dt' \frac{2c\varepsilon_0}{\hbar\omega_0} E_0^*(t') E_0(t') \langle \Psi(t') | \hat{L}^\dagger \hat{L} | \Psi(t') \rangle. \tag{2.99}$$

Lastly, replacing t' by τ as the variable of integration, and noting that the number intensity of the incoming X-ray pulse centred at $\tau = t$ is $I(\tau - t) = 2c\varepsilon_0/(\hbar\omega_0) E_0^*(t) E_0(t)$:

$$\frac{dS}{d\Omega}(\boldsymbol{q}, t) = \frac{d\sigma_{\mathrm{Th}}}{d\Omega} \int_{-\infty}^{\infty} d\tau I(\tau - t) \langle \Psi(\tau) | \hat{L}^\dagger \hat{L} | \Psi(\tau) \rangle. \tag{2.100}$$

This relatively simple equation is going to be the basis of the discussions that follow. At that stage, it is prudent to recap the approximations made so far. It has been assumed that the incoming X-ray beam is polarised and has a narrow bandwidth around ω_0. We have required that the molecule is small compared to the coherence length of the X-ray pulse. The Waller-Hartree approximation ($\omega_{\boldsymbol{k}_s} \approx \omega_0$) was used to simplify the integration over the frequencies of the scattered photons. Finally, we have assumed that the detector can detect all scattered photons regardless of their frequency. Implicit assumptions are also that the photon energy, while still in the hard X-ray regime, is not too high so as to avoid relativistic effects, and that the molecule exists in a superposition of bound states. This equation is an analogue of the description of scattering in the first Born approximation in the classical theory of scattering.

To understand better the meaning of Eq. (2.100), we can go a step further by using the Born-Huang ansatz in Eq. (2.74) for the N electronic states prepared by the pump laser. The differential scattering cross section then becomes:

$$\frac{dS}{d\Omega}(\boldsymbol{q}, t) = \frac{d\sigma_{\mathrm{Th}}}{d\Omega} \sum_{i,j}^{N} \int d\tau \; I(\tau - t) \; \langle \chi_i(\tau) | \Lambda_{ij}(\boldsymbol{q}, \bar{\boldsymbol{R}}) | \chi_j(\tau) \rangle. \tag{2.101}$$

The central quantity in Eq. (2.101) is the two-electron scattering matrix element, $\Lambda_{ij}(\boldsymbol{q}, \bar{\boldsymbol{R}})$. Using the definition of the scattering operator in Eq. (2.93), the matrix element is given by

$$\Lambda_{ij}(\boldsymbol{q}, \bar{\boldsymbol{R}}) = \sum_{m,n}^{N_{\mathrm{e}}} \langle \psi_i(\bar{\boldsymbol{R}}) | e^{\imath \boldsymbol{q} \cdot (\boldsymbol{r}_m - \boldsymbol{r}_n)} | \psi_j(\bar{\boldsymbol{R}}) \rangle. \tag{2.102}$$

From the orthogonality of the electronic states, terms in Eq. (2.102) where $m = n$ reduce to the Kronecker delta δ_{ij}. The two-electron scattering matrix element then becomes:

$$\Lambda_{ij}(\boldsymbol{q}, \bar{\boldsymbol{R}}) = N_{\mathrm{e}} \delta_{ij} + \Lambda'_{ij}(\boldsymbol{q}, \bar{\boldsymbol{R}}), \tag{2.103}$$

where $\Lambda'_{ij}(\boldsymbol{q}, \bar{\boldsymbol{R}})$ represents the pure two-electron part of Eq. (2.102) with

$m \neq n$. Invoking the sifting property of the Dirac delta function, the exponential in Eq. (2.102) can be cast into an integral form:

$$e^{\imath \boldsymbol{q}\cdot(\boldsymbol{r}_m - \boldsymbol{r}_n)} = \iint d\boldsymbol{r}_1 \, d\boldsymbol{r}_2 \, e^{\imath \boldsymbol{q}\cdot(\boldsymbol{r}_1 - \boldsymbol{r}_2)} \delta(\boldsymbol{r}_1 - \boldsymbol{r}_m)\delta(\boldsymbol{r}_2 - \boldsymbol{r}_n). \tag{2.104}$$

Finally, the the integral over the electronic coordinates in Eq. (2.102) implied by the bra-ket notation becomes

$$\Lambda_{ij}(\boldsymbol{q}, \bar{\boldsymbol{R}}) = N_\mathrm{e}\delta_{ij} + 2 \iint d\boldsymbol{r}_1 \, d\boldsymbol{r}_2 \, \rho_{ij}^{(2)}(\boldsymbol{r}_1, \boldsymbol{r}_2, \bar{\boldsymbol{R}}) e^{\imath \boldsymbol{q}\cdot(\boldsymbol{r}_1 - \boldsymbol{r}_2)}, \tag{2.105}$$

where $\rho_{ij}^{(2)}(\boldsymbol{r}_1, \boldsymbol{r}_2, \bar{\boldsymbol{R}})$ is the expectation value of the two-electron density operator $\hat{\rho}(\boldsymbol{r}_1, \boldsymbol{r}_2) = (1/2) \sum_m^{N_\mathrm{e}} \sum_{n\neq m}^{N_\mathrm{e}} \delta(\boldsymbol{r}_1 - \boldsymbol{r}_m)\delta(\boldsymbol{r}_2 - \boldsymbol{r}_n)$ [75]. The diagonal elements of two-electron density give the probability, for a given electronic state, of finding an electron at $\boldsymbol{r}_1$, while another electron is at $\boldsymbol{r}_2$. In connection to that, scattering should not be viewed as a process that occurs from the averaged electron density of the molecule. The correct interpretation is that the incoming beam encounters an instantaneous electron density of correlated electrons, and then the intensity is averaged over possible quantum states. With reference to Eq. (2.101), the scattering from each electronic state is weighted by the ro-vibrational wave function of the molecule in that state.

At that point, we should discuss the role of the diagonal elements with respect to the electronic states with $i = j$ and off-diagonal (mixed) terms with $i \neq j$ summarised in Table 2.1. In the former case, $\rho_{ii}^{(2)}(\boldsymbol{r}_1, \boldsymbol{r}_2, \bar{\boldsymbol{R}})$, known as the two-electron density function, can be further divided into two parts by expanding it as a sum of products over one-electron density functions, $\rho_{if}^{(1)}(\boldsymbol{r}, \bar{\boldsymbol{R}})$. This is achieved by introducing the resolution of the identity in the basis of the electronic states. The resulting equation is:

$$N_\mathrm{e} + 2\rho_{ii}^{(2)}(\boldsymbol{r}_1, \boldsymbol{r}_2, \bar{\boldsymbol{R}}) = \rho_{ii}^{(1)}(\boldsymbol{r}_1, \bar{\boldsymbol{R}})\rho_{ii}^{(1)}(\boldsymbol{r}_2, \bar{\boldsymbol{R}}) + \sum_{f\neq i} \rho_{if}^{(1)}(\boldsymbol{r}_1, \bar{\boldsymbol{R}})\rho_{fi}^{(1)}(\boldsymbol{r}_2, \bar{\boldsymbol{R}}). \tag{2.106}$$

The first term on the right-hand side of Eq. (2.106) is responsible for elastic

scattering, while the contribution from the second term is inelastic. Both contributions are purely electronic. We note that in absence of energy resolution on the detector, these terms cannot be distinguished, *i.e.* we only detect the total scattering cross-section. Nevertheless, sometimes we talk about elastic and inelastic contributions to scattering when interpreting experimental results. In that case, inelastic scattering refers to the entire sum in Eq. (2.106), not to individual transitions.

TABLE 2.1: Summary of the electronic X-ray scattering matrix elements that arise from the full quantum mechanical treatment of a system that exists as a superposition of states, here labelled as i and j. The state labelled as f is a final state that results from the exchange of energy between the system and the X-ray photon. The following notation is used for the double Fourier transform $\mathcal{F}^{(2)}[\rho(\boldsymbol{r}_1,\boldsymbol{r}_2)] = \iint d\boldsymbol{r}_1\, d\boldsymbol{r}_2\, \rho(\boldsymbol{r}_1,\boldsymbol{r}_2) e^{i\boldsymbol{q}\cdot(\boldsymbol{r}_1-\boldsymbol{r}_2)}$.

scattering cross-section	notation	electronic integral
total	$\Lambda_{ii}(\boldsymbol{q},\bar{\boldsymbol{R}})$	$N_\mathrm{e} + 2\mathcal{F}^{(2)}[\rho_{ii}^{(2)}(\boldsymbol{r}_1,\boldsymbol{r}_2,\bar{\boldsymbol{R}})]$
elastic	$\Lambda_{ii}^\mathrm{e}(\boldsymbol{q},\bar{\boldsymbol{R}})$	$\mathcal{F}^{(2)}[\rho_{ii}^{(1)}(\boldsymbol{r}_1,\bar{\boldsymbol{R}})\rho_{ii}^{(1)}(\boldsymbol{r}_2,\bar{\boldsymbol{R}})]$
total inelastic	$\Lambda_{ii}^\mathrm{i}(\boldsymbol{q},\bar{\boldsymbol{R}})$	$\sum_{f\neq i}\mathcal{F}^{(2)}[\rho_{if}^{(1)}(\boldsymbol{r}_1,\bar{\boldsymbol{R}})\rho_{fi}^{(1)}(\boldsymbol{r}_2,\bar{\boldsymbol{R}})]$
coherent mixed	$\Lambda_{ij}(\boldsymbol{q},\bar{\boldsymbol{R}})$	$\mathcal{F}^{(2)}[\rho_{ij}^{(2)}(\boldsymbol{r}_1,\boldsymbol{r}_2,\bar{\boldsymbol{R}})]$

For $i \neq j$, the quantity $\rho_{ij}^{(2)}(\boldsymbol{r}_1,\boldsymbol{r}_2,\bar{\boldsymbol{R}})$ in Eq. (2.105) is known as the two-electron transition density function. It gives rise to coherent mixed scattering, which appears when there is a coherence between two electronic states [76–79]. It is worth noting that in many practical situations, including the experiments described in this thesis, coherent mixed scattering can be safely ignored. The reason is that it oscillates rapidly because of the interference between the two electronic states. For energetically well-separated states, the oscillation period could be below 1 fs, which makes it impossible to resolve, unless the X-ray pulse is extremely short. In the regions of conical intersections, the states come closer, so this argument does not hold any more. However, there the coherence between states could be very short-lived because of the small spatial overlap of the nuclear wave packets on the two states. Overall, a careful choice of experimental parameters and a

system would be needed to unambiguously detect coherent mixed scattering.

Chapter 3

Practical Aspects of the Analysis of UXS Experiments

3.1 Overview

This chapter presents some practical aspects of the theory that concern the analysis and the interpretation of actual experiments. It should be pointed out that matters related to the experimental set-up and procedure are not discussed. The chapter begins by introducing the Legendre decomposition of the scattering signal, which allows the signal to be separated into isotropic and anisotropic components. This separation is the key to disentangling the contributions from internal and rotational molecular degrees of freedom. In UXS experiments, the observed changes as a function of time are small on the scale of the absolute signal, and are therefore analysed in terms of the fractional signal change described in Section 3.3. It also plays an important role in dealing with hard-to-control experimental parameters such as the excitation fraction, background signal and pressure fluctuations. To make the first step towards understanding the observed signal it is often practical to rely on approximate but rapid methodologies. The so-called Independent Atom Model (IAM) will be introduced and its usability and limitations discussed. The chapter concludes with some remarks about the manifestation of photodissociation in the experimental signal, and the possibility of implementing "direct inversion" schemes for the analysis of experimental data.

3.2 Legendre Decomposition

UXS experiments in the gas phase are often performed close to room temperature and without explicit alignment of the molecules. This implies that prior to the pump laser (*i.e.* before time zero) the ensemble is fully isotropic and the molecules are in their ground electronic state. However, if a linearly polarised pump laser is used to initiate a photochemical reaction in the single-photon excitation regime, the probability of excitation is proportional to the cosine squared of the angle between the laser polarisation axis and the transition dipole moment (TDM) of the resonant excited electronic state as detailed in Section 2.6. There is also, of course, an associated sine squared "hole" in the ground-state probability. In a language consistent with a statistical semi-classical treatment, the pump laser preferentially excites those molecules whose TDM aligns with the laser's polarisation axis, while the unexcited molecules suffer a depletion at this orientation as a consequence. The spatial anisotropy of the ensemble causes the scattering signal to become anisotropic as depicted in Figure 3.1.

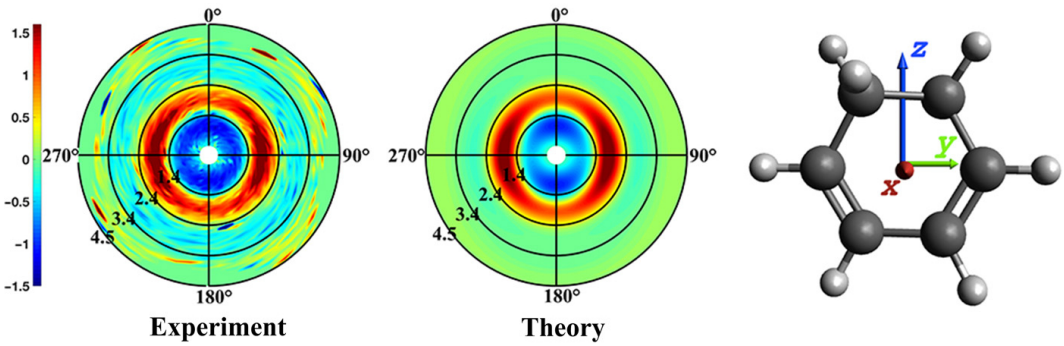

FIGURE 3.1: Theoretical and experimental X-ray scattering shortly after photoexcitation of 1,3-cyclohexadiene with a linearly polarised laser. The signal shows strong anisotropy as a result of the preferential excitation of the molecules that have their transition dipole moment vector aligned with the laser polarisation axis, which is perpendicular to the X-ray propagation. The signal is expressed as a fractional signal change as described in Section 3.3. Reproduced from Ref. [80].

Immediately after the excitation, the scattering signal would only exhibit

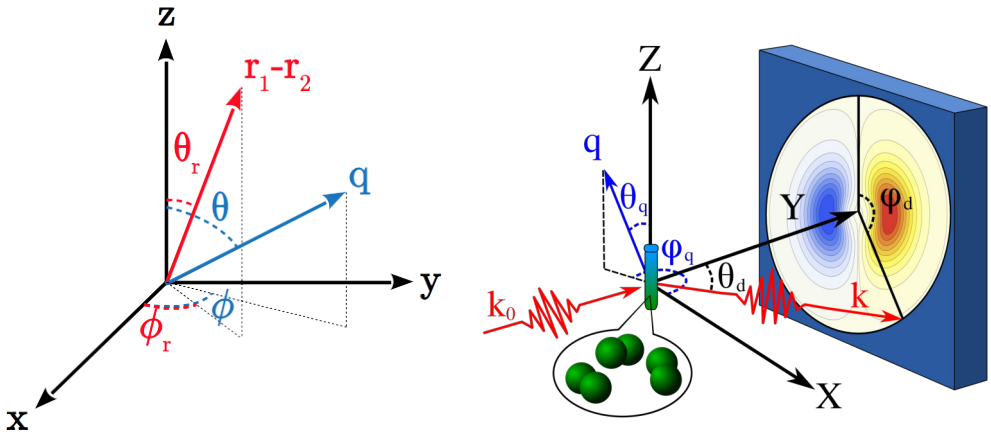

(A) Molecular frame

(B) Laboratory frame

FIGURE 3.2: Angles describing the scattering process. Subfigure 3.2a shows the scattering vector, $\boldsymbol{q} = (q, \theta, \phi)$, and the interelectron distance vector, $\boldsymbol{r}_1 - \boldsymbol{r}_2 = (r, \theta_r, \phi_r)$, in the molecular frame. Subfigure 3.2b shows the scattering vector, $\boldsymbol{q} = (q, \theta_q, \phi_q)$, and the detector polar and azimuthal angles, θ_d and ϕ_d, in the laboratory frame of reference. It is assumed that that the polarisation vector of the pump laser, which defines the laboratory frame $\hat{\mathbf{Z}}$-axis, is perpendicular to the X-ray propagation. Reproduced from Ref. [84]. The transformation between the two frames is specified by the three Euler angles, (α, β, γ). Here, in describing the Euler angles we adopt the convention by Zare [58].

a weak anisotropy on account of the small geometrical difference between the ground and excited state species. Usually, the electron redistribution in the excited state is a weak effect and not easily observed in scattering. However, as the photochemical reaction unfolds, the difference between the ground and excited state structures may become significant, and a strong anisotropy would be observed in the scattering signal. As rotational motion is generally slower than internal dynamics, the anisotropy could persist for picoseconds before rotational dephasing renders the scattering signal isotropic again. At later times, however, rotational revivals may bring back the anisotropy [81–83].

Obviously, the competition between rotational and internal degrees of

freedom seen in the scattering signal is undesirable. While valuable information is contained in both, it is preferable if the two effects can be separated out. The solution is to decompose the detected signal into Legendre amplitudes [85–88]. To see why this is possible and how it works, we try to bring out the angular dependencies of the differential scattering cross-section in Eq. (2.101). The derivations in this section were first presented in the Supplementary Information of Ref. [84]. Unlike the previous work on the subject, the theoretical framework is quite general – it goes beyond the IAM and does not make assumptions about the symmetry of the molecule. We start by noting that the delta function term in Eq. (2.105) is a constant that adds isotropically to the cross-section. However, the pure two-electron part,

$$\Lambda'_{ij}(\boldsymbol{q}, \bar{\boldsymbol{R}}) = 2 \iint d\boldsymbol{r}_1 \, d\boldsymbol{r}_2 \, \rho^{(2)}_{ij}(\boldsymbol{r}_1, \boldsymbol{r}_2, \bar{\boldsymbol{R}}) e^{\imath \boldsymbol{q} \cdot (\boldsymbol{r}_1 - \boldsymbol{r}_2)}, \tag{3.1}$$

needs special attention. Its angular dependence can be investigated by expressing the exponential using a plane wave expansion:

$$e^{\imath \boldsymbol{q} \cdot (\boldsymbol{r}_1 - \boldsymbol{r}_2)} = 4\pi \sum_{l=0}^{\infty} \sum_{m=-l}^{l} \imath^l j_l(qr) Y_l^m(\theta, \phi) Y_l^{m*}(\theta_r, \phi_r). \tag{3.2}$$

Here, θ and ϕ are the polar and azimuthal angles of the momentum transfer vector, respectively, and r, θ_r, and ϕ_r are the radial, polar, and azimuthal coordinates of the distance vector $\boldsymbol{r}_1 - \boldsymbol{r}_2$ (See Figure 3.2). The $j_l(qr)$ are spherical Bessel functions. The coordinates are given in the molecular frame as this will help us deal with integrals over the electronic coordinates later. However, we are ultimately interested in the observed scattering signal at the detector, which is fixed in the laboratory frame, so we need to express the scattering vector in the same frame. Without loss of generality, let us take the laser polarisation axis as the lab frame $\hat{\mathbf{Z}}$-axis. The polar and azimuthal angles of the scattering vector in the molecular frame, θ and ϕ, are related to their counterparts in lab frame, θ_q and ϕ_q, via the Euler angles (α, β, γ). The connection is established by the rotation of the Spherical Harmonics theorem:

$$Y_l^m(\theta, \phi) = \sum_{m'=-l}^{l} D^l_{m',m}(\alpha, \beta, \gamma) Y_l^{m'}(\theta_q, \phi_q), \tag{3.3}$$

where $D^{l}_{m',m}(\alpha,\beta,\gamma)$ are the elements of the Wigner D-matrix. Eq. (3.2) then becomes:

$$e^{\imath \boldsymbol{q}\cdot(\boldsymbol{r}_1-\boldsymbol{r}_2)} = 4\pi \sum_{l=0}^{\infty} \sum_{m=-l}^{l} \sum_{m'=-l}^{l} \imath^l j_l(qr) D^{l}_{m',m}(\alpha,\beta,\gamma) Y_l^{m'}(\theta_q,\phi_q) Y_l^{m*}(\theta_r,\phi_r). \tag{3.4}$$

Introducing Eq. (3.4) back into Eq. (3.1) leads to:

$$\begin{aligned} \Lambda'_{ij}(\boldsymbol{q},\bar{\boldsymbol{R}}) = 8\pi \sum_{l=0}^{\infty} \sum_{m=-l}^{l} \sum_{m'=-l}^{l} \imath^l D^{l}_{m',m}(\alpha,\beta,\gamma) Y_l^{m'}(\theta_q,\phi_q) \\ \times \iint d\boldsymbol{r}_1\, d\boldsymbol{r}_2\, \rho^{(2)}_{ij}(\boldsymbol{r}_1,\boldsymbol{r}_2,\bar{\boldsymbol{R}}) j_l(qr) Y_l^{m*}(\theta_r,\phi_r). \end{aligned} \tag{3.5}$$

Eq. (3.5) can then be introduced into the matrix element $\langle \chi_i(\tau)|\Lambda'_{ij}(\boldsymbol{q},\bar{\boldsymbol{R}})|\chi_j(\tau)\rangle$ that appears in Eq. (2.101) for the differential scattering cross-section. In doing so, the nuclear wave packet $|\chi_i(\tau)\rangle$ can been split into a product of rotational, $|\theta^{\mathrm{r}}_i(\tau)\rangle$, and vibrational, $|\chi^{\mathrm{v}}_i(\tau)\rangle$, wave packets:

$$\begin{aligned} \langle \chi^{\mathrm{v}}_i \theta^{\mathrm{r}}_i|\Lambda'_{ij}(\boldsymbol{q},\bar{\boldsymbol{R}})|\theta^{\mathrm{r}}_j \chi^{\mathrm{v}}_j\rangle =& 8\pi \sum_{l}^{\infty} \sum_{m=-l}^{l} \sum_{m'=-l}^{l} \imath^l \langle \theta^{\mathrm{r}}_i|D^{l}_{m',m}(\alpha,\beta,\gamma)|\theta^{\mathrm{r}}_j\rangle\, Y_l^{m'}(\theta_q,\phi_q) \\ & \times \langle \chi^{\mathrm{v}}_i| \iint d\boldsymbol{r}_1\, d\boldsymbol{r}_2\, \rho^{(2)}_{ij}(\boldsymbol{r}_1,\boldsymbol{r}_2,\bar{\boldsymbol{R}}) j_l(qr) Y_l^{m*}(\theta_r,\phi_r)|\chi^{\mathrm{v}}_j\rangle. \end{aligned} \tag{3.6}$$

Note their time-dependence is omitted in order to simplify the notation, and will be reintroduced later. We notice that the rotational wave packets must be invariant with respect to rotation around the laser polarisation axis, which also defines the laboratory frame $\hat{\mathbf{Z}}$. That means that integral over the Euler angles would vanish for Wigner D-matrices that do not have the same symmetry. The only permissible terms are those with $m = m' = 0$, *i.e.* $D^{l}_{0,0}(\alpha,\beta,\gamma) = P_l(\cos\beta)$. The corresponding spherical harmonics in Eq. (3.6) are

$$Y_l^0(\theta_q,\phi_q) = \sqrt{\frac{2l+1}{4\pi}} P_l(\cos\theta_q) \tag{3.7}$$

and

$$Y_l^0(\theta_r,\phi_r) = \sqrt{\frac{2l+1}{4\pi}} P_l(\cos\theta_r), \tag{3.8}$$

where $P_l(\cos x)$ are the Legendre polynomials. With that, Eq. (3.6) becomes:

$$\langle \chi_i^{\mathrm{v}} \theta_i^{\mathrm{r}} | \Lambda'_{ij}(\boldsymbol{q}, \bar{\boldsymbol{R}}) | \theta_j^{\mathrm{r}} \chi_j^{\mathrm{v}} \rangle = \sum_{l=0}^{\infty} P_l(\cos\theta_q)\, 2(2l+1)\imath^l\, \langle \theta_i^{\mathrm{r}} | P_l(\cos\beta) | \theta_j^{\mathrm{r}} \rangle \times \langle \chi_i^{\mathrm{v}} | \iint d\boldsymbol{r}_1\, d\boldsymbol{r}_2\, \rho_{ij}^{(2)}(\boldsymbol{r}_1, \boldsymbol{r}_2, \bar{\boldsymbol{R}}) j_l(qr) P_l(\cos\theta_r) | \chi_j^{\mathrm{v}} \rangle. \tag{3.9}$$

Inserting Eq. (3.9) into Eq. (2.101) and reinstating the time dependence of the nuclear wave packets leads to:

$$\begin{aligned} \frac{dS}{d\Omega}(\boldsymbol{q}, t) = \frac{d\sigma_{\mathrm{Th}}}{d\Omega} \int d\tau\, I(\tau - t)\, \Big[\, N_{\mathrm{e}} + \sum_{i,j}^{N} \sum_{l=0}^{\infty} P_l(\cos\theta_q)\, 2(2l+1)\imath^l \\ \times \langle \theta_i^{\mathrm{r}}(\tau) | P_l(\cos\beta) | \theta_j^{\mathrm{r}}(\tau) \rangle \\ \times \langle \chi_i^{\mathrm{v}}(\tau) | \iint d\boldsymbol{r}_1\, d\boldsymbol{r}_2\, \rho_{ij}^{(2)}(\boldsymbol{r}_1, \boldsymbol{r}_2, \bar{\boldsymbol{R}}) j_l(qr) P_l(\cos\theta_r) | \chi_j^{\mathrm{v}}(\tau) \rangle \,\Big], \end{aligned} \tag{3.10}$$

which can also be written as:

$$\frac{dS}{d\Omega}(\boldsymbol{q}, t) = \sum_{l}^{\infty} P_l(\cos\theta_q) S_l(q, t), \tag{3.11}$$

where the Legendre amplitude is

$$\begin{aligned} S_l(q, t) = \frac{d\sigma_{\mathrm{Th}}}{d\Omega} \int d\tau\, I(\tau - t)\, \Big[\, N_{\mathrm{e}}\delta_{l0} + 2(2l+1)\imath^l \sum_{i,j}^{N} \langle \theta_i^{\mathrm{r}}(\tau) | P_l(\cos\beta) | \theta_j^{\mathrm{r}}(\tau) \rangle \\ \times \langle \chi_i^{\mathrm{v}}(\tau) | \iint d\boldsymbol{r}_1\, d\boldsymbol{r}_2\, \rho_{ij}^{(2)}(\boldsymbol{r}_1, \boldsymbol{r}_2, \bar{\boldsymbol{R}}) j_l(qr) P_l(\cos\theta_r) | \chi_j^{\mathrm{v}}(\tau) \rangle \,\Big]. \end{aligned} \tag{3.12}$$

Eq. (3.11) means that the scattering signal can always be decomposed in a basis of Legendre polynomials. Note that this is so far quite general and does not assume anything about the pump pulse except linear polarisation. As pointed out previously, mixed coherence terms are negligibly small for sufficiently long X-ray pulses, so we can omit them from the expression. Furthermore, assuming a single-photon excitation implies an initial cosine squared distribution of molecules in space. With reference to the matrix

element $\langle\theta_i^{\mathrm{r}}(t)|P_l(\cos\beta)|\theta_i^{\mathrm{r}}(t)\rangle$, the only allowed values of l are then 0 and 2. Note that this also applies to the ground state "hole".

The zeroth-order term, $S_0(q,t)$, is referred to as the isotropic scattering signal and is given by:

$$S_0(q,t) = \frac{d\sigma_{\mathrm{Th}}}{d\Omega}\int d\tau\; I(\tau - t) \times \left[\, N_{\mathrm{e}} + 2\sum_i^N \langle\chi_i^{\mathrm{v}}(\tau)| \iint d\boldsymbol{r}_1\, d\boldsymbol{r}_2\, \rho_{ii}^{(2)}(\boldsymbol{r}_1,\boldsymbol{r}_2,\bar{\boldsymbol{R}}) j_0(qr)|\chi_i^{\mathrm{v}}(\tau)\rangle \,\right]. \tag{3.13}$$

Most importantly, we note that the rotational wave packets in the isotropic scattering in Eq. (3.13) have been integrated to unity. The equation is expressed only in internal coordinates. This is extremely advantageous for the analysis of experiments as the internal degrees of freedom have been isolated from the rotational motion, which now affects the isotropic signal only indirectly via the weak rotational-vibrational coupling.

The second-order term represents the anisotropic scattering signal:

$$S_2(q,t) = -\frac{d\sigma_{\mathrm{Th}}}{d\Omega}\int d\tau\; I(\tau - t)\; 10\sum_i^N \langle\theta_i^{\mathrm{r}}(\tau)|P_2(\cos\beta)|\theta_i^{\mathrm{r}}(\tau)\rangle \times \langle\chi_i^{\mathrm{v}}(\tau)| \iint d\boldsymbol{r}_1\, d\boldsymbol{r}_2\, \rho_{ii}^{(2)}(\boldsymbol{r}_1,\boldsymbol{r}_2,\bar{\boldsymbol{R}}) j_2(qr) P_2(\cos\theta_r)|\chi_i^{\mathrm{v}}(\tau)\rangle. \tag{3.14}$$

Remarkably, the internal dynamics encoded in this term are exactly equivalent to that in the isotropic signal. That is, isotropic and anisotropic scattering provide two different routes to the same information, however, in the latter case internal motion is mingled with the rotational dynamics as seen from the presence of the rotational wave packets in Eq. (3.14).

What are the practical considerations that stem from the Legendre decomposition? Firstly, the polar angle of the scattering vector, θ_q, that appears in Eq. (3.11) is related to the detector polar and azimuthal angles, θ_d and ϕ_d, for a given experimental set-up. More specifically, for a fixed angle between the polarisation vector of the pump pulse and the wave vector of

the x-ray beam, δ, the following geometric relation holds:

$$\cos\theta_q = \sin(\theta_d/2)\cos\delta - \cos(\theta_d/2)\cos\phi_d\sin\delta. \tag{3.15}$$

The experiments discussed in this thesis are performed with the laser polarisation axis perpendicular to the direction of X-ray propagation, in which case Eq. (3.15) reduces to $\cos\theta_q = -\cos\frac{\theta_d}{2}\cos\phi_d$. On the other extreme, where the laser polarisation is parallel to the X-ray propagation, Eq. (3.15) becomes $\cos\theta_q = \sin(\theta_d/2)$. Notably, this implies that the scattering signal does not show variation with the azimuthal detector angle, ϕ_d, *i.e.* it appears isotropic at the detector. Regardless of the value of δ, the Legendre amplitudes, $S_0(q)$ and $S_2(q)$, can be extracted from the θ_d and ϕ_d dependence of the differential scattering cross-section observed on the detector. This can easily be done using a linear fitting procedure, where the isotropic scattering is given by the y-intercept and the anisotropic $S_2(q)$ component is given by the slope [88, 89]. Similar fitting procedures are possible for higher degree of alignment, *i.e.* where terms with $l > 2$ participate in the Legendre expansion.

Another important point is that the isotropic scattering in Eq. (3.13) is exactly equivalent to the scattering from a fully isotropic ensemble [88–90]. This can be shown by making the rotational wave packets in Eq. (3.12) isotropic, which means that the only non-vanishing integral over the Euler angles is the one with $l = 0$, that is $\langle\theta_i^{\mathrm{r}}(t)|P_l(\cos\beta)|\theta_j^{\mathrm{r}}(t)\rangle = \delta_{l0}$. The zeroth-order spherical Bessel function $j_0(qr)$ that appears in Eq. (3.13) is also found in the Debye formula for rotationally averaged scattering in the context of the IAM, which is discussed in Section 3.4.

As a concluding remark, it should be stressed that isotropic-anisotropic Legendre decomposition should be performed with respect to the polar angle of the scattering vector, θ_q, not with the azimuthal detector angle, ϕ_d. Let us take for example the case of a parallel pump-probe set-up with $\delta = 0$, for which the experimental signal appears fully isotropic on the detector. Performed correctly, the decomposition yields isotropic and anisotropic components. The isotropic component is always fully equivalent to the scattering from a fully isotropic rotational wave packet, while the anisotropic part

accounts for the deviation from that situation. Incorrectly performing the Legendre decomposition with respect to ϕ_d would yield only a zeroth-order term that does not correspond to an isotropic ensemble of molecules.

3.3 Fractional Signal Change

In practice, the Legendre decomposition presented in Section 3.2 is the final step in the processing of experimental data. There are a number of important procedural steps that come before that, which are beyond the scope of this thesis [91]. Among those are various filters for abnormal X-ray shots and masks for bad detector pixels. Corrections have to be made to account for the flat detector area and the effective pixel size. Shots taken at similar time-points are binned to improve signal-to-noise ratio. The X-ray intensity at non-seeded XFELs also fluctuates significantly during the course of the experiment, which needs to be accounted for when the data is processed. However, certain parameters such as background signal, instrument function, X-ray polarisation and gas pressure fluctuations can be dealt with in an elegant fashion by using the fractional signal change, $\Delta S(\boldsymbol{q}, t)$, (also called fractional difference signal, or percentage intensity change if expressed as a percentage) instead of the absolute intensity:

$$\Delta S(\boldsymbol{q}, t) = \frac{I_{\text{on}}(\boldsymbol{q}, t) - I_{\text{off}}(\boldsymbol{q}, t_0)}{I_{\text{off}}(\boldsymbol{q}, t_0)}, \tag{3.16}$$

where $I_{\text{on}}(\boldsymbol{q}, t)$ is the observed signal at time delay t (pump pulse on), and $I_{\text{off}}(\boldsymbol{q}, t_0)$ is the signal without the pump pulse (pump pulse off). Obviously, $I_{\text{on}}(\boldsymbol{q}, t)$ and $I_{\text{off}}(\boldsymbol{q}, t_0)$ correspond to solutions of Eq. (2.101) as detected in the experiment. In terms of the fraction of excited molecules, γ, the signal after the excitation is simply:

$$I_{\text{on}}(\boldsymbol{q}, t) = \gamma I_{\text{exc}}(\boldsymbol{q}, t) + (1 - \gamma) I_{\text{X}}(\boldsymbol{q}, t), \tag{3.17}$$

where $I_{\text{exc}}(\boldsymbol{q}, t)$ and $I_{\text{X}}(\boldsymbol{q}, t)$ are the components of the signal from the excited and the unexcited populations at time t, respectively. The signal prior

to the pump is then:

$$I_{\text{off}}(\boldsymbol{q}, t_0) = I_{\text{X}}(\boldsymbol{q}, t_0) = S_0^{\text{X}}(q, t_0), \tag{3.18}$$

where the last equality follows from the fact that, as discussed before, the scattering is fully isotropic before the pump laser breaks the symmetry. The result in Eq. (3.17) can also be written in terms of isotropic and anisotropic Legendre amplitudes as:

$$\begin{aligned} I_{\text{on}}(\boldsymbol{q}, t) =& \gamma S_0^{\text{exc}}(q, t) + (1-\gamma) S_0^{\text{X}}(q, t_0) \\ &+ P_2(\cos\theta_q) \left[\gamma S_2^{\text{exc}}(q, t) + (1-\gamma) S_2^{\text{X}}(q, t)\right], \end{aligned} \tag{3.19}$$

where we have assumed that no internal dynamics occurs for the unexcited molecules so that we can set $S_0^{\text{X}}(q, t) = S_0^{\text{X}}(q, t_0)$. Introducing Eq. (3.18) and Eq. (3.19) into Eq. (3.16) results in:

$$\begin{aligned} \Delta S(\boldsymbol{q}, t) &= \Delta S_0(q, t) + P_2(\cos\theta_q) \Delta S_2(q, t) \\ &= \gamma \frac{S_0^{\text{exc}}(q, t) - S_0^{\text{X}}(q, t_0)}{S_0^{\text{X}}(q, t_0)} + P_2(\cos\theta_q) \frac{\gamma S_2^{\text{exc}}(q, t) + (1-\gamma) S_2^{\text{X}}(q, t)}{S_0^{\text{X}}(q, t_0)}. \end{aligned} \tag{3.20}$$

Note that excitation fraction appears in the isotropic part of the fractional signal change, $S_0(q, t)$, as a multiplicative scaling factor, which can often be treated as a fitting parameter in the analysis of experimental data.

In addition to all practical considerations outlined above, one of the greatest advantages of the fractional signal change is that it shows time-dependent changes on a relative scale. Note that as $q \to 0$ the scattering signal grows fast and is proportional to the number of electrons squared, N_{e}^2, while at larger values of q the signal asymptotically approaches N_{e} [40]. Without the relative scaling, low q values become quite prominent. Similarly, looking at absolute intensity is of little use as the changes brought up by the excitation are usually small, on the order of a few percent. The fraction signal change is the natural way to represent the data, so that it reveals the encoded dynamics in an optimal manner.

3.4 Independent Atom Model

While the expressions derived in Section 3.2 feature the two-electron density of the molecule, it is often impossible or impractical to compute the scattering directly from this quantity. First, it requires knowledge of the electronic wave function of the molecule in all participating states, which is possible to obtain with a reasonable degree of accuracy from the *ab initio* calculation only for small molecules. Second, even the use of optimised algorithms for the computation of the scattering cross-section, such as the one presented in Chapter 4, may be unfeasible for more than a few representative structures; covering all possible conformations in the course of the dynamics might be computationally prohibitive. A common and well-established approach introduced by Debye is to approximate the two-electron density by a sum of atomic form factors [92]. This approximation is known as the Independent Atom Model (IAM). The corresponding form factors are tabulated quantities that can be found in *The International Table of Crystallography* [93].

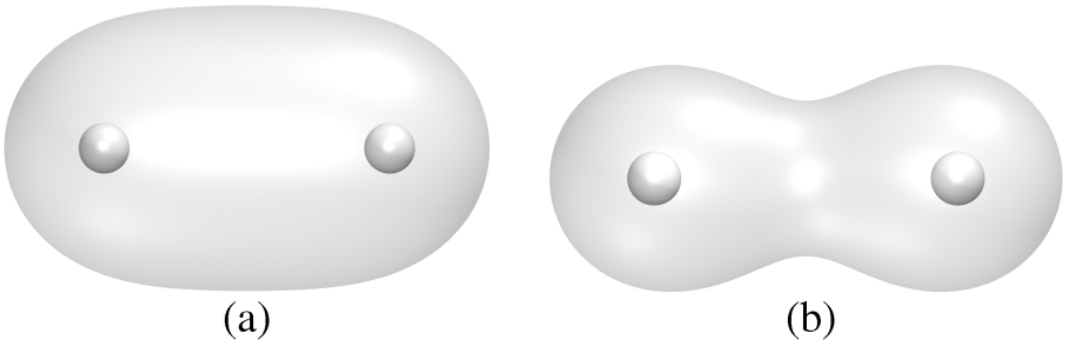

FIGURE 3.3: The electron density of ground state H_2 calculated in two different levels of approximation. (a) shows the *ab initio* density for CAS(2,7)-SCF/aug-cc-pVTZ, while (b) shows the density that corresponds to the Independent Atom Model (IAM). The isosurfaces are shown with a 87% cut off. Reproduced from Ref. [47].

To show the basis of the approximation, we first split the two-electron density into elastic and inelastic terms. We then approximate the diagonal one-electron density, $\rho_{ii}^{(1)}(\mathbf{r}_1, \bar{\mathbf{R}})$, as a sum of spherical atomic densities (see

Figure 3.3), $f_A(r_1)$, centred on the nuclei, A:

$$\rho_{ii}^{(1)}(\mathbf{r}_1, \bar{\mathbf{R}}) = \sum_A \delta\left(\mathbf{r}_1 - \mathbf{R}_A\right) \circledast f_A(r_1), \tag{3.21}$$

where $\circledast$ denotes convolution. Using the Fourier convolution theorem the elastic part of the electronic matrix element $\Lambda_{ii}(\boldsymbol{q}, \bar{\boldsymbol{R}})$ becomes:

$$\begin{aligned} \Lambda_{ii}^{\mathrm{e}}(\boldsymbol{q}, \bar{\boldsymbol{R}}) &= \left| \mathcal{F}\left[\rho_{ii}^{(1)}(\mathbf{r}_1, \bar{\mathbf{R}})\right] \right|^2 = \left| \sum_A e^{i\boldsymbol{q}\cdot\mathbf{R}_A} \tilde{f}_A(q) \right|^2 \\ &= \sum_A \sum_B \tilde{f}_A(q) \tilde{f}_B(q) e^{i\boldsymbol{q}\cdot\mathbf{R}_{AB}}, \end{aligned} \tag{3.22}$$

where $\mathbf{R}_{AB} = \mathbf{R}_A - \mathbf{R}_B$ is the interatomic vector. Many of the tabulated form factors, $\tilde{f}_A(q)$, have been first obtained computationally from the Hartree-Fock wave functions [94–96]. In addition, inelastic Compton corrections, $\tilde{f}_A^{\mathrm{c}}(q)$, are added to the sum in Eq. (3.22) to account for the effect of inelastic scattering. Note that this is necessary because, unlike X-ray crystallography, elastic and inelastic scattering in gas phase are both incoherent and should be treated on an equal footing. The inelastic form factors are completely structureless and isotropic, which means that they are exactly the same for all isomers of a molecule at all times. That implies that these only enter the fractional signal change in Eq. (3.20) via the denominator because of their cancellation in the numerator.

Identically to the derivations in Eq. (3.1)–Eq. (3.12), one can use a plane-wave expansion of the exponent, $\exp\left(i\boldsymbol{q} \cdot \mathbf{R}_{AB}\right)$, in the molecular frame, and then refer that to the laboratory frame via the Euler angles. The differential scattering section again becomes an infinite series of Legendre polynomials, $P_l(\cos\theta_q)$, as expressed in Eq. (3.11), where the expansion coefficients (also

referred to as Legendre amplitudes) are given by:

$$\begin{aligned} S_l(q,t) = \frac{d\sigma_{\mathrm{Th}}}{d\Omega} \int d\tau\ I(\tau - t)\ [\ \sum_A \tilde{f}_A^{\,c}(q)\delta_{l0} + (2l+1)\imath^l \\ \times \sum_{i,j=1}^{N} \langle \theta_i^{\mathrm{r}}(\tau)|P_l(\cos\beta)|\theta_j^{\mathrm{r}}(\tau)\rangle \\ \times \sum_A \sum_B \tilde{f}_A(q)\tilde{f}_B(q)\langle \chi_i^{\mathrm{v}}(\tau)|j_l(qR_{AB})P_l(\cos\theta_{AB})|\chi_j^{\mathrm{v}}(\tau)\rangle\ ]\,, \end{aligned} \tag{3.23}$$

where R_{AB} and θ_{AB} are the radial and angular components of the internuclear distance, $\mathbf{R}_{AB}$. The zeroth and second order terms, whose significance was discussed previously, are now given by:

$$\begin{aligned} S_0(q,t) = \frac{d\sigma_{\mathrm{Th}}}{d\Omega} \int d\tau\ I(\tau - t)\ [\ \sum_A \tilde{f}_A^{\,c}(q) \\ + \sum_{i=1}^{N} \sum_A \sum_B \tilde{f}_A(q)\tilde{f}_B(q)\langle \chi_i^{\mathrm{v}}(\tau)|j_0(qR_{AB})|\chi_i^{\mathrm{v}}(\tau)\rangle\ ]\,, \end{aligned} \tag{3.24}$$

and

$$\begin{aligned} S_2(q,t) = \frac{d\sigma_{\mathrm{Th}}}{d\Omega} \int d\tau\ I(\tau - t)\ (-5) \sum_{i=1}^{N} \langle \theta_i^{\mathrm{r}}(\tau)|P_2(\cos\beta)|\theta_i^{\mathrm{r}}(\tau)\rangle \\ \times \sum_A \sum_B \tilde{f}_A(q)\tilde{f}_B(q)\langle \chi_i^{\mathrm{v}}(\tau)|j_2(qR_{AB})P_2(\cos\theta_{AB})|\chi_i^{\mathrm{v}}(\tau)\rangle, \end{aligned} \tag{3.25}$$

where we have again disregarded coherent mixed scattering. Eq. (3.24) can be seen to arise from the Debye scattering formula. The latter is obtained from Eq. (3.22) in the case of isotropic ensemble. Taking the spherical average over the internuclear distances, $\mathbf{R}_{AB}$, or equivalently in the molecular frame around q, gives:

$$\Lambda^{\mathrm{e}}_{\mathrm{Debye}}(q,\bar{\boldsymbol{R}}) = \sum_A \tilde{f}_A^{\,2}(q) + \sum_A \sum_{B\neq A} \tilde{f}_A(q)\tilde{f}_B(q)\frac{\sin qR_{AB}}{qR_{AB}}, \tag{3.26}$$

since $\langle e^{i\mathbf{q}\cdot\mathbf{R}_{AB}}\rangle = \sin qR_{AB}/(qR_{AB})$.

The IAM approximation is extensively used in crystallography and powder diffraction, and gives satisfactory results when the absolute intensity is needed. However, it has certain limitations. Firstly, it does not account for the true electron density distribution of the molecule. The density is assumed to be isotropically associated with the nuclei and, consequently, electron delocalisation effects are not considered. Valence electrons participating in molecular bonding are not properly accounted for. Secondly, electron density redistribution in the excited states is not captured. Finally, electron correlation effects, implicitly present in the total scattering cross-section via the two-electron correlated density, are not captured. All these effects are subtle and quite small on the scale of the absolute intensity. However, geometrical changes in photochemical processes might also be small, so more accurate treatment may sometimes be needed. On the other hand, electron delocalisation and correlation are interesting aspects of photochemistry in their own right, and the IAM model falls short from being the right tool for their investigation. Chapter 4 provides an example of a computational framework that is more suitable for these purposes.

3.5 Observing Dissociation

In many photochemical processes, the absorbed energy of the photon is enough to overcome dissociation barriers. Dissociation reactions are commonly studied and provide useful information for the bonding in molecules. In UXS, bond breaking leaves a very strong and characteristic signature that we will discuss here briefly.

For simplicity, we will work in the framework of the IAM for isotropic scattering. It is prudent to state the behaviour of elastic and inelastic form factors as the magnitude of the momentum transfer vector, q, changes. Firstly, the inelastic corrections always go to zero at $q = 0$, while, for an atom A, they go to the number of electrons, N_A, as q increases. The elastic scattering form factor on the other hand goes to N_A^2 at $q = 0$ and tends to zero at large q [40]. For a collection of n identical atoms, or coarse-grained particles, described by a form factor, $\tilde{f}_A(q)$, the scattering signal is given by Eq. (3.26)

in the general case. However, at $q = 0$ the interference term equals unity, $\sin(qR_{AB})/(qR_{AB}) = 1$, so that:

$$\Lambda^{\mathrm{e}}(0, \bar{\boldsymbol{R}}) = \sum_A \tilde{f}_A^{\,2}(0) + \sum_A \sum_{B \neq A} \tilde{f}_A(0)\tilde{f}_B(0) = \left(\sum_A \tilde{f}_A(0) \right)^2 = (nN_A)^2. \tag{3.27}$$

In other words, the scattered intensity in the direction of the incoming beam is proportional to the square of the electrons in the beam path. However, the dilute gas phase is characterised by large intermolecular distances. Hence, as the scattering vector moves away from zero, the observed intensity rapidly becomes proportional to the number of atoms in the beam path instead:

$$\Lambda^{\mathrm{e}}(q, \bar{\boldsymbol{R}}) = \sum_A \tilde{f}_A^{\,2}(q) = n\tilde{f}^{\,2}(q), \tag{3.28}$$

because $\sin(qR_{AB})/(qR_{AB}) \to 0$ as $R_{AB} \to \infty$. Essentially, within all experimentally observed scattering angles, the signal obeys Eq. (3.28), *i.e.* it is an incoherent sum of the species in the beam path. As a molecule dissociates, the two fragments effectively become separate species and the interference between them is lost. For a diatomic AB, as $R_{AB} \to \infty$, the interference term goes to zero, $\sin(qR_{AB})/(qR_{AB}) \to 0$, so that:

$$\Lambda^{\mathrm{e}}(q, \boldsymbol{R}_A, \boldsymbol{R}_B) = \tilde{f}_A^{\,2}(q) + \tilde{f}_B^{\,2}(q). \tag{3.29}$$

This means that at small but nonzero values of the momentum transfer vector, the scattering signal becomes proportional to $N_A^2 + N_B^2$, while for the undissociated molecule it is proportional to $(N_A + N_B)^2$. The intensity has been reduced by $2N_AN_B$ for each dissociated molecule. This characteristic drop is a clear sign of dissociation in the experiments, and can even be used to infer reaction rates, as demonstrated in Chapter 7.

3.6 Direct Inversion Schemes

A question of paramount importance is how to extract the information for the photochemical dynamics in real space from the total scattering signal. We will again focus on the isotropic scattering component, for which we can rewrite Eq. (3.13) as:

$$S_0(q,t) = \frac{d\sigma_{\mathrm{Th}}}{d\Omega}\left[N_{\mathrm{e}} + \int dr P(r,t)\frac{\sin qr}{qr}\right], \tag{3.30}$$

where $P(r)$ is the radial distribution function of interelectron distances averaged over electronic states and nuclear motion during the course of the X-ray pulse:

$$P(r,t) = r^2 \int_0^{\pi} d\theta_r \sin\theta_r \int_0^{2\pi} d\phi_r \sum_i^N \int d\tau\; I(\tau - t)\; \langle \chi_i^{\mathrm{v}}(\tau)|2\rho_{ii}^{(2)}(\boldsymbol{r},\bar{\boldsymbol{R}})|\chi_i^{\mathrm{v}}(\tau)\rangle. \tag{3.31}$$

In Eq. (3.31), θ_r and ϕ_r are the polar and azimuthal angles of the interelectron vector, $\mathbf{r} = \mathbf{r}_1 - \mathbf{r}_2$. $P(r,t)$ is a real physical observable and gives the probability of finding one electron at a distance r from another electron given the spread of nuclear configurations encoded in the nuclear wave packet, $|\chi_i^{\mathrm{v}}(\tau)\rangle$. For a short X-ray pulse and a localised wave packet, the radial distribution function characterises the electron distribution in what is classically perceived as the molecular structure. Mathematically, it can be extracted from the observed isotropic signal by a sine transformation [41]:

$$P(r,t) = \frac{2}{\pi}\int_0^{\infty} dq \left[S_0(q,t)\left(\frac{\sigma_{\mathrm{Th}}}{d\Omega}\right)^{-1} - N_{\mathrm{e}}\right] qr \sin qr. \tag{3.32}$$

Eq. (3.32) is quite a powerful statement. It means that the total X-ray scattering in gas phase provides direct access to the correlated instantaneous electron density of the molecule. In addition to providing the means for tracking structure evolution from the perspective of the electrons, it allows electron correlation effects to be studied experimentally [41, 42, 97, 98]. Unfortunately, there are two aspects that severely limit the applications of Eq. (3.32).

The first one is more fundamental and relates to the simple fact that $P(r)$ is a one-dimensional function. While some information about the three-dimensional structure of the two-electron density is retained, the rotational average in Eq. (3.31) certainly makes its extraction non-trivial. The full dimensionality of the problem has been projected onto a single radial component. This should be considered equivalent to the phase problem in X-ray crystallography. Methods for extraction via iterative procedures have been suggested in the literature, but have been shown not to be unique unless some meaningful constraints have been adopted [99, 100].

The second limitation is more technical. Current XFEL experiments suffer from a limited q-range. The accessible scattering vector rarely goes above 4-5Å^{-1} . Given the uncertainty relationship between the scattering range and the spatial resolution, $\sigma_q \sigma_r \approx \pi$, the ability to extract well-resolved radial distributions functions from experiments is rather limited. Certain large charge movements could be observed via $P(r,t)$, but small changes in bond lengths or angles cannot be resolved.

Given those limitations, it is often practical to rely on some sort of synergistic approach between theoretical or computational modelling and data fitting to explain the experimental findings. Such methods are presented in Chapters 6 and 7. Theory can provide suitable constrains on molecular motion and structural freedom that can overcome the issue of real-space resolution described above. Essential to success is the existence of computational tools that can reliably simulate the scattering signal, so that data fitting can be performed in the scattering space, eliminating the problematic inversion to real space via the sine transformation in Eq. (3.32).

Chapter 4

Computational Methods

4.1 Overview

Obtaining accurate energies and the associated electronic structure in atoms and molecules by solving the TISE in Eq. (2.4) for the clamped-nuclei Hamiltonian is the central objective of quantum chemistry. Since an exact solution is not possible, the world of *ab initio* chemistry is bursting with approximations. The first part of this chapter briefly describes some of the common techniques encountered later in the thesis. Calculating the electronic structure of the molecule is only the first step in simulating the scattering cross-section. Here, a method for calculating generalised (elastic, inelastic, total and coherent mixed) isotropic cross-sections starting from the wave function of the molecule is presented. It is both fast and free from approximations beyond those made in obtaining the electron density of the molecule.

4.2 Electronic Structure Calculations

This section briefly covers the foundations of electronic structure methods. A more comprehensive discussion can be found in many standard textbooks such as Ref. [101] and Ref. [102]. In *ab initio* chemistry, the total electronic wave function is made up of single-electron wave functions, $\phi(\mathbf{r})$, called orbitals. These give the probability of finding an electron in a given region of space. Obviously, the form of the molecular Hamiltonian (Eq. (2.72)) implies that the electronic TISE is a many-body problem, where the motion of the individual electrons is correlated by the action of the electron-electron

repulsion term. Furthermore, electrons are fermions, which means that the total wave function must obey the Pauli principle:

$$\psi(\mathbf{r}_1, \ldots, \mathbf{r}_i, \ldots, \mathbf{r}_j, \ldots, \mathbf{r}_n) = -\psi(\mathbf{r}_1, \ldots, \mathbf{r}_j, \ldots, \mathbf{r}_i, \ldots, \mathbf{r}_n), \tag{4.1}$$

that is, the wave function must be antisymmetric with respect to particle interchange. This is related to the notion of electron spin. The natural representation of the total wave function that fulfils the fermion asymmetry is the Slater determinant:

$$\psi\left(\mathbf{r}_1, \mathbf{r}_2, \ldots, \mathbf{r}_n\right) = \frac{1}{\sqrt{N_\mathrm{e}!}} \begin{vmatrix} \varphi_1\left(\mathbf{r}_1\right) & \varphi_2\left(\mathbf{r}_1\right) & \ldots & \varphi_n\left(\mathbf{r}_1\right) \\ \varphi_1\left(\mathbf{r}_2\right) & \varphi_2\left(\mathbf{r}_2\right) & \ldots & \varphi_n\left(\mathbf{r}_2\right) \\ \varphi_1\left(\mathbf{r}_3\right) & \varphi_2\left(\mathbf{r}_3\right) & \ldots & \varphi_n\left(\mathbf{r}_3\right) \\ \cdot & \cdot & \cdot & \cdot \\ \varphi_1\left(\mathbf{r}_n\right) & \varphi_2\left(\mathbf{r}_n\right) & \ldots & \varphi_n\left(\mathbf{r}_n\right) \end{vmatrix}. \tag{4.2}$$

Here, $\varphi(\mathbf{r})$ are spin orbitals – products of a spatial orbital and a spin wave function (spin-up or spin-down). From the properties of determinants, interchanging two electrons (rows) reverses its sign. If two orbitals (columns) are the same, the determinant vanishes in accordance with the fact that two electrons cannot share the same quantum state.

4.2.1 Hartree-Fock Self-Consistent Field

Obtaining approximate solutions for the spin orbitals in atoms and molecules is the key goal of electronic structure calculations. While there are many possible approaches with varying degrees of accuracy and complexity, the work presented in this thesis features only a small number of them. Conceptually, the simplest is the Hartree-Fock (HF) method, in which the exact wave function is represented by a single Slater determinant. In essence, the HF approximation takes the many-body problem defined in the electronic Hamiltonian and breaks it down into a set of coupled one-electron equations, whose eigenfunctions are the spin orbitals. The coupling, that originates from the electron-electron repulsion term, is treated in an average,

mean-field, manner. The solutions of these equations are obtained iteratively by the application of the variational principle, which states that the exact energy is never going to be larger than the expectation value of the Hamiltonian for a given trial wave function, $|\psi_{\text{trial}}\rangle$:

$$\frac{\langle\psi_{\text{trial}}|\hat{H}|\psi_{\text{trial}}\rangle}{\langle\psi_{\text{trial}}|\psi_{\text{trial}}\rangle} = E_{\text{trial}} \geq E_{\text{exact}}. \tag{4.3}$$

The procedure can be summarised as follows. A trial set of spin-orbitals is generated, and used to construct a mean-field potential energy of an electron in the presence of the other $N_e - 1$ electrons. The HF equations are solved to provide a revised set of spin-orbitals. These are used to refine the mean-field potential, and so on, until convergence to a self-consistent solution within a given tolerance. The spin-orbitals obtained in this way are orthogonal and associated with eigenvalues that give the individual single-orbital energies. The HF Slater determinant for the ground state is formed by populating the lowest N_e spin-orbitals with the electrons of the system. The rest of the orbitals are deemed virtual and are not populated.

In practice, the variational procedure that is the heart of the HF method is performed by expanding the spin orbitals in a finite set of spatial basis functions. Introducing the expansion into the HF equations leads to a matrix eigenvalue problem – the so called Roothan-Hall equations. Finding the spin orbitals is then reduced to optimising the expansion coefficients within the given basis set. The finite size of the basis set effectively puts a limit to the number of spin orbitals that can be formed.

4.2.2 Gaussian-Type Orbitals

One of the most popular methods for expanding the spin orbitals is to use Gaussian type functions. Their advantage is that a product of two Gaussians is another Gaussian centred between them. That greatly simplifies the analytical evaluation of two-electron integrals that involve multiple centres. Their main disadvantage is that Gaussians are generally a poor approximation for the spatial extent, shape and asymptotic behaviour of one-electron wave functions. As a consequence, a larger number of basis functions needs

to be used for an adequate accuracy in the calculation compared to *e.g.* Slater-type orbital basis. Within a Gaussian basis set of N_{bf} basis function, the spatial orbital $\phi_a(\boldsymbol{r}_1)$ is given by:

$$\begin{aligned}\phi_a(\boldsymbol{r}_1) &= \sum_{\mu}^{N_{\text{bf}}} M_{\mu}^{(a)} g_{\mu}(\boldsymbol{r}) \\ &= \sum_{\mu}^{N_{\text{bf}}} M_{\mu}^{(a)} (x - A_{\mu,x})^{l_\mu} (y - A_{\mu,y})^{m_\mu} (z - A_{\mu,z})^{n_\mu} e^{-\gamma_\mu (\boldsymbol{r} - \boldsymbol{A}_\mu)^2},\end{aligned} \tag{4.4}$$

where $\boldsymbol{A}_\mu$ is the centre of the μ^{th} Gaussian, and $M_{\mu}^{(a)}$ denotes the expansion coefficient for that orbital. The sum of l_μ, m_μ and n_μ specifies the orbital angular momentum. In order to minimise the large number of independent expansion coefficients optimised in the variational procedure, it is common to use contracted Gaussian functions, which more closely resemble atomic orbitals. A contracted Gaussian is a linear combination of un-contracted Gaussians, known as primitives. The contraction coefficients are held constant and not optimised. Each primitive Gaussian can participate in a number of contractions. In reference to Eq. (4.4), the expansion coefficient $M_{\mu}^{(a)}$ should then be understood as a product of the molecular and the contraction coefficients, or a sum thereof if the primitive participates in more than one contraction.

There is a number of families of Gaussian basis sets available to use in electronic structure packages. Out of those, three are used in this work – STO-*N*G, Pople and Dunning basis sets. The STO-*N*G is a family of minimal basis sets. Each atomic orbital is represented by one contracted Gaussian made up of *N* primitives, which are combined in such a way that they resemble Slater type orbitals (STO). Minimal basis sets are inexpensive to use but rarely do they provide accurate results. In order to improve the accuracy, two (contracted) functions can be used for each atomic orbital. Such basis sets are termed double-zeta. Similarly, triple-zeta basis sets describe each atomic orbital by three contracted Gaussians, quadruple-zeta – by four, and so on. A compromise between accuracy and computational demands is achieved by using split-valence basis sets such as those proposed by Pople

and colleagues. For example, for a Pople double-zeta basis set (denoted as *X*-*YZ*G) only the valence atomic orbitals are represented by two contracted Gaussians – one with *Y* primitives, and another with *Z*. The core atomic orbitals are represented by a single contracted Gaussian, which comprises *X* primitives. This can be generalised to triple-zeta, quadruple-zeta, and so on. To enhance performance, diffuse functions (indicated by + before the letter G) and polarisation functions (indicated by * after the letter G) are often used to supplement the basis set to better account for electron delocalisation and asymmetric electron distributions, respectively. Usually these are applied only to heavy atoms but, if required, they can be applied to hydrogen atoms as well, which is denoted by a double plus (++) and double asterisk (**). Lastly, the Dunning basis sets are commonly utilised in post-HF calculations. They are designed to converge smoothly and more rapidly in such cases. They are abbreviated as cc-pv*N*Z, where "cc" stands for correlation consistent, "p" stands for polarisation functions, and *N*Z states for double-zeta, triple-zeta, etc. If present, the prefix "aug-" denotes that the basis set has been augmented with diffuse functions.

4.2.3 Multiconfigurational and Multireference Methods

The drawback of HF calculations is that they use a single determinant, which fails to describe electron correlation beyond the mean-field. More specifically, the probability of finding one electron at $\mathbf{r}_1$ while another one with the same spin is at $\mathbf{r}_2$ is not conditional; it is given by the product of the independent probabilities. The Slater determinant only accounts for the so-called exchange correlation, which nulls the probability of finding electrons with parallel spin in the same point in space. In practice, the difference between the exact energy and the HF energy is termed the correlation energy, and accounts for the fact that the motion of one electron is influenced by the others. The goal of a plethora of post-HF methods is to account for this missing correlation.

For an infinite basis set, all possible Slater determinants form a complete space, so that any arbitrary function of the electronic coordinates can be expanded as a linear combination of determinants. That includes the exact

electronic ground state or any excited state. In practice, basis sets have a finite size, which means that the determinants do not form a complete basis. Nevertheless, expansion of the electronic wave function as a linear combination of the available determinants is exact within the given subspace. The procedure is called full configuration interaction (CI), and in terms of the HF determinant, $\psi_0(\bar{\mathbf{r}})$, it can be written as:

$$\psi(\bar{\mathbf{r}}) = c_0\psi_0(\bar{\mathbf{r}}) + \sum_{\alpha,a} c_\alpha^a \psi_\alpha^a(\bar{\mathbf{r}}) + \sum_{\substack{\alpha<\beta \\ a<b}} c_{\alpha\beta}^{ab}\psi_{\alpha\beta}^{ab}(\bar{\mathbf{r}}) \ldots, \tag{4.5}$$

where $\psi_\alpha^a(\bar{\mathbf{r}})$ denotes excitation from orbital α to a in the HF determinant, $\psi_{\alpha\beta}^{ab}(\bar{\mathbf{r}})$ denotes double excitation from α and β to a and b, and so on. The c are expansion coefficients. As one might expect, full CI quickly becomes impractical given the total number of determinants in the expansion (N_e-combinations from a set of 2M spin orbitals). Truncated CI methods are developed to alleviate the scaling problem, where only certain excitations are considered, *e.g.* only singly-excited determinants (CIS) or singly- and doubly-excited (CISD).

Finally, it should be pointed out that it is often possible or convenient to work with configuration state functions (CSFs) instead of Slater determinants. CSFs are symmetry-adapted linear combinations of Slater determinants that are eigenstates of the total spin operator.

In the case of CI, the molecular expansion coefficients in Eq. (4.4) are only calculated at the HF level, and kept fixed in the CI procedure, which only varies the expansion coefficients in Eq. (4.5). There will be no gain in accuracy if the orbitals are optimised, since obtaining the correct CI coefficients (in the limit of full CI) gives the exact solution. However, for truncated CI the situation changes. By allowing simultaneous optimisation of both sets of coefficients, one can significantly reduce the number of determinants (or CSFs) and still obtain an adequate solution for the ground

and the excited state wave functions. This approach is termed multiconfiguration self-consistent field (MCSCF). Amongst the possible ways to select determinants for a MCSCF calculation, the complete active-space self-consistent field method (CASSCF) stands out as crucially important for excited states. In CASSCF, a subset of electrons are deemed active, and all determinants (CSFs) that arise from distributing those electrons into a subset of orbitals are considered. These orbitals, some occupied and some virtual in the ground-state HF Slater determinant, are said to belong to the active space. The selection of the orbitals is a form of art; a skilled computational chemist derives inspiration from their knowledge of the reaction or process at hand. Multiple electronic states can be computed simultaneously using a state-average procedure (SA-CASSCF), so that the states share the same orbitals and only differ in their CI expansion.

The limitation of CASSCF is that it does not fully account for electron correlation. The expansion with multiple determinants takes care of static correlation, *e.g.* the part of the correlation that originates from configurations nearly degenerate to the HF determinant. The remaining correlation is dynamic. It relates to the correlated motion of the electrons. Two popular methods that improve upon CASSCF to include dynamic correlation are multireference configuration interaction (MRCI) and second order complete active space perturbation theory (CASPT2). Unlike CASSCF, where the HF determinant is the sole reference function to generate excited determinants, these methods are multireference in nature. Multiple CSFs, usually from a preceding CASSCF calculation, are used as a starting point.

In MRCI, excited CSFs are generated from those reference configurations (for example, singly-excited or singly- and doubly-excited). These are then used in a CI calculation. Once the reference CASSCF has been performed, the MRCI calculation is relatively straightforward, despite being computationally demanding. As it includes highly excited determinants, MRCI often captures a lot of the remaining dynamic correlation. Thus, it is commonly the highest-level theory affordable in many practical situations. Somewhat

less demanding, CASPT2 is a multireference perturbative approach, originally designed for a single wave function [103, 104]. It has later been generalised to handle multiple states (MS-CASPT2), thus becoming suitable for regions of conical intersections, where simultaneous treatment of the states is necessary [105].

4.3 Molecular Quantum Dynamics

In Chapter 2, it was shown that solving the TDSE for a molecule after photoexcitation requires the simultaneous description of nuclear and electronic degrees of freedom. The dynamics are non-adiabatic, *i.e.* they evolve on a number of electronic surfaces that are coupled via NACMEs. Solving Eq. (2.76), which governs the nuclear wave packet propagation, is not trivial in the general case, and a number of methods exist to tackle it depending on the demands of the problem. For a system which has a small number of degrees of freedom (for example, diatomics, triatomics or some sort of reduced-dimensionality model), it is possible to numerically propagate the nuclear wave packet on a grid after pre-computing the required PESs and the coupling between them. That quickly becomes impossible for larger molecules where full-dimensionality is required. Algorithms such as Multiconfigurational Time-dependent Hatree (MCTDH) can considerably extend the number of degrees of freedom that can be handled by using a time-dependent set of one-dimensional basis functions [106, 107]. Still, precomputing PESs for more than a few dimensions is not practical. The issue can be eliminated by using *on-the-fly* algorithms, which compute the PES and the coupling as the nuclear dynamics evolve. This way, only relevant regions of the PES are sampled. The computational efficiency of this approach comes at a price. How to represent a nuclear wave function given that we know the PESs only locally? Strategies generally differ in how much and by what means the quantum nature of the nuclear motion is retained. Methods such G-MCTDH [108], vMCG [109], AIMS [110] and MCE [111] approximate the nuclear wave packet by a set of travelling Gaussians following classical trajectories. A certain degree of quantum character is retained

via the generation, spread and interaction between the Gaussian functions.

Unlike those methods, surface hopping offers a simple semi-classical alternative [112]. Here, the quantum nature of the propagation is approximated statistically. A large collection of non-interconnected trajectories is propagated via Newton's equation of motion, where the forces on the atoms are generated from *on-the-fly ab initio* calculations of the local PES. Nuclei remain fully classical and localised. Furthermore, the trajectories are allowed to exist only in a single electronic state at a time. The transitions between the states are realised by "hops" – a jump between two states close in energy, whose probability of occurring is governed by the strength of the NACMEs. In Chapter 6, a popular surface-hopping algorithm called SHARC is used to generate a large collection of molecular geometries that encompass the possible conformational space in the excited states of NMM. In that particular example, the simulated dynamics in terms of nuclear motion and electronic states are completely disregarded; surface-hopping is simply used as a tool to get a sensible pool of geometries.

4.4 *Ab Initio* Isotropic X-ray Scattering

In Chapter 3, the IAM was presented. The IAM *isotropic* scattering cross-section was brought forward by Debye in 1915, and has remained the standard approach ever since. It is applicable to powder, liquid, amorphous, and gas samples, where there is no preferred orientation imposed on the scattering species (*c.f.* crystallography). As discussed previously, in gas-phase UXS experiments, the scattering signal is rarely isotropic on account of the cosine square distribution of excited molecules prepared by the pump laser. However, it has been demonstrated in Section 3.2 that the isotropic component can always be extracted and that it is equivalent, in the limit of the IAM, to the Debye scattering cross-section. Given the historic success of Debye's approach, it might seem at first that the development of new computational tools for UXS is superfluous. However, as explained in Chapter 3, IAM suffers from limitations that are often incompatible with the goals of UXS. These include: not being able to describe valence electrons,

not being able to differentiate between electronic states, and not being able to capture electron correlation correctly. These are all important features of photochemistry. Furthermore, even if those aspects are not considered to be important on their own right, their systematic neglect may lead to erroneous conclusions when looking into photochemical structural dynamics.

Methodologies to simulate isotropic X-ray scattering from first principles have existed even prior to the arrival of UXS. Their goal was the accurate prediction of scattering from ground state molecules in thermal equilibrium in gas phase. It was first shown by Wang and Smith that a direct analytical formula can be obtained if the electronic wave function is expanded in a Gaussian basis [113]. Later, different modifications of this technique aiming to reduce computational time have been suggested [114–116]. The isotropic scattering cross-section can also be obtained by numerical rotational averaging over the Euler angles, either in the laboratory or the molecular frame [50, 52, 117]. Recently, a grid-density method has also been proposed [53].

The algorithm given in this section is an extension of the method devised by Crittenden and Bernard [116]. It was first presented in Ref. [84]. In simple words, it leads to a representation of the scattering as a sum of spherical Bessel functions, where the expansion coefficients are related by a recursive relationship. As compared to previous methods, this leads to higher computational efficiency and the ability to deal with an arbitrary high angular momentum. The algorithm is designed in the most general way possible, thus being applicable to all matrix elements found in Table 2.1 – total, elastic, inelastic and coherent mixed.

The starting point for our discussion is again the electronic matrix element in Eq. (2.105). We have already shown that the isotropic scattering is equivalent to taking the rotational average of this quantity. Instead of performing the averaging in the laboratory frame by rotating the molecule, we will perform it in the molecular frame by rotating the scattering vector, $\boldsymbol{q}$. That leads to the following equations:

$$\Lambda_{ii}(\boldsymbol{q}, \bar{\boldsymbol{R}}) = N_\mathrm{e} + 2\Big\langle \iint d\boldsymbol{r}_1 \, d\boldsymbol{r}_2 \, \rho_{ii}^{(2)}(\boldsymbol{r}_1, \boldsymbol{r}_2, \bar{\boldsymbol{R}}) e^{\imath \boldsymbol{q}\cdot(\boldsymbol{r}_1 - \boldsymbol{r}_2)} \Big\rangle_{\theta_q \phi_q}, \tag{4.6}$$

and

$$\Lambda_{ij}(\boldsymbol{q}, \bar{\boldsymbol{R}}) = 2\Big\langle \iint d\boldsymbol{r}_1\, d\boldsymbol{r}_2\, \rho_{ij}^{(2)}(\boldsymbol{r}_1, \boldsymbol{r}_2, \bar{\boldsymbol{R}}) e^{\imath \boldsymbol{q}\cdot(\boldsymbol{r}_1 - \boldsymbol{r}_2)} \Big\rangle_{\theta_q \phi_q}, \tag{4.7}$$

where Eq. (4.6) gives the total scattering for electronic state i and Eq. (4.7) gives the coherent mixed scattering between states i and $j \neq i$. Similarly, introducing Eq. (2.106) into Eq. (4.6) leads to:

$$\lambda_{ii}(\boldsymbol{q}, \bar{\boldsymbol{R}}) = \Big\langle \iint d\boldsymbol{r}_1\, d\boldsymbol{r}_2\, \rho_{ii}^{(1)}(\boldsymbol{r}_1, \bar{\boldsymbol{R}}) \rho_{ii}^{(1)}(\boldsymbol{r}_2, \bar{\boldsymbol{R}}) e^{\imath \boldsymbol{q}\cdot(\boldsymbol{r}_1 - \boldsymbol{r}_2)} \Big\rangle_{\theta_q \phi_q}, \tag{4.8}$$

and

$$\lambda_{ij}(\boldsymbol{q}, \bar{\boldsymbol{R}}) = \Big\langle \iint d\boldsymbol{r}_1\, d\boldsymbol{r}_2\, \rho_{ij}^{(1)}(\boldsymbol{r}_1, \bar{\boldsymbol{R}}) \rho_{ji}^{(1)}(\boldsymbol{r}_2, \bar{\boldsymbol{R}}) e^{\imath \boldsymbol{q}\cdot(\boldsymbol{r}_1 - \boldsymbol{r}_2)} \Big\rangle_{\theta_q \phi_q}, \tag{4.9}$$

where λ_{ii} denotes the elastic scattering matrix element in state i, and λ_{ij} the individual inelastic scattering matrix element between states i and $j \neq i$. The total inelastic contribution to scattering is given by the sum of all elements λ_{ij}, or equivalently, by the difference between Eq. (4.6) and Eq. (4.8). We are going to evaluate these elements by expanding the corresponding one- and two-electron density functions using Gaussian basis functions. This is performed with the nuclear positions clamped, so we will drop the dependence of these quantities on the nuclear coordinates. If there are N_{MO} occupied molecular orbitals, the electron densities can be written as [75]:

$$\rho_{ij}^{(1)}(\boldsymbol{r}_1) = \sum_{a,b}^{N_{\mathrm{MO}}} D_{ab}^{ij} \phi_a(\boldsymbol{r}_1) \phi_b(\boldsymbol{r}_1), \tag{4.10}$$

and

$$\rho_{ij}^{(2)}(\boldsymbol{r}_1, \boldsymbol{r}_2) = \frac{1}{2} \sum_{a,b,c,d}^{N_{\mathrm{MO}}} d_{abcd}^{ij} \phi_a(\boldsymbol{r}_1) \phi_b(\boldsymbol{r}_1) \phi_a(\boldsymbol{r}_2) \phi_d(\boldsymbol{r}_2), \tag{4.11}$$

where, for $i = j$, the expansion coefficients D_{ab}^{ij} and d_{abcd}^{ij} are elements of the

one- and two-electron reduced density matrices (1- and 2-RDM), respectively. For $i \neq j$, they are referred to as one- and two-electron reduced *transition* density matrix elements. Inserting Eq. (4.10) and Eq. (4.11) in Eq. (4.6)-Eq. (4.9), leads to a set of integrals that have identical structure:

$$K_{ij}(q) = \left\langle \iint d\boldsymbol{r}_1 d\boldsymbol{r}_2 \sum_{a,b,c,d}^{N_{\mathrm{MO}}} z^{ij}_{abcd} \phi_a(\boldsymbol{r}_1)\phi_b(\boldsymbol{r}_1)\phi_c(\boldsymbol{r}_2)\phi_d(\boldsymbol{r}_2) e^{\imath \boldsymbol{q}\cdot(\boldsymbol{r}_1-\boldsymbol{r}_2)} \right\rangle_{\theta_q \phi_q}, \tag{4.12}$$

where

$$z^{ij}_{abcd} = \begin{cases} d^{ii}_{abcd}, & \text{total } (i=j) \\ D^{ii}_{ab} D^{ii}_{cd}, & \text{elastic } (i=j) \\ D^{ij}_{ab} D^{ji}_{cd}, & \text{inelastic } (i \neq j) \\ d^{ij}_{abcd}. & \text{coherent mixed } (i \neq j). \end{cases} \tag{4.13}$$

Inserting Eq. (4.4), which defines the molecular orbitals in terms of Gaussian basis functions, into Eq. (4.12) leads to:

$$K_{ij}(q) = \sum_{\mu,\nu,\xi,\zeta}^{N_{\mathrm{bf}}} Z^{ij}_{\mu\nu\xi\zeta} \left\langle J_{\mu\nu}(\boldsymbol{q}) J^*_{\xi\zeta}(\boldsymbol{q}) \right\rangle_{\theta_q \phi_q}, \tag{4.14}$$

with the two-electron density $Z^{ij}_{\mu\nu\xi\zeta} = \sum_{a,b,c,d}^{N_{\mathrm{MO}}} z^{ij}_{abcd} M^{(a)}_{\mu} M^{(b)}_{\nu} M^{(c)}_{\xi} M^{(d)}_{\zeta}$. The Fourier integrals over $\boldsymbol{r}_1$ and $\boldsymbol{r}_2$ have been relabelled as $J_{\mu\nu}(\boldsymbol{q})$ and $J^*_{\xi\zeta}(\boldsymbol{q})$, respectively,

$$J_{\mu\nu}(\boldsymbol{q}) = \int d\boldsymbol{r}_1 g_{\mu}(\boldsymbol{r}_1) g_{\nu}(\boldsymbol{r}_1) e^{\imath \boldsymbol{q}\cdot\boldsymbol{r}_1}, \tag{4.15}$$

and

$$J^*_{\xi\zeta}(\boldsymbol{q}) = \int d\boldsymbol{r}_2 g_{\xi}(\boldsymbol{r}_2) g_{\zeta}(\boldsymbol{r}_2) e^{-i\boldsymbol{q}\cdot\boldsymbol{r}_2}. \tag{4.16}$$

It can be seen from the form of Eq. (4.14) that any analytical method for evaluating isotropic scattering from first principles would face the challenge of how to efficiently compute an integral that scales with fourth power of the number of basis functions, N^4_{bf}. Here, similarly to calculating two-electron

integrals in electronic structure packages, the choice of a Gaussian basis set provides great advantages. First, we use the McMurchie-Davidson expansion, which allows us to rewrite the product of two Gaussian basis functions of arbitrary angular momentum as a sum of derivatives of an s-type function [118]:

$$\begin{aligned}\Pi_{\mu\nu}(\boldsymbol{r}) = g_\mu(\boldsymbol{r})g_\nu(\boldsymbol{r}) = \mathcal{G}_{\mu\nu}\sum_{L_1=0}^{l_\mu+l_\nu}\sum_{M_1=0}^{m_\mu+m_\nu}\sum_{N_1=0}^{n_\mu+n_\nu} E_{L_1}^{l_\mu l_\nu} E_{M_1}^{m_\mu m_\nu} E_{N_1}^{n_\mu n_\nu} \\ \times \left(\frac{\partial}{\partial P_x}\right)^{L_1}\left(\frac{\partial}{\partial P_y}\right)^{M_1}\left(\frac{\partial}{\partial P_z}\right)^{N_1} e^{-\gamma_P(\boldsymbol{r}-\boldsymbol{P})^2}.\end{aligned} \tag{4.17}$$

The McMurchie-Davidson expansion coefficients, $E_L^{l_\mu l_\nu}(x_\mu, x_\nu, \gamma_\mu, \gamma_\nu)$, implicitly depend on the Cartesian components of the centres of the Gaussian functions x_μ and x_ν and the exponents γ_μ and γ_ν. Eq. (4.17) uses the following definitions that originate from the Gaussian product theorem:

$$\begin{aligned}\gamma_P &= \gamma_\mu + \gamma_\nu, \\ \mathcal{G}_{\mu\nu} &= e^{-(\gamma_\mu\gamma_\nu/\gamma_P)(\boldsymbol{A}-\boldsymbol{B})^2}, \\ \boldsymbol{P} &= (\gamma_\mu\boldsymbol{A} + \gamma_\nu\boldsymbol{B})/\gamma_P.\end{aligned} \tag{4.18}$$

The existence of a recursive formula between the McMurchie-Davidson expansion coefficients makes their evaluation particularly efficient, and is the reason why they are routinely used in *ab initio* calculations. Inserting $\Pi_{\mu\nu}(\boldsymbol{r})$ into the expression for $J_{\mu\nu}(\boldsymbol{q})$ in Eq. (4.15), and taking the derivative outside the integral, leads to:

$$\begin{aligned}J_{\mu\nu}(\boldsymbol{q}) = \int d\boldsymbol{r}\,\Pi_{\mu\nu}(\boldsymbol{r})e^{\imath\boldsymbol{q}\cdot\boldsymbol{r}} = \mathcal{G}_{\mu\nu}\sum_{L_1=0}^{l_\mu+l_\nu}\sum_{M_1=0}^{m_\mu+m_\nu}\sum_{N_1=0}^{n_\mu+n_\nu} E_{L_1}^{l_\mu l_\nu} E_{M_1}^{m_\mu m_\nu} E_{N_1}^{n_\mu n_\nu} \\ \times \left(\frac{\partial}{\partial P_x}\right)^{L_1}\left(\frac{\partial}{\partial P_y}\right)^{M_1}\left(\frac{\partial}{\partial P_z}\right)^{N_1}\int d\boldsymbol{r} e^{-\gamma_P(\boldsymbol{r}-\boldsymbol{P})^2}e^{\imath\boldsymbol{q}\cdot\boldsymbol{r}}.\end{aligned} \tag{4.19}$$

Furthermore, the Fourier integral of a zero angular momentum Gaussian is just another Gaussian in momentum space,

$$\int d\boldsymbol{r} e^{-\gamma_P(\boldsymbol{r}-\boldsymbol{P})^2} e^{\imath \boldsymbol{q}\cdot\boldsymbol{r}} = \left(\frac{\pi}{\gamma_P}\right)^{3/2} e^{-q^2/4\gamma_P} e^{\imath \boldsymbol{q}\cdot\boldsymbol{P}}, \tag{4.20}$$

where the Fourier shift property has been used to account for the centre of the basis function. Assembling the two-electron integral $J_{\mu\nu}(\boldsymbol{q})J^*_{\xi\zeta}(\boldsymbol{q})$, which will later be spherically-averaged, results in:

$$\begin{aligned} J_{\mu\nu}(\boldsymbol{q})J^*_{\xi\zeta}(\boldsymbol{q}) &= \int d\boldsymbol{r}_1 \Pi_{\mu\nu}(\boldsymbol{r}_1) e^{\imath \boldsymbol{q}\cdot\boldsymbol{r}_1} \int d\boldsymbol{r}_2 \Pi_{\xi\zeta}(\boldsymbol{r}_2) e^{-i\boldsymbol{q}\cdot\boldsymbol{r}_2} \\ &= \frac{\pi^3 \mathcal{G}_{\mu\nu}\mathcal{G}_{\xi\zeta}}{(\gamma_P\gamma_Q)^{3/2}} e^{-q^2(1/\gamma_Q+1/\gamma_P)/4} \sum_{L_1=0}^{l_\mu+l_\nu} \sum_{M_1=0}^{m_\mu+m_\nu} \sum_{N_1=0}^{n_\mu+n_\nu} \sum_{L_2=0}^{l_\xi+l_\zeta} \sum_{M_2=0}^{m_\xi+m_\zeta} \sum_{N_2=0}^{n_\xi+n_\zeta} \\ &\quad \times E_{L_1}^{l_\mu l_\nu} E_{M_1}^{m_\mu m_\nu} E_{N_1}^{n_\mu n_\nu} E_{L_2}^{l_\xi l_\zeta} E_{M_2}^{m_\xi m_\zeta} E_{N_2}^{n_\xi n_\zeta} F_{L_1M_1N_1}^{L_2M_2N_2}(\boldsymbol{q},\boldsymbol{P},\boldsymbol{Q}), \end{aligned} \tag{4.21}$$

where

$$\begin{aligned} &F_{L_1M_1N_1}^{L_2M_2N_2}(\boldsymbol{q},\boldsymbol{P},\boldsymbol{Q}) = \\ &\left(\frac{\partial}{\partial P_x}\right)^{L_1} \left(\frac{\partial}{\partial P_y}\right)^{M_1} \left(\frac{\partial}{\partial P_z}\right)^{N_1} \left(\frac{\partial}{\partial Q_x}\right)^{L_2} \left(\frac{\partial}{\partial Q_y}\right)^{M_2} \left(\frac{\partial}{\partial Q_z}\right)^{N_2} e^{\imath \boldsymbol{q}\cdot(\boldsymbol{P}-\boldsymbol{Q})}. \end{aligned} \tag{4.22}$$

Relabelling $\boldsymbol{H} = \boldsymbol{P} - \boldsymbol{Q}$, as well as $L = L_1 + L_2$, $M = M_1 + M_2$, and $N = N_1 + N_2$, Eq. (4.22) can be written as,

$$F_{L_1M_1N_1}^{L_2M_2N_2}(\boldsymbol{q},\boldsymbol{P},\boldsymbol{Q}) = (-1)^{L_2+M_2+N_2} \left(\frac{\partial}{\partial H_x}\right)^{L} \left(\frac{\partial}{\partial H_y}\right)^{M} \left(\frac{\partial}{\partial H_z}\right)^{N} e^{\imath \boldsymbol{q}\cdot\boldsymbol{H}}. \tag{4.23}$$

As a side note, for a perfectly aligned molecule in space there is no need to perform the rotational averaging, so that Eq. (4.23) is given by:

$$\begin{aligned} F_{L_1M_1N_1}^{L_2M_2N_2}(\boldsymbol{q},\boldsymbol{H}) &= (-1)^{L_2+M_2+N_2} \left(\frac{\partial}{\partial H_x}\right)^{L} \left(\frac{\partial}{\partial H_y}\right)^{M} \left(\frac{\partial}{\partial H_z}\right)^{N} e^{\imath \boldsymbol{q}\cdot\boldsymbol{H}} \\ &= (-1)^{L_2+M_2+N_2} (\imath q_x)^L (\imath q_y)^M (\imath q_z)^N e^{\imath \boldsymbol{q}\cdot\boldsymbol{H}}. \end{aligned} \tag{4.24}$$

Despite being complex-valued, Eq. (4.24) is relatively easy to compute as the coordinates of the centres of the Gaussians only enter via the exponential. Conveniently, in the isotropic scattering case the only term in Eq. (4.23) affected by the integration over angular components of the scattering vector is $\exp[\imath \boldsymbol{q} \cdot \boldsymbol{H}]$. The utility of the McMurchie-Davidson derivatives now becomes clear. For computational convenience and numerical stability, the evaluation of Eq. (4.23) is divided into two cases. When $H < \epsilon_{\text{cut}}$, where ϵ_{cut} is a small cut-off value, the exponential in Eq. (4.24) is approximately unity so that:

$$\begin{aligned} \left\langle F^{L_2M_2N_2}_{L_1M_1N_1}(\boldsymbol{q}, \boldsymbol{H}) \right\rangle_{\theta_q\phi_q} &= (-1)^{L_2+M_2+N_2} \imath^{L+M+N} \left\langle q_x^L q_y^M q_z^N \right\rangle_{\theta_q\phi_q} \\ &= (-1)^{L_2+M_2+N_2} B_{LMN} (\imath q)^{L+M+N}, \end{aligned} \tag{4.25}$$

which follows directly from Eq. (4.24) and where,

$$B_{LMN} = \left\langle \sin^{L+M}\theta_q \cos^N \theta_q \cos^L \phi_q \sin^M \phi_q \right\rangle_{\theta_q\phi_q}, \tag{4.26}$$

is a numerical constant. In the case where $H \geq \epsilon_{\text{cut}}$, performing the rotational average results in:

$$\left\langle F^{L_2M_2N_2}_{L_1M_1N_1}(\boldsymbol{q}, \boldsymbol{H}) \right\rangle_{\theta_q\phi_q} = (-1)^{L_2+M_2+N_2} \left(\frac{\partial}{\partial H_x}\right)^L \left(\frac{\partial}{\partial H_y}\right)^M \left(\frac{\partial}{\partial H_z}\right)^N \frac{\sin qH}{qH}. \tag{4.27}$$

In order to go further, we first notice that $\sin qH/qH$ is the zeroth order spherical Bessel function $j_0(qH)$. Performing the derivatives with respect to the Cartesian components of the centre $\boldsymbol{H}$, gives rise to higher order spherical Bessel functions, $j_\beta(qH)$, so that:

$$\begin{aligned} &\left\langle F^{L_2M_2N_2}_{L_1M_1N_1}(\boldsymbol{q}, \boldsymbol{H}) \right\rangle_{\theta_q\phi_q} = \\ &(-1)^{L_2+M_2+N_2} \sum_{p=0}^{L} \sum_{s=0}^{M} \sum_{t=0}^{N} a_L^p(H_x) b_M^s(H_y) c_N^t(H_z) \left(\frac{q}{H}\right)^\beta j_\beta(qH), \end{aligned} \tag{4.28}$$

where $\beta = \lceil (L+M+N-p-s-t)/2 \rceil + p + s + t$ and $\lceil \dots \rceil$ denotes the

ceiling function, which gives the least integer greater than or equal to its argument. Importantly, the expansion coefficients a_L^p, b_M^s, and c_N^t are reminiscent of the well-known Hermite polynomials and obey similar recursive relations (here given for a_L^p),

$$a_L^p(H_x) = \begin{cases} 1, & L = 0,\ p = 0 \\ 0, & L = 1,\ p = 0 \\ -H_x, & L = 1,\ p = 1\,. \\ -a_{L-2}^0(L-1), & L > 1,\ p = 0 \\ -a_{L-1}^{p-1}H_x - a_{L-2}^p(L-1) & L > 1,\ p > 0 \end{cases} \tag{4.29}$$

There are a number of technical points that need to be addressed now. First, the choice of a sensible cut-off value ϵ_{cut} has a twofold significance. It speeds up the calculation because, for $H < \epsilon_{\text{cut}}$, the values of the integral $\left\langle F_{L_1M_1N_1}^{L_2M_2N_2}(\boldsymbol{q},\boldsymbol{H})\right\rangle_{\theta_q\phi_q}$ are independent of the centres of the Gaussian basis functions. This means that they can be precomputed for all allowed values of the angular momentum and easily accessed in the calculation when needed. Also, the cut-off guarantees numerical stability of the algorithm with respect to prohibitively large values of the $(q/H)^\beta$ factor in Eq. (4.28). The recursive relationship for the coefficients a_L^p, b_M^s and c_N^t as well as those for the spherical Bessel functions are a major factor for the computational efficiency of the algorithm. The algorithm also takes advantage of the symmetry of the two-electron integrals, namely $\left\langle J_{\mu\nu}(\boldsymbol{q})J_{\xi\zeta}^*(\boldsymbol{q})\right\rangle_{\theta_q\phi_q} = \left\langle J_{\xi\zeta}(\boldsymbol{q})J_{\mu\nu}^*(\boldsymbol{q})\right\rangle_{\theta_q\phi_q}$ and $J_{\mu\nu}(\boldsymbol{q}) = J_{\nu\mu}(\boldsymbol{q})$.

Further gains can be achieved by considering the contraction scheme of the basis set used. As usual, primitive Gaussians that appear in multiple contractions need to be considered only once. In doing so, the weight $Z_{\mu\nu\xi\zeta}^{ij}$ needs to be modified to reflect the total contribution of the primitive to any molecular orbital. In addition, many basis sets feature functions that share the same exponents. If they are centred on the same atom, they can be treated together as they result in integrals $\left\langle F_{L_1M_1N_1}^{L_2M_2N_2}(\boldsymbol{q},\boldsymbol{H})\right\rangle_{\theta_q\phi_q}$ that share most of their terms. Finally, the number of two-electron integrals can be truncated by implementing a user-controlled cut-off value for the size of

z^{ij}_{abcd}. This amounts to effective reduction of the number of electrons that are Fourier-transformed to momentum space. However, as it is often the case, there could be a large number of integrals with close to negligible contributions. Allowing for a net loss of 0.1% of the electron density can often result in speeding up the calculation by a factor of two with almost no effect on the calculated scattering intensity.

4.4.1 Benchmarking and Scaling

In this subsection, the performance of the algorithm is compared to a previously existing method, and its computational scaling is explored. All calculations are performed on the ammonia molecule, NH_3, using the MOLPRO electronic structure software package [119, 120]. The geometry used was optimised at the CASSCF(10,8)/aug-cc-pVTZ level of theory, where the numbers in the brackets mean that there are 10 active electrons distributed amongst 8 active orbitals. The focus is on total and elastic scattering, *i.e.* the diagonal two-electron and one-electron properties with respect to electronic states, respectively. We note that the scaling of the algorithm for coherent mixed scattering is identical to total scattering; inelastic scattering is identical to elastic scattering.

Three levels of theory were used in this study – HF, CASSCF(10,6) and CASSCF(10,8). The basis sets included were Pople's and Dunning's correlation-consistent basis sets with double-zeta, double-zeta plus diffuse functions, and triple-zeta plus diffuse functions, as well as the STO-3G minimal basis set. The total and elastic fractional signal change was calculated with reference to the CASSCF(10,8)/aug-cc-pVTZ total and elastic scattering, respectively:

$$\Delta S(q) = \frac{I(q) - I_{\mathrm{ref}}(q)}{I_{\mathrm{ref}}(q)}. \tag{4.30}$$

The advantage of using the fraction signal change was discussed in Section 3.3. In order to produce a simple quantity that can be used to compare different calculations, the integral of the absolute values in the range

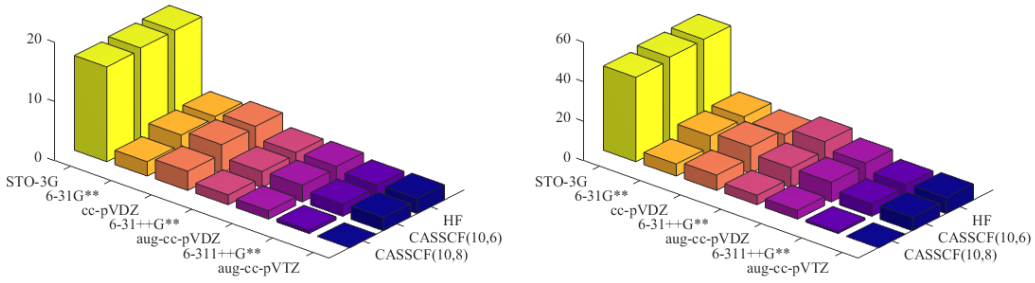

(A) NH_3 total scattering (B) NH_3 elastic scattering

FIGURE 4.1: Convergence of the total and elastic X-ray scattering signals of NH_3. The calculations are performed with with HF, CASSCF(10,6) and CASSCF(10,8) using various basis sets. The height of the bars gives the integral of the percentage intensity change with respect to CASSCF(10,8)/aug-cc-pVTZ total and elastic scattering for the range $0 \leq q \leq 11.34$ Å^{-1}.

$[q_{min}, q_{max}] = [0, 11.34]$ Å^{-1} was calculated as:

$$E = \int_{q_{min}}^{q_{max}} dq \left| \%\Delta S(q) \right|, \tag{4.31}$$

where $\%\Delta S(q)$ is the fractional signal change in percent, *i.e.* $\%\Delta S(q) = \Delta S(q) \times 100\%$. It is worth noting that the behaviour of the absolute total and elastic scattering signals in the limit of large q is different. The former asymptotically tends to the number of electrons in the molecule, while the latter tends to zero. The resulting difference in the value in the denominator in Eq. (4.30) gives rise to a smaller integral in Eq. (4.31) for the case of total scattering. The results for all levels of theory and basis sets are summarised in Fig. 4.1 as well as Table 4.1.

As one might expect, the STO-3G performs quite poorly for calculating scattering, coming close to the IAM ($E = 17.2$ Å^{-1} and $E = 32.8$ Å^{-1} for total and elastic scattering). The two remaining families of basis functions show similar performance at any given level of theory. Interestingly, the Pople basis sets outperform slightly the Dunning ones at the HF level and the smaller active space CASSCF calculation. It can be speculated that the

former provides better description of the electron density in cases where the static electron correlation is not captured adequately. That is supported by the fact that the most significant change in Fig. 4.1 is seen when transitioning from the smaller CASSCF(10,6) to the larger CASSCF(10,8) active space. When comparing the two types of scattering, it is expected that the total scattering is greatly affected by electron correlation, as it is largely a two-electron property. However, slightly surprisingly, elastic scattering also shows a big jump when increasing the active space. This hints that the electron density relaxation associated with static correlation plays a vital role here. However, the effect of the dynamic correlation on the total scattering calculations should not be underestimated. This calls for more advanced *ab initio* methods, which for technical reasons are not used here.

When it comes to computational time and resources, the algorithm exhibits N_{bf}^4 scaling that originates from the permutation over all unique sets of four basis functions. The data presented in Fig. 4.2 and Table 4.1 confirms that. For example, the difference between the smallest and the largest basis set used is as large as three orders of magnitude. It is clear that a careful selection of the basis set is needed if high efficiency is required as this is the rate-determining factor in the calculation. The difference in computational time between elastic and total scattering stems from the nature of the two-electron "charge" density $Z^{ij}_{\mu\nu\xi\zeta}$. For total scattering, this is strictly a two-electron property that reflects the correlation between the electrons, and it has to be evaluated for each unique quadruplet of basis functions *on the fly*. Storing and accessing them is impractical. As the number of orbitals with partial occupancy increases, the cost of computing $Z^{ij}_{\mu\nu\xi\zeta}$ also increases. In the case of elastic scattering, $Z^{ij}_{\mu\nu\xi\zeta}$ can be separated into two independent one-electron charge densities. There are N_{bf}^2 of those, which can be precomputed at a lower computational cost and saved for an efficient use in the calculation. Thus, the calculation of elastic scattering is largely unaffected by the change in the number of occupied orbitals implied by the increase of the level of theory or size of the active space. However, the overhead cost of total scattering is often quite affordable and it might seem reasonable, even when high efficiency is required, to compute directly the total

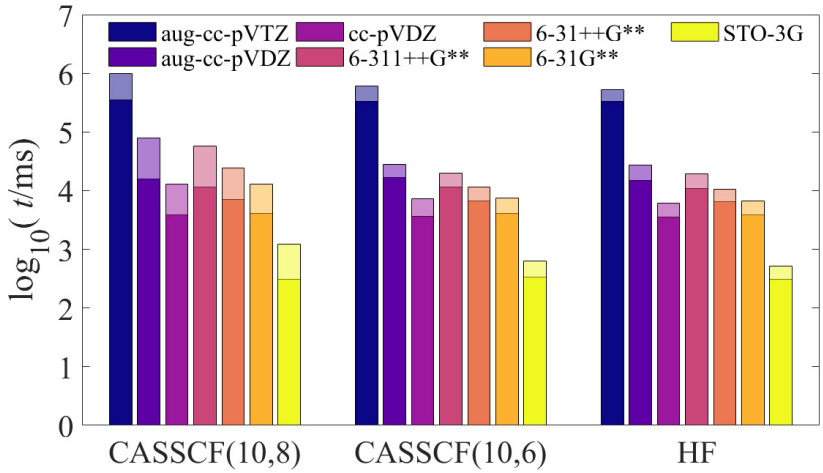

FIGURE 4.2: Computational scaling, expressed as a logarithm of the CPU time in milliseconds, of the algorithm for the *ab initio* calculation of isotropic elastic and total X-ray scattering signals. The calculations are performed for NH_3 using different *ab initio* methods and basis sets. The solid part of the bars gives the elastic scattering, while the shaded area at the top represents the extra time required to compute the total scattering with the same level of theory and basis set.

scattering cross-section, instead of relying on the more common approach of calculating total scattering as a sum of elastic scattering and tabulated inelastic corrections [36, 121, 122].

The results here are presented for a single molecule, so it is not possible to assess the scaling with the size of the molecule. However, it should be pointed out that for small molecules, as described above, combining the evaluation of integrals with identical exponents and origins brings about an improved efficiency. In practice, as the molecule gets larger, the number of the basis function's centres (atoms) also increases, which means that the calculation becomes dominated by terms that cannot benefit from this approach.

The algorithm developed in this chapter was compared against the results published by Hoffmeyer *et al.* [117]. Despite the difference in the

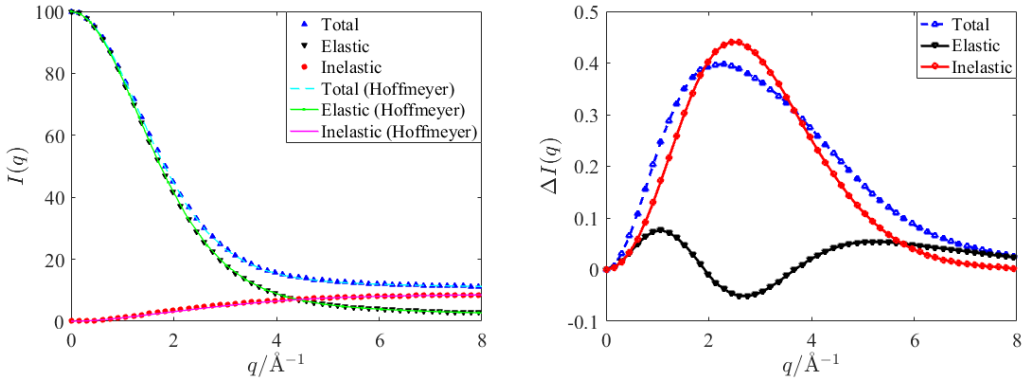

(A) (B)

FIGURE 4.3: Comparison between the method presented in this chapter and the results published by Hoffmeyer *et al.*, who used an MR-SDCI wave function ([5s3p2d/3s2p]) that was numerically integrated on a grid [117]. Total, elastic and inelastic ground-state X-ray scattering for NH_3 are shown. The scattering curves are calculated with CASSCF(10,8)/aug-cc-pVTZ. Subfigure 4.3a shows the total intensity, while subfigure 4.3b shows the difference between our results and those by Hoffmeyer *et al.*

methodology, the two approaches seem to agree reasonably well as indicated by Fig. 4.3, which shows the total, elastic and inelastic scattering intensities. Note that here inelastic scattering refers to the total sum of inelastic contributions, which simply equals the difference between the total scattering and elastic scattering. The following differences in the methods should be emphasised. Hoffmeyer *et al.* use a numerical integration, while the formalism presented here is entirely analytical. Their work relies on a double-zeta basis set with polarisation and diffuse functions, [5s3p2d/3s2p], whereas we employ a larger aug-cc-pVTZ basis set. On the other hand, our best calculation is based on the reference CASSCF(10,8) level of theory, while they report a MR-SDCI (Multi-Reference Single and Double Configuration Interaction) calculation. Unlike CASSCF, MR-SDCI accounts better for dynamic correlation. This has a smaller effect on elastic scattering as seen in Fig. 4.3. However, the total, and hence the inelastic, scattering is more affected by dynamic correlation, which explains the observed discrepancies

between the two methods. Overall, total scattering is expected to be sensitive to electron correlation – something that should be taken into consideration when choosing computational methods to compute this quantity.

TABLE 4.1: The convergence, expressed as the integral, E, of the percentage intensity change with respect to CASSCF(10,8)/aug-cc-pVTZ for the range $0 \leq q \leq 11.34$ Å^{-1}, and the computational CPU time, t, required for the calculation of the isotropic elastic and total X-ray scattering signal in NH_3. Different *ab initio* methods and basis sets are considered.

	CASSCF(10,8)		**CASSCF(10,6)**		**HF**	
	elastic scattering					
Basis set	***t*/s**	***E*/Å^{-1}**	***t*/s**	***E*/Å^{-1}**	***t*/s**	***E*/Å^{-1}**
aug-cc-pVTZ	351.4	0.0	335.4	6.8	332.5	8.1
6-311++G**	15.7	1.0	16.7	6.4	15.1	7.5
aug-cc-pVDZ	3.9	4.4	3.7	10.1	3.6	11.1
6-31++G**	11.5	4.8	11.4	10.0	10.7	14.6
cc-pVDZ	7.1	7.8	6.7	13.6	6.5	10.9
6-31G**	4.1	6.1	4.1	11.7	3.9	12.6
STO-3G	0.3	42.7	0.3	44.3	0.3	44.7
	total scattering					
Basis set	***t*/s**	***E*/Å^{-1}**	***t*/s**	***E*/Å^{-1}**	***t*/s**	***E*/Å^{-1}**
aug-cc-pVTZ	983.0	0.0	605.5	2.3	521.8	2.6
6-311++G**	79.6	0.5	28.3	2.1	27.3	2.4
aug-cc-pVDZ	13.0	1.4	7.3	2.8	6.1	3.1
6-31++G**	57.0	1.7	20.2	2.7	19.3	3.0
cc-pVDZ	24.5	3.2	11.6	4.8	10.7	5.0
6-31G**	12.9	2.4	7.4	4.0	6.6	4.3
STO-3G	1.2	16.0	0.6	16.3	0.5	16.4

Chapter 5

Determining the Orientation of Transition Dipole Moments Using UXS

5.1 Introduction

This chapter presents work which is reproduced with permission from Haiwang Yong, **Nikola Zotev**, Brian Stankus, Jennifer M. Ruddock, Darren Bellshaw, Sébastien Boutet, Thomas J. Lane, Mengning Liang, Sergio Carbajo, Joseph S. Robinson, Wenpeng Du, Nathan Goff, Yu Chang, Jason E. Koglin, Max D. J. Waters, Theis I. Sølling, Michael P. Minitti, Adam Kirrander and Peter M. Weber. "Determining Orientations of Optical Transition Dipole Moments using Ultrafast X-Ray Scattering". *The Journal of Physical Chemistry Letters* **9**, 6556 (2018). Copyright 2019 American Chemical Society.

The theoretical framework presented in Section 2.6 shows that, when an optical laser is resonant with the energy gap between two electronic states, it induces a population transfer between them. The probability of excitation is related to the square of the TDM between the two states. Eq. (2.59) further shows that when a linearly polarised laser is used, the excited state population exhibits a cosine squared distribution with respect to the angle between the polarisation axis of the laser and the relevant TDM. The latter is taken to be the internal frame $\hat{\mathbf{z}}$-axis. This means that we will now

work in the so-called dipole-fixed frame.[1] The coherent excited state rotational wave packet is time dependent and ultimately dephases. However, before doing so the distribution of molecules is anisotropic. As it has been demonstrated in Section 3.2, this spatial anisotropy gives raise to anisotropy in the scattering signal. The scattering anisotropy amplitude, which is defined by Eq. (3.14), can be thought of as arising from the competition between structural rearrangements in the molecule and its rotation in the laboratory frame. At any time, the distribution of orientations and internal motion are intertwined. However, for times shortly after the excitation, rotational dephasing has not yet occurred and the distribution of molecules can be taken to be approximately a cosine squared. This corresponds to a $|\theta_{\mathrm{exc}}|^2 = 3\gamma\cos^2\beta/(8\pi^2)$ TDM distribution for the excited state, which leaves a $|\theta_{\mathrm{gs}}|^2 = (1-3\gamma\cos^2\beta)/(8\pi^2)$ "hole" in the ground state, where γ is the excitation fraction and β is the angle between the TDM and the laser polarisation axis. With reference to Eq. (3.25), the matrix elements over the Euler angles then reduce to:

$$\langle\theta^{\mathrm{r}}_{\mathrm{exc}}|P_2(\cos\beta)|\theta^{\mathrm{r}}_{\mathrm{exc}}\rangle = 0.4\gamma, \tag{5.1}$$

and

$$\langle\theta^{\mathrm{r}}_{\mathrm{gs}}|P_2(\cos\beta)|\theta^{\mathrm{r}}_{\mathrm{gs}}\rangle = -0.4\gamma, \tag{5.2}$$

so that the instantaneous anisotropic amplitude becomes

$$\begin{aligned} S_2(q) = -2\gamma\sum_A\sum_B \tilde{f}_A(q)\tilde{f}_B(q)\,(\,&\langle\chi^{\mathrm{v}}_{\mathrm{exc}}|j_2(qR_{AB})P_2(\cos\theta_{AB})|\chi^{\mathrm{v}}_{\mathrm{exc}}\rangle \\ &- \langle\chi^{\mathrm{v}}_{\mathrm{gs}}|j_2(qR_{AB})P_2(\cos\theta_{AB})|\chi^{\mathrm{v}}_{\mathrm{gs}}\rangle\,)\,. \end{aligned} \tag{5.3}$$

Note that here θ_{AB} denotes the angle between the bond vector $\mathbf{R}_{AB}$ and the TDM in the molecular frame.

The work presented in this chapter deals with the case where the initially excited state is not known. One way to probe the character of this state is to determine the orientation of the TDM in the molecular frame.

[1] As the dipole-fixed frame of reference differs from the molecule frame except for parallel transitions, the angular momentum and hence the rotational motion is not properly described in that frame.

Taking a rough guess at the geometry of the excited state, and combining with the known structure of the ground state, the only parameter that remains unknown in Eq. (5.3) is the distribution of angles between the TDM and the bond vectors. Thus, given that high quality experimental scattering signal is available, and the anisotropy amplitude, $S_2(q)$, can be extracted from it, the direction of the TDM in the molecular frame can be obtained by a straightforward fitting procedure. It should be pointed out that the procedure is not particularly sensitive to the actual geometries used as long as they are not unphysical. In contrast, a $\pi/2$ rotation of the TDM in the molecular frame can completely reverse the sign of the anisotropic amplitude. In simple words, two orthogonal orientations of the molecule in the beam path, would have completely different observed scattering anisotropy. Thus, UXS provides an effective means to determine the directionality of the TDM, effectively supplementing the dynamics encoded in the time-resolved signal.

THE JOURNAL OF PHYSICAL CHEMISTRY Letters

Letter

Cite This: J. Phys. Chem. Lett. 2018, 9, 6556−6562

pubs.acs.org/JPCL

Determining Orientations of Optical Transition Dipole Moments Using Ultrafast X-ray Scattering

Haiwang Yong,[†] Nikola Zotev,[‡] Brian Stankus,[†] Jennifer M. Ruddock,[†] Darren Bellshaw,[‡] Sébastien Boutet,[§] Thomas J. Lane,[§] Mengning Liang,[§] Sergio Carbajo,[§] Joseph S. Robinson,[§] Wenpeng Du,[†] Nathan Goff,[†] Yu Chang,[†] Jason E. Koglin,[§] Max D. J. Waters,[∥] Theis I. Sølling,[∥,#] Michael P. Minitti,[§] Adam Kirrander,*[,‡] and Peter M. Weber*[,†]

[†]Department of Chemistry, Brown University, Providence, Rhode Island 02912, United States

[‡]School of Chemistry, University of Edinburgh, Edinburgh EH9 3FJ, United Kingdom

[§]SLAC National Accelerator Laboratory, Menlo Park, California 94025, United States

[∥]Department of Chemistry, University of Copenhagen, Universitetsparken 5, 2100 Copenhagen, Denmark

Supporting Information

ABSTRACT: Identification of the initially prepared, optically active state remains a challenging problem in many studies of ultrafast photoinduced processes. We show that the initially excited electronic state can be determined using the anisotropic component of ultrafast time-resolved X-ray scattering signals. The concept is demonstrated using the time-dependent X-ray scattering of *N*-methyl morpholine in the gas phase upon excitation by a 200 nm linearly polarized optical pulse. Analysis of the angular dependence of the scattering signal near time zero renders the orientation of the transition dipole moment in the molecular frame and identifies the initially excited state as the $3p_z$ Rydberg state, thus bypassing the need for further experimental studies to determine the starting point of the photoinduced dynamics and clarifying inconsistent computational results.

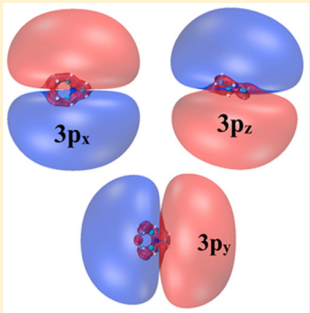

Identification of the initially excited electronic state in ultrafast time-resolved experiments is of paramount importance for analysis of the observed dynamics. Inaccurate assignment can lead to falsely attributed structural changes and to pathways that may not be accessible in the given experiments. Yet accurate assignments remain challenging, especially of the transient electronically excited states that constitute the critical initial step of any photochemical or photophysical process. We demonstrate here a method to assign the excited state via the orientation of the optical transition dipole moment (TDM) in the course of time-resolved, anisotropic X-ray scattering measurements.

Traditionally, TDMs are determined spectroscopically.[1] Experimental techniques such as 1D and 2D IR spectroscopy,[2] fluorescence spectroscopy,[3,4] and photoelectron spectroscopy[5,6] can be used for long-lived states. In addition, related properties such as oscillator strength and excitation energies are often obtained from electronic structure calculations and serve as supporting evidence for pinpointing the initially excited states. However, these strategies do not always provide unambiguous results. On the one hand, the experimental spectra may exhibit broadening that results from either instrumental parameters or the natural line width of the underlying transitions. If the molecular system features an ultrashort-lived state with a lifetime short compared to the rotational period, a molecular frame TDM can be determined from the photofragment angular distributions.[7−12] However, determination of the TDM orientation in other cases remains intractable, while excitation energies, TDMs, and oscillator strengths derived from computations can be associated with large uncertainties,[13,14] not the least in molecules where the initially excited state has Rydberg character and thus highly diffuse orbitals.[15,16] Identification of the initially excited state is therefore a challenging problem.

In this Letter, we illustrate how the aforementioned complications can largely be bypassed in gas-phase ultrafast time-resolved X-ray scattering experiments, which have become possible with the recent development of powerful X-ray Free-Electron Lasers (XFELs). Within a few years of the first X-rays emerging from the Linac Coherent Light Source (LCLS),[17] ultrafast gas-phase X-ray scattering experiments have become a reality, yielding scattering data with high temporal and angular resolution.[18−20] It is now feasible to obtain high-quality two-dimensional scattering signals that reveal alignment and anisotropy in the sample.[21] Thus, in addition to the isotropic signal that reveals the structural dynamics, one can also explore the richness of information hidden in the anisotropy of the time-resolved X-ray scattering patterns. The potential importance of the anisotropic

Received: September 8, 2018
Accepted: October 31, 2018
Published: October 31, 2018

DOI: 10.1021/acs.jpclett.8b02773
J. Phys. Chem. Lett. 2018, 9, 6556−6562

components of X-ray and electron scattering in gas-phase ensembles and the accompanying rotational dynamics is underscored by the fact that they have been studied theoretically for many years.[22−28] Experimental studies of rotational and structural dynamics of gas-phase molecules have also been performed by Yang et al. using time-resolved ultrafast electron diffraction.[29−33] In the present study, we show that for short-lived states in polyatomic molecules, for which TDM orientations are difficult to obtain, the anisotropic scattering signal reveals the identity of the initially prepared state. We investigate the optical excitation of an asymmetric top molecule, *N*-methyl morpholine (NMM) shown in Figure 1, using a 200 nm pump laser pulse in the gas phase and show that the anisotropy near time zero can be used as a quick and reliable tool to determine the initially accessed state.

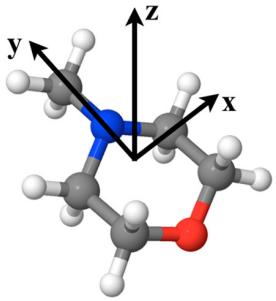

Figure 1. Structure and molecular axes of NMM in the ground state.

The time-resolved molecular dynamics of NMM has previously been explored using Rydberg fingerprint spectroscopy.[34,35] Zhang et al. found that optical excitation at 208 nm prepares the molecule in a 3p state, which then decays via internal conversion on a time scale of about 100 fs to the lower-lying 3s Rydberg state.[35] In the spectrum, they noticed that the 3p peak right after time zero splits into two components, one intense peak with higher binding energy (BE) and one weaker peak at lower BE. On the basis of the relative order of binding energies calculated from self-interaction corrected density functional theory (DFT-SIC), the high BE and the low BE peaks were assigned to the $3p_z$ and $3p_x$ states, respectively. However, this identification of the initially excited state is only as reliable as the supporting computational results. To examine this last point, we show in Table 1 the computational results for the 3p Rydberg states of NMM at three different levels of theory. While the benchmark multireference configuration interaction (MRCI) and complete active space self-consistent field (CASSCF) methods indicate that the most probable excitation is to the $3p_z$ state, time-dependent density functional theory (TDDFT) suggests that it is a $3p_y$ state. It is also worth noting that MRCI and CASSCF calculations suggest that vertical excitation energies are ordered as $3p_z < 3p_x < 3p_y$, but for TDDFT, the order is $3p_x < 3p_y < 3p_z$ (see details in the SI). Because of the inconsistencies in the computational results for challenging cases such as Rydberg-excited molecules, an unambiguous determination of short-lived optically excited states provides a valuable experimental benchmark.

In the time-resolved X-ray scattering experiments, a thermal ensemble of room-temperature gas-phase NMM molecules is excited with a 200 nm pump laser and probed using 9.5 keV X-ray photons generated by the LCLS. The scattering signal is detected on a 2.3 megapixel Cornell-SLAC pixel array detector (CSPAD),[36] and the position of the detected X-rays is converted into polar coordinates on the detector, expressed in terms of the amplitude of the scattering vector **q** and the azimuthal angle ϕ. The optical laser and the X-rays propagate collinearly, and their linear polarizations are perpendicular to each other. The time-evolving patterns are expressed as the percent difference scattering patterns, $P_{\mathrm{diff}}(\phi,q,t)$,

$$P_{\mathrm{diff}}(\phi, q, t) = 100\frac{I_{\mathrm{on}}(\phi, q, t) - I_{\mathrm{off}}(\phi, q)}{I_{\mathrm{off}}(\phi, q)} \quad (1)$$

where $I_{\mathrm{on}}(\phi,q,t)$ represents the scattering pattern at a given pump−probe delay time t and $I_{\mathrm{off}}(\phi,q)$ is the scattering pattern from the ground-state, unexcited molecules, with ϕ the azimuthal angle on the detector and q the momentum transfer. Using the percent difference of the scattering signal helps to cancel poorly defined experimental parameters such as background signals and gas pressure fluctuations. More importantly, the anisotropy due to polarization of the X-rays also cancels out in eq 1,[37] leaving only the anisotropy introduced by the optical pump pulse. The percent difference signal scales with the excitation probability, which is intentionally kept small as to reduce the probability of competing multiphoton excitation processes. Details about the experiments are described in the Supporting Information.

The time-dependent scattering images shown in Figure 2 display a strong anisotropy near time zero, which decays at later times. The isotropic, radial dependence of the percent difference signal encodes the NMM dynamics as the molecule evolves from the ground-state structure to the Rydberg state geometry after the optical excitation. The variation of the scattering signal with the azimuthal angle, i.e., the anisotropy, originates from preferential excitation of molecules whose TDM vector aligns with the polarization of the optical pulse in the laboratory frame. For single-photon excitation, the anisotropy takes a $\cos^2(\theta)$ functional form with respect to the laser polarization axis, where θ is defined as the angle between the molecular TDM vector and the laser polarization vector and ranges from 0 to π.[38] It follows that the intrinsic orientation of the TDM in the molecular frame determines the orientation of the excited-state population of molecules in the laboratory frame, which is captured in the scattering signal near time zero. Because the alignment of excited molecules is determined by the relationship between the TDM vector of the

Table 1. Oscillator Strengths with TDM Directions, Shown as (*x*,*y*,*z*) Unit Vectors, From the Ground State to Each of the Three 3p States in NMM, Calculated at Different Levels of Theory[a]

excited state	CAM-B3LYP/6-311++G(d,p)	SA5-CASSCF(2,5)/6-311+G(d)	MRCI(2,5)/6-311+G(d)
$3p_x$	0.0041 (1, 0, 0)	0.0704 (1, 0, 0)	0.0322 (1, 0, 0)
$3p_y$	0.1159 (0, 0.57, −0.82)	0.0496 (0, 0.84, 0.55)	0.0340 (0, 0.85, 0.52)
$3p_z$	0.0318 (0, 0.15, 0.99)	0.1321 (0, 0.18, −0.98)	0.1138 (0, 0.18, −0.98)

[a]Molecular axes are defined by the three principal rotational axes of NMM (Figure 1).

DOI: 10.1021/acs.jpclett.8b02773
J. Phys. Chem. Lett. 2018, 9, 6556−6562

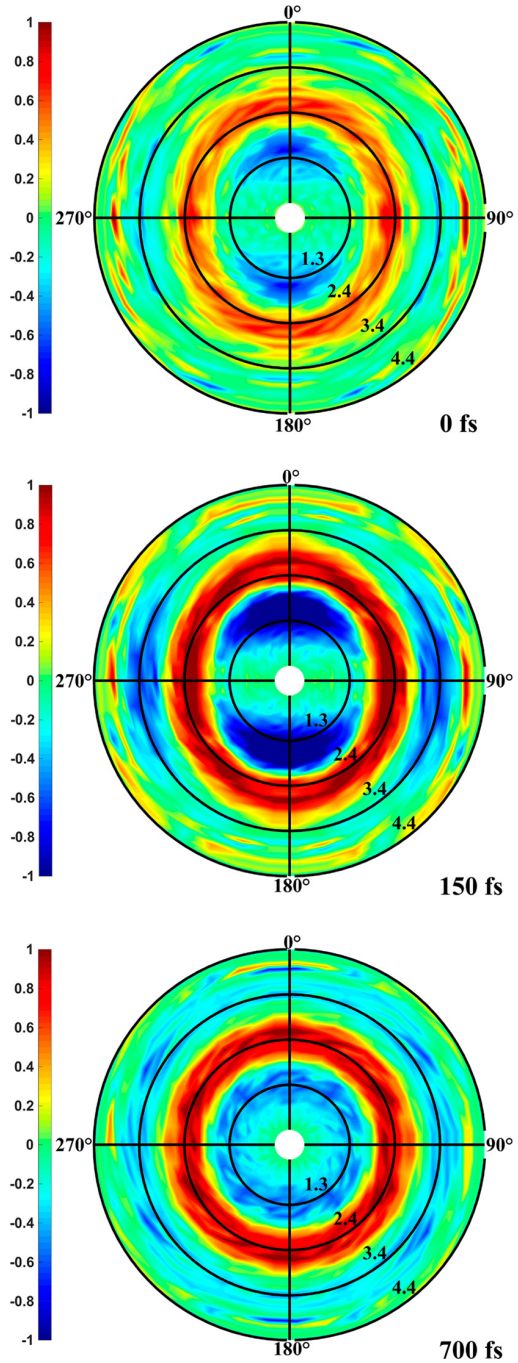

Figure 2. Experimental percent difference scattering patterns at three pump−probe delay times (0, 150, and 700 fs). The vertical axis is defined by the orientation of the polarization axis of the pump laser. The circles in the panels indicate values of the amplitude of the scattering momentum transfer vector of $\mathbf{q}$ = 1.3, 2.4, 3.4, and 4.4 Å^{-1}.

initially accessed state and the laser polarization vector, the ultrashort lifetime of the initially excited states, or any subsequent internal dynamics, will not destroy the $\cos^2(\theta)$ distribution imparted on the ensemble with the excitation. For symmetric and asymmetric tops and linear molecules, different orientations of the TDM vectors in the molecular frame produce markedly different scattering signals regardless of their relative magnitude. Because their orientation is often constrained by the point group of the molecule, straightforward scattering pattern symmetry arguments, possibly assisted by structures derived from inexpensive calculations, can be used to unambiguously determine the initially excited state.

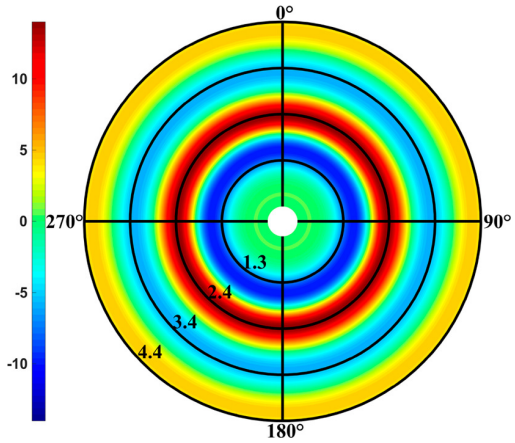

Figure 3. Simulated percent difference scattering pattern produced using the rotationally averaged independent atom model (IAM)[39] showing the isotropic result once the alignment disappears (100% excitation is assumed). The excited-state molecular geometry used corresponds to the optimized geometry of the molecular ion, which is also used in modeling the I_{on} signal in Figure 4.

It is worth pointing out that ultrafast X-ray scattering experiments ultimately measure geometry changes. Although the maximum molecular alignment occurs at time zero, the maximum strength of the anisotropy is observed only when the geometry has evolved significantly. In other words, even though the excited molecules are preferentially aligned with the laser polarization axis, without a significant geometry change, the populations of the ground and the excited states are indistinguishable by X-ray scattering. It is worth noting that detection of the instantaneous rearrangement of the electrons after photon absorption, which is a much weaker effect, remains elusive. As the geometry evolves, the rotational wavepackets formed on the excited and the ground states disperse, resulting in loss of alignment. These two effects, i.e., rotational and internal motion, compete, which results in the anisotropic scattering having maximum magnitude at 150 fs in the case of NMM. In general, because rotational motion is much slower than the molecular frame structural dynamics, the anisotropy should be detectable in a majority of molecular systems. In NMM, as is evident from the data, rotational dephasing fully destroys the $\cos^2(\theta)$ alignment in approximately 700 fs, while near-equilibrium geometry for the Rydberg state is reached in less than 250 fs. Subsequent vibrational motion and subtle geometry transformations shift the peak positions in the $\mathbf{q}$-dependent signal without affecting significantly the overall shape and orientation of the observed anisotropy. This makes the anisotropy near time zero a simple but powerful tool for determining the initially excited state prior to any detailed analysis of the underlying dynamics.

The quadrant symmetry of the observed signal is explained by the orientational freedom around the polarization axis. Close inspection of the anisotropy in the images in Figure 2 reveals that the angular dependence peaks near $\mathbf{q}$ = 1.3 and 3.4 Å^{-1}. The amplitude of the negative peak at $\mathbf{q}$ = 1.3 Å^{-1} is at a maximum in the vertical direction, while the negative signal near $\mathbf{q}$ = 3.4 Å^{-1} is stronger in the horizontal direction. The

DOI: 10.1021/acs.jpclett.8b02773
J. Phys. Chem. Lett. 2018, 9, 6556−6562

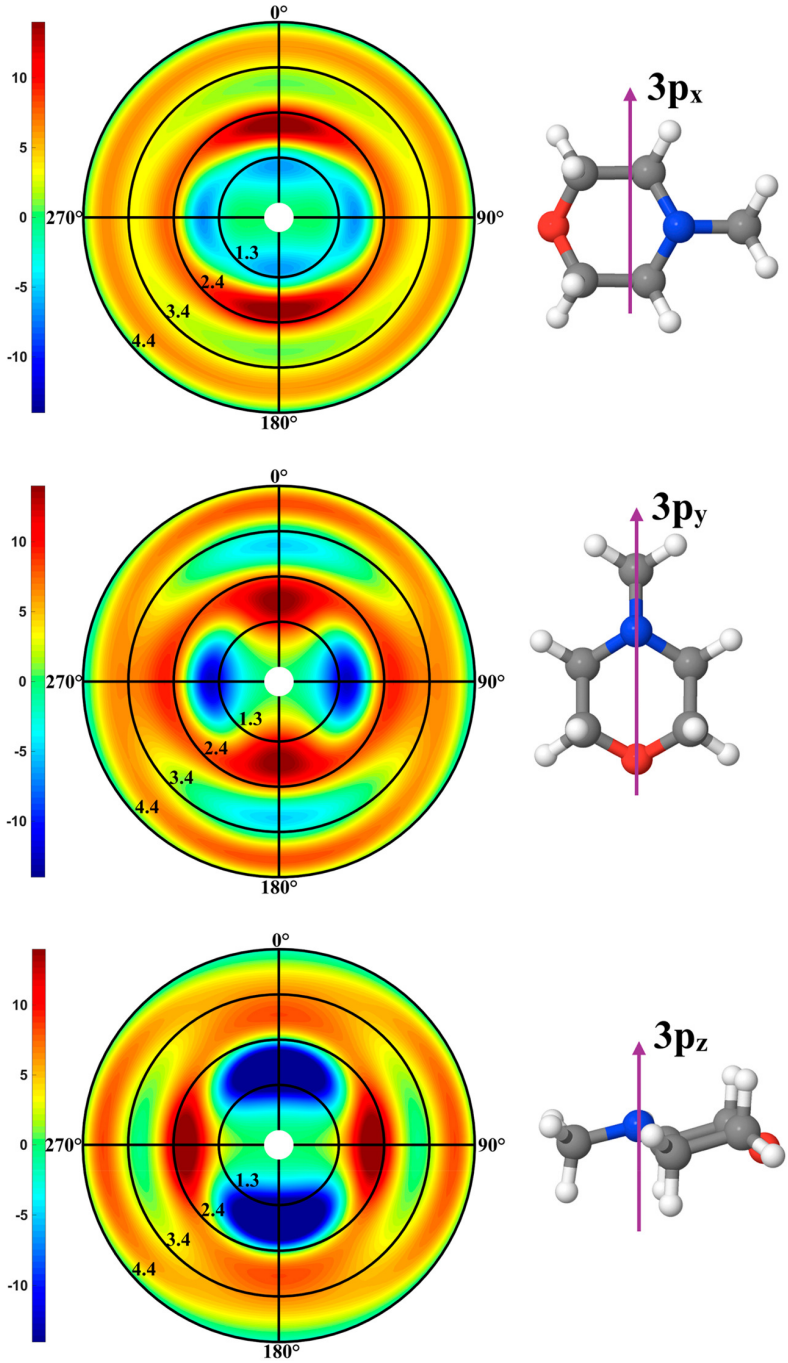

Figure 4. Simulated percent difference scattering patterns for NMM molecules (left column), excited to the $3p_x$, $3p_y$, and $3p_z$ electronic Rydberg states, with the orientation of the TDM relative the molecule shown in the right column. A $\cos^2(\theta)$ distribution with respect to the laser polarization axis is assumed for the excited state, and orientations due to rotation about the laser polarization axis are averaged out. In the right column, the orientation of the TDM in the molecular frame is indicated using a purple arrow, as calculated from MRCI(2,5)/6-311+G(d).

positive feature at $\mathbf{q} = 2.4$ Å^{-1} does not show a strong anisotropy, besides a slight stretch along the vertical axis.

For the purpose of calculating reference scattering intensities, the optimized geometry of the ion-state NMM from UMP2/aug-cc-pVDZ is used to approximate the Rydberg state structure. While not strictly accurate, the resulting error in the isotropic signal has only a small effect on the anisotropic component of the signal. The isotropic difference signal is calculated as shown in Figure 3, which agrees favorably with the experimental pattern following rotational dephasing (at approximately $t > 700$ fs). In order to identify the initially excited state, we create a $\cos^2(\theta)$ distribution of excited molecules in an ensemble for the three possible cases of alignment, corresponding to the polarization axis being aligned with the TDM axis of the $3p_x$, $3p_y$, or $3p_z$ state. The calculated percent difference scattering patterns are presented in Figure 4. It is apparent that the simulated pattern of only the $3p_z$ excitation shows the same symmetry as the experiment (see

DOI: 10.1021/acs.jpclett.8b02773
J. Phys. Chem. Lett. 2018, 9, 6556−6562

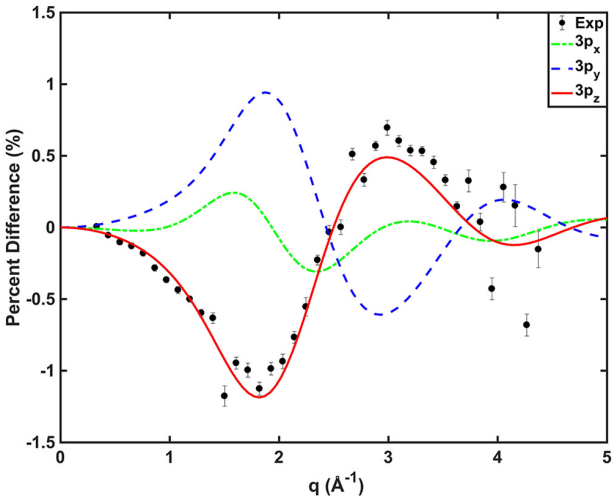

Figure 5. Anisotropic signal derived from experimental results at a pump−probe delay time of t = 150 fs. The three theoretical signals are derived from the calculated results shown in Figure 4. The theoretical curves are scaled with respect to the excitation fraction, and dephasing of the $\cos^2(\theta)$ distribution after time zero is taken into consideration.

Figure 2, 0 and 150 fs panel). However, because the assumption of an instantaneous geometry change is made in the simulations of the results in Figure 4 and because the percent difference signals can be detected only when there is a difference in structures between the unexcited and excited molecules, the angular distribution seen in the anisotropic scattering pattern can never be measured exactly as shown in Figure 4 (note the discrepancy in the angular distributions near $\mathbf{q}$ = 2.4 Å^{-1} for 3p$_z$ as compared to Figure 2). The experimental measurement, Figure 2, shows the pattern on the path from the anisotropic signal approximated as a $\cos^2(\theta)$ distribution to the isotropic signal when the alignment is completely lost to rotational motion.

In order to quantify the difference between the three states of interest, the amplitudes of their anisotropic scattering components, which reflect the angular distributions of the total signal, are decomposed from the two-dimensional scattering pattern using a standard method (see details in the SI),[24,26−28] and compared to the anisotropic component of experimental results at 150 fs, which show maximum anisotropy. (The results using other times are shown in the SI.) As is evident from Figure 5, the anisotropic signal derived from the experimental scattering pattern matches only that of the 3p$_z$ Rydberg state, for which the TDM points along the lone pair of the nitrogen atom. The three calculated signals are remarkably different on account of the orthogonality of their TDMs, which makes identification of the state straightforward. Specifically, the 3p$_z$ and 3p$_y$ anisotropy components are nearly opposite of each other, while the 3p$_x$ anisotropy components have different peak centers and much smaller magnitudes compared to 3p$_y$.

It is possible to imagine situations where a wavepacket is launched on several electronic states, in which case the anisotropy will have contributions from all states involved. Under these circumstances, depending on the relative orientations of their TDMs, it might be possible to apply a fitting procedure to determine even the relative excitation fractions of these states. In the case of NMM, this is not necessary as the experimental results are clearly explained by the 3p$_z$ state alone. This is to be expected given the bandwidth of the pump laser, which is around 1 nm (full width at half-maximum), the large energy differences of the 3p states,[35] and the difference in the oscillator strengths from the benchmark MRCI(2,5)/6-311+G(d) calculation in Table 1.

The current experiment also yields time-dependent scattering signals of the coherent vibrational motion in NMM on the 3s potential energy surface following 3p$_z$ → 3s internal conversion. The full analysis of this motion requires in-depth calculations of the electron density distributions and quantum molecular dynamics that account for vibrational dephasing of the coherent vibrations and nonadiabatic coupling between electronic and nuclear motions. Such an analysis of the presented data is currently underway with the aim of a complete understanding of the photoexcited dynamics and will be reported later.

In contrast to other pump−probe techniques, where the determination of the initially excited state is limited by the availability of complementary spectra or the accuracy of the computed oscillator strengths, ultrafast X-ray scattering experiments provide inherent information for the electronic transition induced by the pump pulse. In this Letter, we demonstrate how the strong anisotropy detected immediately after photoexcitation leads to fast and reliable identification of the initially excited state relying only on the orientation of the TDM in the molecular frame. Because the alignment of the molecules in the ensemble is preserved for a long time compared to the lifetime of the excited state, this method is applicable despite the fast internal conversion after excitation. Ultimately, the advantage of X-ray scattering stems from the fact that, unlike spectroscopy, which deals with the energy levels, the scattering signal constitutes a direct observation of the molecular structure in space.

■ ASSOCIATED CONTENT

Supporting Information

The Supporting Information is available free of charge on the ACS Publications website at DOI: 10.1021/acs.jpclett.8b02773.

Experimental methods, computational details, anisotropy scattering separation, and fitting (PDF)

■ AUTHOR INFORMATION

Corresponding Authors

*E-mail: peter_weber@brown.edu (P.M.W.).
*E-mail: adam.kirrander@ed.ac.uk (A.K.).

ORCID

Haiwang Yong: 0000-0002-5860-4259
Max D. J. Waters: 0000-0002-3505-627X
Theis I. Sølling: 0000-0003-1710-9072
Adam Kirrander: 0000-0002-3347-8137
Peter M. Weber: 0000-0003-3017-336X

Present Address

#T.I.S.: Center for Integrative Petroleum Research, College of Petroleum & Geosciences, King Fahd University of Petroleum & Minerals, Dhahran 31261, Saudi Arabia.

Author Contributions

H.Y. and N.Z. contributed equally to this work.

Notes

The authors declare no competing financial interest.

DOI: 10.1021/acs.jpclett.8b02773
J. Phys. Chem. Lett. 2018, 9, 6556−6562

■ ACKNOWLEDGMENTS

Portions of this research were carried out on the CXI Instrument at the Linac Coherent Light Source (LCLS), a division of SLAC National Accelerator Laboratory and an Office of Science user facility operated by Stanford University. This work was supported by the U.S. Department of Energy, Office of Science, Basic Energy Sciences, under Award DE-SC0017995, the Carnegie Trust for the Universities of Scotland under research grant CRG050414 (A.K.), a Carnegie PhD Scholarship (N.Z.), the Royal Society of Edinburgh under Sabbatical Fellowship 58507 (A.K.), and an EPSRC PhD Studentship from the University of Edinburgh (D.B.).

■ REFERENCES

(1) Nordén, B. Applications of Linear Dichroism Spectroscopy. *Appl. Spectrosc. Rev.* **1978**, *14*, 157−248.
(2) Grechko, M.; Zanni, M. T. Quantification of Transition Dipole Strengths Using 1D and 2D Spectroscopy for the Identification of Molecular Structures via Exciton Delocalization: Application to α-Helices. *J. Chem. Phys.* **2012**, *137*, 184202.
(3) Zare, R. N.; Herschbach, D. R. Doppler Line Shape of Atomic Fluorescence Excited by Molecular Photodissociation. *Proc. IEEE* **1963**, *51*, 173−182.
(4) Mu, T.; Chen, S.; Zhang, Y.; Guo, P.; Chen, H. Determining the Orientation of Transition Moments and Depolarization by Fluorescence Polarizing Angle Spectrum. *Opt. Express* **2015**, *23*, 11748−11754.
(5) Lohmüller, T.; Erdmann, M.; Rubner, O.; Engel, V. Determination of Transition Dipole Moments from Time-Resolved Photoelectron Spectroscopy. *Eur. Phys. J. D* **2003**, *25*, 95−99.
(6) Reid, K. L. Photoelectron Angular Distributions. *Annu. Rev. Phys. Chem.* **2003**, *54*, 397−424.
(7) Dzvonik, M.; Yang, S.; Bersohn, R. Photodissociation of Molecular Beams of Aryl Halides. *J. Chem. Phys.* **1974**, *61*, 4408−4421.
(8) Kawasaki, M.; Lee, S. J.; Bersohn, R. Photodissociation of Molecular Beams of Aryl Halides: Translational Energy Distribution of the Fragments. *J. Chem. Phys.* **1977**, *66*, 2647−2655.
(9) Heck, A. J. R.; Chandler, D. W. Imaging Techniques for the Study of Chemical Reaction Dynamics. *Annu. Rev. Phys. Chem.* **1995**, *46*, 335−372.
(10) Fuglesang, C. D.; Baugh, D. A.; Pipes, L. C. Extraction of the Transition Dipole Matrix from the Photodissociation of Oriented/Aligned Parent Molecules. *J. Chem. Phys.* **1996**, *105*, 9796−9803.
(11) Sato, H. Photodissociation of Simple Molecules in the Gas Phase. *Chem. Rev.* **2001**, *101*, 2687−2726.
(12) Rakitzis, T. P.; van den Brom, A. J.; Janssen, M. H. M. Directional Dynamics in the Photodissociation of Oriented Molecules. *Science* **2004**, *303*, 1852−1854.
(13) Dreuw, A.; Head-Gordon, M. Failure of Time-Dependent Density Functional Theory for Long-Range Charge-Transfer Excited States: The Zincbacteriochlorin-Bacteriochlorin and Bacteriochlorophyll-Spheroidene Complexes. *J. Am. Chem. Soc.* **2004**, *126*, 4007−4016.
(14) Prlj, A.; Curchod, B. F. E.; Fabrizio, A.; Floryan, L.; Corminboeuf, C. Qualitatively Incorrect Features in the TDDFT Spectrum of Thiophene-Based Compounds. *J. Phys. Chem. Lett.* **2015**, *6*, 13−21.
(15) Gudmundsdóttir, H.; Zhang, Y.; Weber, P. M.; Jónsson, H. Self-Interaction Corrected Density Functional Calculations of Molecular Rydberg States. *J. Chem. Phys.* **2013**, *139*, 194102.
(16) Cheng, X.; Zhang, Y.; Jónsson, E.; Jónsson, H.; Weber, P. M. Charge Localization in a Diamine Cation Provides a Test of Energy Functionals and Self-Interaction Correction. *Nat. Commun.* **2016**, *7*, 11013.
(17) Emma, P.; Akre, R.; Arthur, J.; Bionta, R.; Bostedt, C.; Bozek, J.; Brachmann, A.; Bucksbaum, P.; Coffee, R.; Decker, F. J.; et al. First Lasing and Operation of an Ångstrom-Wavelength Free-Electron Laser. *Nat. Photonics* **2010**, *4*, 641−647.
(18) Minitti, M. P.; Budarz, J. M.; Kirrander, A.; Robinson, J.; Lane, T. J.; Ratner, D.; Saita, K.; Northey, T.; Stankus, B.; Cofer-Shabica, V.; et al. Toward Structural Femtosecond Chemical Dynamics: Imaging Chemistry in Space and Time. *Faraday Discuss.* **2014**, *171*, 81−91.
(19) Minitti, M. P.; Budarz, J. M.; Kirrander, A.; Robinson, J. S.; Ratner, D.; Lane, T. J.; Zhu, D.; Glownia, J. M.; Kozina, M.; Lemke, H. T.; et al. Imaging Molecular Motion: Femtosecond X-Ray Scattering of an Electrocyclic Chemical Reaction. *Phys. Rev. Lett.* **2015**, *114*, 255501.
(20) Glownia, J. M.; Natan, A.; Cryan, J. P.; Hartsock, R.; Kozina, M.; Minitti, M. P.; Nelson, S.; Robinson, J.; Sato, T.; van Driel, T.; et al. Self-Referenced Coherent Diffraction X-Ray Movie of Ångström- and Femtosecond-Scale Atomic Motion. *Phys. Rev. Lett.* **2016**, *117*, 153003.
(21) Küpper, J.; Stern, S.; Holmegaard, L.; Filsinger, F.; Rouzée, A.; Rudenko, A.; Johnsson, P.; Martin, A. V.; Adolph, M.; Aquila, A.; et al. X-Ray Diffraction from Isolated and Strongly Aligned Gas-Phase Molecules with a Free-Electron Laser. *Phys. Rev. Lett.* **2014**, *112*, 083002.
(22) Williamson, J. C.; Zewail, A. H. Ultrafast Electron Diffraction. 4. Molecular Structures and Coherent Dynamics. *J. Phys. Chem.* **1994**, *98*, 2766−2781.
(23) Ben-Nun, M.; Cao, J.; Wilson, K. R. Ultrafast X-Ray and Electron Diffraction: Theoretical Considerations. *J. Phys. Chem. A* **1997**, *101*, 8743−8761.
(24) Cao, J.; Wilson, K. R. Ultrafast X-Ray Diffraction Theory. *J. Phys. Chem. A* **1998**, *102*, 9523−9530.
(25) Baskin, J. S.; Zewail, A. H. Molecular Structure and Orientation: Concepts from Femtosecond Dynamics. *J. Phys. Chem. A* **2001**, *105*, 3680−3692.
(26) Baskin, J. S.; Zewail, A. H. Ultrafast Electron Diffraction: Oriented Molecular Structures in Space and Time. *ChemPhysChem* **2005**, *6*, 2261−2276.
(27) Baskin, J. S.; Zewail, A. H. Oriented Ensembles in Ultrafast Electron Diffraction. *ChemPhysChem* **2006**, *7*, 1562−1574.
(28) Lorenz, U.; Møller, K. B.; Henriksen, N. E. On the Interpretation of Time-Resolved Anisotropic Diffraction Patterns. *New J. Phys.* **2010**, *12*, 113022.
(29) Reckenthaeler, P.; Centurion, M.; Fuß, W.; Trushin, S. A.; Krausz, F.; Fill, E. E. Time-Resolved Electron Diffraction from Selectively Aligned Molecules. *Phys. Rev. Lett.* **2009**, *102*, 213001.
(30) Yang, J.; Makhija, V.; Kumarappan, V.; Centurion, M. Reconstruction of Three-Dimensional Molecular Structure from Diffraction of Laser-Aligned Molecules. *Struct. Dyn.* **2014**, *1*, 044101.
(31) Yang, J.; Centurion, M. Gas-Phase Electron Diffraction from Laser-Aligned Molecules. *Struct. Chem.* **2015**, *26*, 1513−1520.
(32) Yang, J.; Beck, J.; Uiterwaal, C. J.; Centurion, M. Imaging of Alignment and Structural Changes of Carbon Disulfide Molecules Using Ultrafast Electron Diffraction. *Nat. Commun.* **2015**, *6*, 8172.
(33) Yang, J.; Guehr, M.; Vecchione, T.; Robinson, M. S.; Li, R.; Hartmann, N.; Shen, X.; Coffee, R.; Corbett, J.; Fry, A.; et al. Diffractive Imaging of a Rotational Wavepacket in Nitrogen Molecules with Femtosecond Megaelectronvolt Electron Pulses. *Nat. Commun.* **2016**, *7*, 11232.
(34) Zhang, Y.; Deb, S.; Jónsson, H.; Weber, P. M. Observation of Structural Wavepacket Motion: The Umbrella Mode in Rydberg-Excited N-Methyl Morpholine. *J. Phys. Chem. Lett.* **2017**, *8*, 3740−3744.
(35) Zhang, Y.; Jónsson, H.; Weber, P. M. Coherence in Nonradiative Transitions: Internal Conversion in Rydberg-Excited N-Methyl and N-Ethyl Morpholine. *Phys. Chem. Chem. Phys.* **2017**, *19*, 26403−26411.
(36) Blaj, G.; Caragiulo, P.; Carini, G.; Carron, S.; Dragone, A.; Freytag, D.; Haller, G.; Hart, P.; Hasi, J.; Herbst, R.; et al. X-Ray Detectors at the Linac Coherent Light Source. *J. Synchrotron Radiat.* **2015**, *22*, 577−583.

DOI: 10.1021/acs.jpclett.8b02773
J. Phys. Chem. Lett. 2018, 9, 6556−6562

(37) Als-Nielsen, J.; McMorrow, D. *Elements of Modern X-Ray Physics*, 2nd ed.; Wiley, 2011.
(38) Zare, R. N. Optical Preparation of Aligned Reagents. *Ber. Bunsenges. Phys. Chem.* **1982**, *86*, 422−425.
(39) Prince, E. *International Tables for Crystallography. Vol. C: Mathematical, Physical and Chemical Tables*, 3rd ed.; Springer: Dordrecht, The Netherlands, 2006.

DOI: 10.1021/acs.jpclett.8b02773
J. Phys. Chem. Lett. 2018, 9, 6556−6562

Supporting information:

Determining Orientations of Optical Transition Dipole Moments using Ultrafast X-Ray Scattering

Haiwang Yong,[1] Nikola Zotev,[2] Brian Stankus,[1] Jennifer M. Ruddock,[1] Darren Bellshaw,[2] Sébastien Boutet,[3] Thomas J. Lane,[3] Mengning Liang,[3] Sergio Carbajo,[3] Joseph S. Robinson,[3] Wenpeng Du,[1] Nathan Goff,[1] Yu Chang[1], Jason E. Koglin,[3] Max D.J. Waters,[4] Theis I. Sølling,[4,$] Michael P. Minitti,[3] Adam Kirrander,[2,*] and Peter M. Weber[1,*]

[1]*Brown University, Department of Chemistry, Providence, Rhode Island 02912, USA*
[2]*School of Chemistry, University of Edinburgh, Edinburgh EH9 3FJ, United Kingdom*
[3]*SLAC National Accelerator Laboratory, Menlo Park, California 94025, USA*
[4]*Department of Chemistry, University of Copenhagen, Universitetsparken 5, 2100 Copenhagen, Denmark.*

[$]*Present address: Center for Integrative Petroleum Research, College of Petroleum & Geosciences, King Fahd University of Petroleum & Minerals, Dhahran 31261, Saudi Arabia*

Corresponding Author

*E-mail: peter_weber@brown.edu (P. M. W.); adam.kirrander@ed.ac.uk (A. K.)

1. Experimental setup and computational details

The scattering measurements were performed in the CXI endstation of the Linac Coherent Light Source (LCLS). Details of the time-resolved X-ray scattering experiment and the scattering data processing have been described previously.[1,2] The optical pump pulse was generated from the fourth harmonic of a 120 Hz Ti:Sa laser operating at 800 nm, producing pulses at 200 nm. The X-ray probe pulse was generated from LCLS, operating at 9.49 keV with around 10 fs pulse duration. The N-methylmorpholine was discharged into a scattering cell with a sample pressure of 7 Torr. The pump and probe pulses were focused collinearly into the scattering cell, each with an approximate spot size of 30 μm FWHM. The scattered X-rays were measured with a 2.3-megapixel Cornell-SLAC Pixel Array Detector (CSPAD)[3]. By analyzing the scattering signal around time zero, we determined the sigma cross-correlation time to be 101(12) fs. The time delay between the pump and probe pulses was controlled by a motorized delay stage, and the timing jitter from LCLS was monitored by a spectrally encoded cross correlator, achieving the time resolution of 10 fs.[4,5] Aiming to have best signal to noise ratio, we sort the signal into 50 fs time bins. In order to calibrate the shot-to-shot X-ray intensity transmitted through the scattering cell entrance apertures, the intensity of the primary X-ray beam was monitored downstream of the CSPAD by a photodiode.

The ionic ground state NMM, the geometry of which was optimized using the UMP2/aug-cc-pVDZ method, was used to represent the excited state structure. The oscillator strengths of NMM molecules are calculated at the neutral ground state NMM structure, and the corresponding levels of theory are listed in the Table 1 in main text. We find that all three methods predict the transition from the ground to the $3p_x$ state with a near zero oscillator strength, indicating that it is a forbidden transition. However, when considering the symmetry allowed

transitions, the results of $3p_y$ and $3p_z$ TDMs calculated by CAM-B3LYP/6-311++G(d,p) are quite different from the results with CAS(2,5)/6-311+G(d) and MRCI(2,5)/6-311+G(d). We assume that the reliance on Kohn-Sham orbitals and a poorly treated self-interaction error for the Rydberg state orbitals could be the reason for CAM-B3LYP/6-311++G(d,p) predicting the $3p_y$ and $3p_z$ TDM qualitatively incorrectly. The *ab-initio* CAS and MRCI calculations are performed using the Molpro electronic structure software package[6,7]. The CAM-B3LYP calculation is performed using the Gaussian 09 software[8].

In the anisotropic scattering pattern simulations, a combination of excited state molecules with a $\cos^2(\theta)$ distribution and ground state molecules with a $\sin^2(\theta)$ distribution together are used to represent the ensemble right after optical excitation. Here, θ is defined as the angle between the molecular TDM vector and the laser polarization vector ranging from 0 to π. The molecules preserve the rotational symmetry about the laser polarization axis in the ensemble. Next, the independent atom model (IAM)[9] is used to simulate the 2-dimensonal scattering pattern $I(\phi,q)$ for each fixed orientation single molecule from the ensemble (see Equation S1)[9], and then summed and averaged together to give the $I_{on}(\phi,q)$ signal. The $I_{off}(\phi,q)$ signal is calculated from rotational averaged ground state molecules by IAM. Three possible molecular TDM vectors were considered for Rydberg-excited NMM, the percent difference signals $P_{diff}(\phi,q,t)$ derived from $I_{on}(\phi,q)$ and $I_{off}(\phi,q)$ using main text Eq. 1 were shown in Figure 4.

$$I(\phi,q) = \sum_{n=1}^{N}\sum_{m=1}^{N} f_n f_m e^{iq\cdot\left(\overrightarrow{r_m}-\overrightarrow{r_n}\right)} \quad \text{(S1)}$$

In Equation S1, the f_n and $f_m$are atomic form factors of the n_{th} and m_{th} atoms in the molecule taken from the reference[9], N is the total number of atoms in the molecule, $\overrightarrow{r_m}$ and $\overrightarrow{r_n}$ are the positions of the n_{th} and m_{th} atoms in molecular frame, and q is the momentum transfer vector

which can be described by the vector (ϕ,q,ϑ) in the laboratory frame with the constraint $q = \frac{4\pi\sin\frac{\vartheta}{2}}{\lambda}$. Here, the ϑ is the scattering angle, as the angle between the direction of incident photon and scattered photon. λ is the wavelength of the X-ray.

2. Anisotropic scattering decomposition

A standard method to separate the angular dependence signal $P_{diff,aniso}(q,t)$ from total scattering patterns $P_{diff}(\phi,q,t)$ was used for both experimental patterns and theoretical patterns simulated using procedures described above. The decomposition equation is given by[10]

$$P_{diff}(\phi,q,t) = \frac{1}{2}\left(3\left(\cos(\phi)\sqrt{1-\left(\frac{\lambda q}{4\pi}\right)^2}\right)^2 - 1\right)P_{diff,aniso}(q,t) + P_{diff,iso}(q,t) \qquad \text{(S2)}$$

Due to the quadrant symmetry of the $\cos^2(\theta)$ distribution in the ensemble for a single-photon excitation process, this angular symmetry can be described by second order Legendre polynomials. In this case, the total scattering pattern can be decomposed to an isotropic component that reflects the structural dynamics and an anisotropic component that reflects both rotational and structural dynamics of the excited molecules[10]. The decomposed theoretical signals $P_{diff,aniso}(q,t)$ derived from the calculated results $P_{diff}(\phi,q,t)$ were scaled by a parameter η to account for the effect from an instrument function, an excitation fraction and the dephasing of the $\cos^2(\theta)$ distribution after time zero due to rotational motion of molecules. Except the results shown in Figure 5 in main text, the decomposed experimental and corresponding theoretical results at two other time delays, 0 fs and 250 fs, are shown here in Figure S1 and Figure S2, respectively. The reason we choose 150 fs for the illustration of the main text is mainly that time point shows a maximum anisotropy, meaning that the molecules have not rotated much within 150 fs. Because of the large differences between the scattering

patterns of the three possible cases, the assignment of the $3p_z$ as the initially excited state is independent of the time delay used for the fit, as shown in Figure S1 and S2.

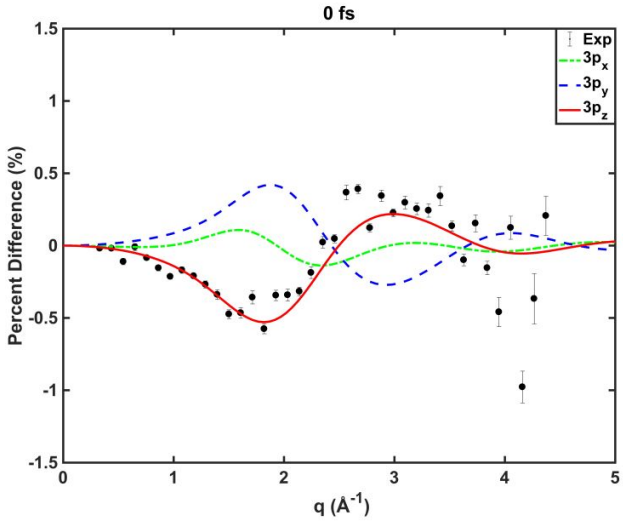

Figure S1. Anisotropy signal from the experimental results at pump-probe delay time t=0 fs.

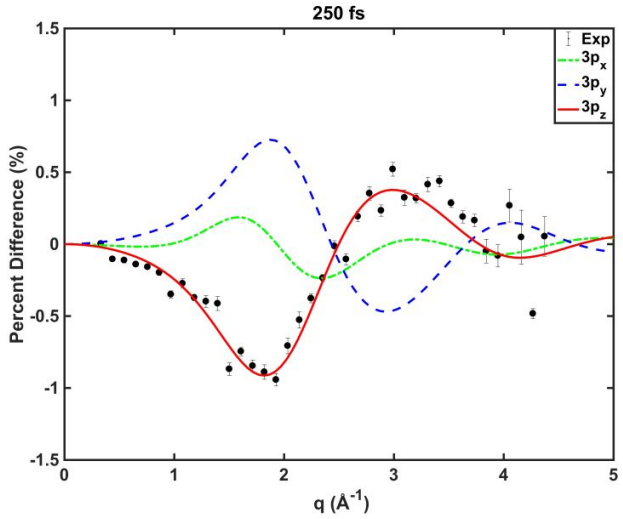

Figure S2. Anisotropy signal from the experimental result at pump-probe delay time t=250 fs.

References:

(1) Budarz, J. M.; Minitti, M. P.; Cofer-Shabica, D. V; Stankus, B.; Kirrander, A.; Hastings, J. B.; Weber, P. M. Observation of Femtosecond Molecular Dynamics via Pump-Probe Gas Phase X-Ray Scattering. *J. Phys. B: At. Mol. Opt. Phys.* **2016**, *49*, 034001.

(2) Minitti, M. P.; Budarz, J. M.; Kirrander, A.; Robinson, J. S.; Ratner, D.; Lane, T. J.; Zhu, D.; Glownia, J. M.; Kozina, M.; Lemke, H. T.; et al. Imaging Molecular Motion: Femtosecond X-Ray Scattering of an Electrocyclic Chemical Reaction. *Phys. Rev. Lett.* **2015**, *114*, 255501.

(3) Blaj, G.; Caragiulo, P.; Carini, G.; Carron, S.; Dragone, A.; Freytag, D.; Haller, G.; Hart, P.; Hasi, J.; Herbst, R.; et al. X-Ray Detectors at the Linac Coherent Light Source. *J. Synchrotron Rad.* **2015**, *22*, 577–583.

(4) Harmand, M.; Coffee, R.; Bionta, M. R.; Chollet, M.; French, D.; Zhu, D.; Fritz, D. M.; Lemke, H. T.; Medvedev, N.; Ziaja, B.; et al. Achieving Few-Femtosecond Time-Sorting at Hard X-Ray Free-Electron Lasers. *Nat. Photonics* **2013**, *7*, 215–218.

(5) Bionta, M. R.; Lemke, H. T.; Cryan, J. P.; Glownia, J. M.; Bostedt, C.; Cammarata, M.; Castagna, J.-C.; Ding, Y.; Fritz, D. M.; Fry, A. R.; et al. Spectral Encoding of X-Ray/Optical Relative Delay. *Opt. Express* **2011**, *19* (22), 21855-21865.

(6) Werner, H.-J.; Knowles, P. J.; Knizia, G.; Manby, F. R.; Schütz, M.; Celani, P.; Korona, T.; Lindh, R.; Mitrushenkov, A.; Rauhut, G.; et al. MOLPRO, Version 2012.1, a Package of Ab Initio Programs. see http://www.molpro.net.

(7) Werner, H. J.; Knowles, P. J.; Knizia, G.; Manby, F. R.; Schütz, M. Molpro: A General-Purpose Quantum Chemistry Program Package. *WIREs Comput. Mol. Sci.* **2012**, *2*, 242–

253.

(8) Frisch, M. J.; Trucks, G. W.; Schlegel, H. B.; Scuseria, G. E.; Robb, M. A.; Cheeseman, J. R.; Scalmani, G.; Barone, V.; Mennucci, B.; Petersson, G. A.; et al. Gaussian 09, Revision C.01, Gaussian, Inc., Wallingford CT, **2009**.

(9) Prince, E. *International Tables for Crystallography. Volume C: Mathematical, Physical and Chemical Tables*, 3rd ed.; Springer, Dordrecht, **2006**.

(10) Lorenz, U.; Møller, K. B.; Henriksen, N. E. On the Interpretation of Time-Resolved Anisotropic Diffraction Patterns. *New J. Phys.* **2010**, *12*, 113022.

5.3 Conclusion

Retrieving the direction of the TDM in NMM has been shown to enable the characterisation of the initially excited state in the experiment. Following this pioneering work, the method has been applied to another experiment [80]. In that particular case, it was even possible to use a fitting procedure to determine the relative ratio of the Rydberg states involved. However, the technique has to be utilised with caution. In the situations under consideration, it was applied based on the knowledge that the excitation is restricted to one of the members of a small group of Rydberg states, whose TDMs are markedly different. In principle, it is not possible to differentiate between states that have the same or similar direction of the TDM. This situation arises often as TDMs are constrained by the symmetry properties of the molecule, so a number of electronic states can share these possible directions. Furthermore, it might not be possible to decisively attribute the observed anisotropy to any state if there is a complete lack of knowledge of the character of the states that could potentially be accessed. This stems from the fact that at least a crude estimate for the geometry in the excited states is required. Finally, knowledge of the direction of the TDM by itself does not constitute knowledge of the state's character. Computational tools or previous experimental findings are needed to elucidate this matter.

The following chapter comes as a natural continuation of this work. It looks at the internal dynamics that follows from the excitation to the $3p_z$ Rydberg state. Knowledge of the initially accessed states has important consequences for assigning the correct reaction paths and explaining the ultrafast vibrations retrieved from the scattering data.

Chapter 6

Observing Coherent Vibrations

6.1 Introduction

This chapter presents work which is reproduced with permission from Brian Stankus, Haiwang Yong, **Nikola Zotev**, Jennifer Ruddock, Darren Bellshaw, Thomas J. Lane, Mengning Liang, Sébastien Boutet, Sergio Carbajo, Joseph S. Robinson, Wenpeng Du, Nathan Goff, Yu Chang, Jason E. Koglin, Michael P. Minitti, Adam Kirrander and Peter M. Weber. "Ultrafast X-Ray Scattering Reveals Vibrational Coherence Following Rydberg Excitation", *Nature Chemistry*, **11**, 716 (2019).

In Section 3.6, the limitations of direct inversion schemes have been discussed. The limited range of the momentum transfer vector fundamentally prevents the retrieval of high-resolution radial distribution functions directly from the scattering pattern. Furthermore, even if that is possible, relying solely on the isotropic scattering provides only a limited representation of the molecular structure. Vital information is lost in the angular average. The same geometry is encoded in the anisotropic component but projected onto the second order spherical Bessel function. Thus, combining isotropic and anisotropic scattering amplitudes would improve the information content, but that would still not be sufficient to confidently assign the 3D structure of the molecule. Theoretical constraints are always needed.

To bypass these problems, the work described here takes a different approach. Following a photoexcitation with a 200 nm pulse, the time-dependent structural information for NMM is extracted by what is essentially a

least-squares fitting procedure, where the possible conformations are selected from a large pool of theoretical structures. The work reports two different pools of structures and compares the results obtained with them in order to give an estimate of the sensitivity of the method to the input from theory. Both pools are derived from surface-hopping simulations, on the Rydberg states' surfaces and on the positive ion surface. The role of these pools is to provide meaningful constraints on possible geometries, which address the issue of the limited information content in the scattering signal.

It may appear at first that the small range of scattering angles collected fundamentally limits the resolution via the uncertainty principle, $\sigma_q \sigma_r \approx \pi$, and effectively makes any attempts to retrieve high-resolution structures hopeless. However, the geometries in the pools are characterised by a certain degree of correlation between the interatomic vectors, which reflects basic physical constraints that exist in the molecule due to its bonding. For example, changing the length of any given chemical bond in a cyclic compound inevitably also alters the bond angles in a somewhat predictable manner. These correlations mean that the features in the scattering signal that evolve with time can only arise from large collective motions. Whilst individual uncertainty in a given parameter, *e.g.* a bond length, might be high when viewed in isolation, there may only exist a restricted range over which it can physically coexist with the other parameters, as encoded in the scattering signal. Similarly, the method reported in this work bypasses the fact that the structural information is projected onto the zeroth order spherical Bessel function and the anisotropy is not used further than assigning the initially excited state. Having that in mind, it is important to differentiate between precision and accuracy when applying the approach described here. While within a given pool of trajectories, the inversion might be statistically quite sound, that does not mean that it is accurate. Higher accuracy would arise only from more accurate constraints on the structure parameters, *i.e.* a higher level of theory is used in the dynamics simulation.

Another important advance made by this work is that it is the first one to take into account explicitly the electronic structure of the molecule. The molecule remains in the Rydberg manifold for the entire duration of the

experiment. For a fixed geometry, Rydberg states have almost identical isotropic scattering patterns. Also, as discussed later, the difference between the *ab initio* Rydberg scattering pattern and IAM is relatively constant with geometry. Thus, the difference is subtracted from the experimental data, which is then analysed solely from the perspective of the IAM. Computing *ab initio* scattering patterns for the entire pool of theoretical structures is computationally prohibitive. Despite those caveats, this works marks a crucial first step towards the simultaneous determination of nuclear and electronic motion.

ARTICLES
https://doi.org/10.1038/s41557-019-0291-0
nature chemistry

Ultrafast X-ray scattering reveals vibrational coherence following Rydberg excitation

Brian Stankus[1,4], Haiwang Yong[1,4], Nikola Zotev[2], Jennifer M. Ruddock[1], Darren Bellshaw[2], Thomas J. Lane[3], Mengning Liang[3], Sébastien Boutet[3], Sergio Carbajo[3], Joseph S. Robinson[3], Wenpeng Du[1], Nathan Goff[1], Yu Chang[1], Jason E. Koglin[3], Michael P. Minitti[3], Adam Kirrander[2] and Peter M. Weber[1*]

The coherence and dephasing of vibrational motions of molecules constitute an integral part of chemical dynamics, influence material properties and underpin schemes to control chemical reactions. Considerable progress has been made in understanding vibrational coherence through spectroscopic measurements, but precise, direct measurement of the structure of a vibrating excited-state polyatomic organic molecule has remained unworkable. Here, we measure the time-evolving molecular structure of optically excited *N*-methylmorpholine through scattering with ultrashort X-ray pulses. The scattering signals are corrected for the differences in electron density in the excited electronic state of the molecule in comparison to the ground state. The experiment maps the evolution of the molecular geometry with femtosecond resolution, showing coherent motion that survives electronic relaxation and seems to persist for longer than previously seen using other methods.

The coherence of molecular vibrations—and its decay by dephasing—determines a wide array of molecular properties and governs the widths and shapes of observed vibrational spectral lines[1,2]. Statistical theories for chemical reactions assume that dephasing leads to the dissipation of vibrational energy throughout the available phase space[3]. Dephasing could thus be considered an obstacle to the coherent control of chemical reaction dynamics using laser pulses[4] and to other fields that rely on the quantum coherence of molecular vibrations.

The advent of ultrashort pulsed optical lasers ushered in a new era of femtochemistry. Femtosecond laser pulses allowed spectroscopic measurements of time-evolving molecules in real time, providing intriguing glimpses of the intricate ways in which molecular excitation can lead to chemical dynamics and vibrational coherences[5,6]. These ultrafast studies, which rely on spectroscopic probes, have generated a wealth of knowledge about photochemical reaction mechanisms. Yet, spectroscopy is an inherently indirect probe of structural dynamics, and so following the dephasing of polyatomic molecules in real time—at the level of individual bond parameters—remains challenging.

With the recent advent of ultrafast X-ray free-electron lasers and ultrafast electron diffraction, more direct measurements of time-dependent atomic positions have become possible[7–15]. Ultrafast gas-phase scattering has emerged as a powerful tool for measuring molecular dynamics[7,8,13,14,16–18], revealing chemical reaction mechanisms that were previously inferred but not observed. In this study, we show that precise excited-state molecular structures can be obtained from X-ray scattering patterns and used to construct a detailed picture of their dynamics with femtosecond time resolution. Recent spectroscopic studies have revealed that in *N*-methylmorpholine (NMM), coherent vibrational motions can survive an electronic relaxation process[19,20]. Here, we show that the low-frequency coherent vibrations of NMM have been clearly resolved in space and time using time-resolved X-ray scattering with ultrafast pulses generated by the Linac Coherent Light Source (LCLS). The determined time-resolved molecular structures show that the coherent motions persist well beyond electronic relaxation. This is an important finding because such electronic relaxation phenomena in large-molecule systems have traditionally been regarded as statistical in nature.

The nature of the initial excited state when NMM is pumped with 200 nm radiation has previously been the subject of investigation. Analysis of the anisotropic X-ray scattering signal of NMM immediately following 200 nm excitation revealed the population of the $3p_z$ molecular Rydberg state[21]. In ultrafast photoelectron spectroscopy studies, excitation to the $3p_z$ state[21] has been seen to launch a coherent structural oscillation that persists following internal conversion to the 3*s* state with a 106 fs time constant[19]. Electronic structure calculations indicate that the molecular structure in the electronic ground state is an equatorial chair structure[20,22] (shown in Fig. 1), and the observed photoelectron signals indicate that the structural motion primarily responsible for the observed oscillation is a coherent vibration in a mode that involves the planarization of the amine, which is consistent with related computational studies on the same molecule[23].

In this work, the transient structures of the molecule as it evolves in time on the Rydberg surface are determined by matching the experimentally measured X-ray scattering patterns against a large set of computed patterns that are from a global geometry search in a conformational space created from molecular dynamics simulations. This analysis, along with a correction to the signals stemming from the change in electron density following excitation, is capable of providing a femtosecond time-resolved determination of electronically excited molecular structures in a polyatomic molecule, even in the absence of heavy elements.

In the experiment, a 200 nm UV pump pulse excited the molecules to the $3p_z$ Rydberg state[19,21] (Fig. 1). The scattering patterns

[1]Department of Chemistry, Brown University, Providence, RI, USA. [2]EaStCHEM, School of Chemistry, University of Edinburgh, Edinburgh, UK. [3]Linac Coherent Light Source, SLAC National Accelerator Laboratory, Menlo Park, CA, USA. [4]These authors contributed equally: Brian Stankus, Haiwang Yong. *e-mail: peter_weber@brown.edu

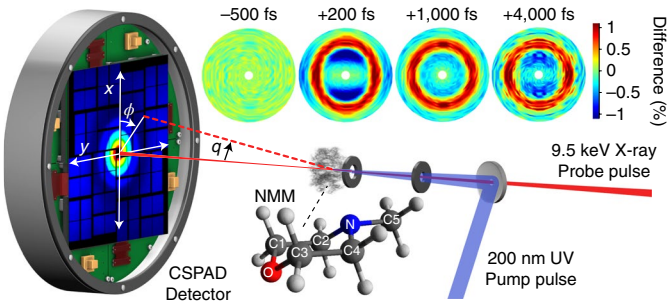

Fig. 1 | A schematic of the experimental set-up. The reaction of NMM is initiated with a 200 nm UV pump pulse, and the time-evolving molecular structure is probed by scattering using 9.5 keV X-ray probe pulses with a variable time delay. The scattering signals are recorded with a CSPAD detector. The percentage change in the scattering pattern as a function of q and Φ for several representative time delays is also shown (top).

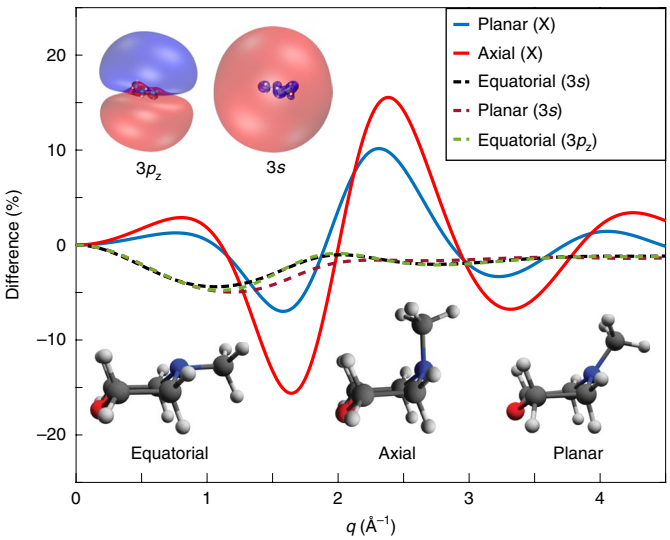

Fig. 2 | The calculated difference in scattering patterns caused by nuclear and electronic structure changes as a function of q. This assumes 100% excitation of the sample. The three relevant molecular conformations, as well as orbital plots for the 3s and 3p_z states, are included as insets. The planar (X) (blue solid line) and axial (X) (red solid line) curves are the difference between the planar and equatorial structures in the ground state, and between the axial and equatorial structures in the ground state, respectively. X, the electronic ground state of the molecule. The equatorial (3s) (black dashed line) and planar (3s) (red dashed line) curves are the difference between the equatorial structure in the 3s and ground states, and between the planar structure in the 3s and ground states, respectively. The equatorial (3p_z) curve (black dashed line) is the difference between the equatorial structure in the 3p_z and ground states.

created by intersecting the sample with a pulsed, 9.5 keV X-ray beam from the LCLS light source were detected by a 2.3 megapixel Cornell–SLAC pixel array detector (CSPAD)[24]. The positions of the detected X-rays were converted to the coordinates of the amplitude of the scattering vector (q) and the azimuthal angle (ϕ) as described in Supplementary Section 1.

Results and discussion

Experimental results. The time-evolving signals are expressed as a percentage change (equation (1)), where $I_{on}(\phi,q,t)$ represents the scattering pattern at the given time delay (t), and $I_{off}(\phi,q)$ represents the scattering pattern of the ground-state unexcited molecules. The resulting time-dependent scattering images (see Fig. 1 for an illustration; a full animation is provided in Supplementary Video 1) show a sudden onset of the difference signal following optical excitation. An anisotropic component of the signal (seen most clearly at $t = 200$ fs) arises from the preferential excitation of those molecules whose transition dipole moments are oriented parallel to the linear polarization of the optical pump pulse in the laboratory frame. Because the anisotropy is determined by the relationship between the transition dipole moment vector in the initially accessed state and the laser polarization vector, a detailed analysis of this component previously derived an unambiguous assignment of the initially excited state to the 3p_z Rydberg state[21]. The isotropic signal, on the other hand, contains all of the intrinsic information of the molecule in the molecular frame, including both the nuclear and electronic structural evolutions. The two components are decomposed from the two-dimensional scattering patterns using a standard method[25,26]:

$$P_{diff}(\phi,q,t) = 100\frac{I_{on}(\phi,q,t) - I_{off}(\phi,q)}{I_{off}(\phi,q)} \quad (1)$$

The isotropic scattering signal—which shows a time dependence that reveals the dynamics of all internal degrees of freedom of the reacting molecule—has two main features: a rapid 'step function' onset, and a subsequent oscillation that reflects vibrational motions in the molecule and occurs on a timescale that is in good agreement with previous photoelectron studies (623 ± 19 fs versus 630 ± 13 fs measured before)[19] (all errors are reported as 1σ). The oscillation is heavily damped with a time constant of 635 ± 116 fs, which also agrees with the 530 ± 66 fs value measured by photoelectron spectroscopy. A third, low-amplitude exponential-decay feature (see Supplementary Fig. 2) probably arises from intramolecular vibrational relaxation on a picosecond timescale. There is a rapid onset of the difference scattering signal, which is attributed to the electronic transition of NMM from the ground state to the Rydberg state, as well as small-amplitude nuclear motions following electronic excitation. Consequently, the effects of electronic excitation need to be considered to extract the structural motions of the vibrating molecule.

Calculation of electronic excitation effects. The effect on the scattering patterns that results from the change in electron density due to the optical excitation is calculated using ab initio multiconfigurational wavefunctions obtained from the state-averaged complete active-space self-consistent field method (SA5-CASSCF(2,5)/6-311++G(d,p)) (refs. [27,28]). Figure 2 shows the effect of electronic excitation on the scattering signals in comparison to conformational change. The relative magnitude of the effect of the redistribution of electron density following excitation is seen to be approximately half of the effect from the nuclear structure change, depending on the specific molecular geometry. At certain vibrational displacements, the two effects can be nearly comparable in magnitude, meaning that the signatures of both are captured in the scattering experiment. For example, for the planar structure represented in Fig. 2, the electronic contribution has a magnitude of −4.7% difference at $q = 1$ Å^{-1}, whereas the structural contribution has a magnitude of only 0.5%. Clearly, the electronic contribution must be included to adequately account for the observed difference signals.

The effect on the scattering signal that arises from the change in the spatial distribution of the Rydberg electron as it internally converts from 3p_z to 3s is not experimentally observed, which is consistent with a very small difference in the calculated effect (Fig. 2). This is because the Rydberg orbitals are very diffuse, and,

Table 1 | The molecular structure parameters of vibrationally hot NMM in the excited 3*s* state, determined for delay times from 2.6 ps to 3.9 ps

	Experimental		Calculated	
	Rydberg-surface dynamics pool	Ion-surface dynamics pool	Ion structure	Ground-state structure
Nearest-neighbour interatomic distances (Å)				
O–C3	1.368 ± 0.005	1.373 ± 0.008	1.401	1.398
O–C1	1.364 ± 0.008	1.374 ± 0.006	1.401	1.398
N–C4	1.434 ± 0.012	1.449 ± 0.007	1.439	1.453
N–C2	1.441 ± 0.019	1.447 ± 0.009	1.439	1.453
N–C5	1.433 ± 0.007	1.430 ± 0.006	1.454	1.446
C3–C4	1.557 ± 0.009	1.554 ± 0.008	1.580	1.519
C2–C1	1.578 ± 0.023	1.552 ± 0.006	1.580	1.519
Characteristic angles (°)				
C2–C1–C4–C3 torsional	0.6 ± 1.5	−0.3 ± 0.5	0.0	0.0
O–N–C5 umbrella	28.3 ± 6.1	20.4 ± 2.7	37.4	−24.1
N–C4–C2–C5 pyramidalization	1.4 ± 1.2	−0.1 ± 1.0	4.0	−17.4
C5–N–C4–C3 torsional	56.8 ± 4.3	44.3 ± 3.1	70.3	1.6

The errors are the s.d. over measurements at different time points.

when rotationally averaged, the difference between them is small. The electronic effect observed in the scattering experiment must therefore primarily arise from the vacancy left in the nitrogen valence orbitals of the tertiary amine group following the promotion of an electron to the Rydberg orbital. This also explains the observation in Fig. 2 that the electronic effect does not greatly depend on the geometrical structure of the molecule. Given that all of the measured structural evolution occurs on the Rydberg manifold[19], the electronic contribution to the signal can be treated as approximately constant throughout the dynamics. As a consequence, it is possible to separate the electronic and nuclear effects on the scattering patterns and to treat their contributions to the signal as approximately additive.

Structural determination analysis. To determine the transient molecular structures and construct the time-dependent video of the dynamical motions, the experimental signal at each time point was compared against a large set of scattering patterns computed from many hypothetical structures. This large pool of possible structures was created by extracting structures from a large and diverse set of surface-hopping trajectories propagated on the ground and excited Rydberg electronic states with the excess kinetic energy from the excitation taken into consideration. Approximately one million molecular geometries were extracted from the simulations. These sample a large conformational space that is confined to energetically allowed conformations that could potentially be accessed by the molecule during the dynamics. For each molecular structure, a scattering pattern was computed by approximating the geometrical structure using the Independent Atom Model[29] and adding the contribution of the electronic excitation of the planar structure in the 3*s* state (Fig. 2). By comparing the experimental signal with theoretical patterns, the least-squares fitting errors of all theoretical patterns from the pool were obtained at each time point. These errors were then plotted against each structural parameter; that is, the interatomic distances and the bond angles. In general, we found that the least-squares error varies as a function of any given structural parameter in a normal or skewed-normal distribution. The peak centres of these distributions are taken to represent the best-fitting structural parameters (see Supplementary Section 2 for details). This analysis gives the transient molecular structure at each time point independently, so that the measurement of many time points yields the time-dependent motions of the excited-state molecule. The analysis results in the probability of the laser exciting the molecules to the upper electronic state. This global, time-independent parameter was determined to be 5.7%, a value that gives confidence that multiphoton excitation processes do not interfere with our analysis.

After the damping of the observed oscillations is complete, the difference scattering signals settle to an essentially constant value. As the internal conversion from the $3p_z$ to the 3*s* state is complete after ~0.5 ps, the scattering signal at long delay times arises from the structure of NMM in the 3*s* Rydberg state. The excited-state structure of NMM—determined from experimental signals at long delay times (2.6–3.9 ps)—is given in Table 1. As the determination of the molecular structure is performed independently for each of the 25 time points, the structural parameters obtained from each of those time points are independent measurements that can be used to assess the precision of the structure determination. The errors reported in Table 1 are the standard deviations over measurements of independent time points. It is seen that the nearest-neighbour bond distances determined from this procedure have errors on the order of ~10 mÅ. To assess the accuracy of the result, Table 1 includes the optimized structure of NMM in its cation ground state. Although the ion structure is not necessarily identical to the structure in the 3*s* Rydberg state, it is probably quite similar, and Table 1 shows a reasonable agreement. The most notable difference between the ion minimum-energy structure and the vibrationally hot Rydberg excited-state structure seems to be in the low-frequency angular modes that are likely to be most affected by the high internal energy of the NMM molecule after internal conversion.

To ensure that the pool of possible molecular structures was sufficiently diverse, a second pool of structures was generated on the basis of a combination of comparatively low-level density functional theory and Hartree–Fock classical trajectories propagated on the ground state of the cation of NMM. As the topology of the cationic state of the molecule is expected to be similar to that of the Rydberg states of the neutral molecule, the conformational spaces constructed from the two are also expected to be similar. The results using this second pool (under the ion-surface dynamics pool column in Table 1) generally agree favourably with the high-level computation result (under the Rydberg-surface dynamics pool column in Table 1). The small discrepancy shown in torsional angles from

two different pools is mainly due to the substantially smaller number of geometries used in the ion-surface dynamics pool compared with the Rydberg-surface dynamics pool (further details in the Methods). This leads to a much lower local structure density around the true structure contained in the ion-surface pool compared to the Rydberg-surface pool. The consistency of the results obtained using the different pools demonstrates that the determination of molecular structures is robust with respect to the method used to generate the pool of structures. It should be noted, however, that because the calculated percent difference scattering pattern requires a simulated ground state scattering pattern as a reference, our method does depend on an accurate ground-state input structure. Given that the excited-state structure we determine is in good agreement with the calculated structure of the ground-state ion (Table 1), the ground-state input structure is inferred to be quite accurate.

Analysis of the structural dynamics. Given the ability to determine precise excited state molecular structures for each time point, we are now in a position to assemble a graphical representation of the time-dependent molecular structures in the form of a molecular movie. For this illustration, the geometry that gives the smallest-fit errors across all 21 non-hydrogenic interatomic distances is chosen as the representative geometry. By stitching together the images at each time point, the dynamical motions of the vibrating molecule are obtained (an animation is shown in Supplementary Video 2). An examination of the time dependence of some select structural parameters (Fig. 3) reveals the source of the dynamics observed in the experimental difference scattering pattern. Analysis of individual structural parameters indicates that the transient signal is dominated by signals arising from interatomic distances that involve the heavier atoms (rather than hydrogen atoms), which change following excitation (these include all of the distances between C5 and the other heavy atoms, as well as the O–N distance). Selected representative time-dependent structural parameters are fitted to a dynamical model that includes the contributions described above. The O–N–C5 angle (refer to Fig. 1 for atom labels) has an oscillatory period of 619 ± 22 fs, whereas the C5–N–C4–C3 torsional angle oscillates with a 613 ± 14 fs period. Both of these values are in good agreement with the fits to the overall scattering signal oscillation period of 623 ± 19 fs, and the previous photoelectron spectroscopic measurement at 208 nm (630 ± 13 fs)[19]. This indicates that the primary driver of the observed oscillation is the planarization motion of the amine group. For comparison, Fig. 3 includes the time dependence of the C2–C1–C4–C3 torsional angle, which does not participate in this motion. This torsional angle remains essentially unchanged during vibrational motion.

The time-dependent molecular structures also reveal that the oscillation in O–N–C5 angle dephases with an exponential time constant of 1,490 ± 785 fs, whereas the C5–N–C4–C3 torsional angle dephases in 1,900 ± 876 fs. Both of these time constants are larger than the damping in the overall signal intensity (635 ± 116 fs), although we note the relatively large errors in these determined values (see Supplementary Section 1 for details). This suggests that the decomposition of the overall scattering signals into specific, time-dependent geometrical parameters allows a more comprehensive understanding of the oscillatory umbrella motion than direct dynamic analysis of the overall scattering signal. Although the umbrella motion drives the relaxation of energy into the bath of vibrational states, its coherence may persist for longer than previously thought, and longer than analysis of the overall signal intensity would suggest.

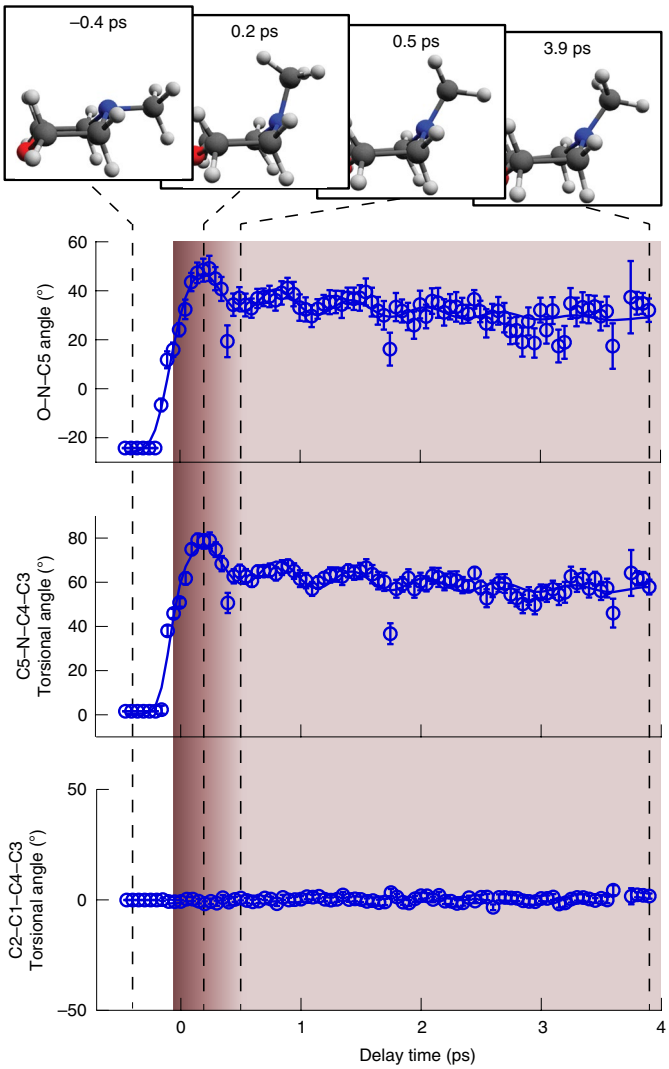

Fig. 3 | Time-dependent plots of selected structural parameters of NMM following Rydberg excitation. The O–N–C5 angle (top), the C5–N–C4–C3 torsional angle (middle) and the C2–C1–C4–C3 torsional angle (bottom), extracted from the structural determination as described in the text, are shown along with their respective 1σ error bars. The dynamic fits to the respective vibrational motions of the O–N–C5 angle and C5–N–C4–C3 torsional angle are also shown as solid lines. The approximate lifetime of the initially excited 3p_z Rydberg state (determined from photoelectron measurements in ref. [19]) is shown as a dark red shaded region, which corresponds to the 3s state when the colour is lighter. Example molecular structures for selected time points are also shown. A full animation is given in Supplementary Video 2.

Conclusions

In summary, we have captured transient molecular scattering signals that reveal the time-dependent excited-state molecular structure of NMM following Rydberg excitation. Precise molecular structures are obtained by reference to a large pool of potential structures generated computationally, with the resulting structures shown to be robust with respect to the choice of computational method. The resulting time-dependent molecular structure uncovers the vibrational motions in an excited polyatomic organic molecule. We observe large amplitude vibrations of the amine planarization mode and its dephasing on a picosecond timescale. It seems that the coherence of the vibrational motion survives the electronic relaxation[19] and persists for multiple vibrational periods. Although the overall signal intensity reflects the motions in many vibrational modes, and therefore has a faster apparent dephasing, the time dependence of specific structural parameters suggests that the intrinsic dephasing of the motions may be much slower than previously recorded.

The optical excitation in this instance is primarily a one-electron effect, and occurs on a background of the 56 electrons in the molecule. Because the scattering signals arise from the interference of scattering from different parts of the molecule, the excitation of a single electron leads to an effect on the scattering signal of about ~0.2% with the excitation fraction in the present experiment (Fig. 2), which is well within the experimental detection limit of ~0.05%. On the basis of our study, it is now conceivable that both vibrational structural motions and electron density changes can be observed during chemical reactions, which opens the door to observe (in real time) the formation and destruction of chemical bonds. Application to a variety of chemical reactions (including electrocyclic and charge transfer reactions) could provide previously unattainable experimental insights into chemical bonding and charge migration during reactions.

Methods

Experimental methods. The X-ray scattering measurements were performed in the coherent X-ray imaging instrument[30] at the LCLS[31] at the SLAC National Accelerator Laboratory. The 200 nm pump laser was the fourth harmonic of a 120 Hz Ti:sapphire laser with an ~80 fs pulse duration with ~1 μJ per pulse on target and a ~1.5 nm spectral bandwidth. The X-ray probe pulse was generated from LCLS, which operated at 120 Hz with ~10^{12} photons per pulse at 9.5 keV photon energy with a 20 eV full-width at half-maximum bandwidth and a ~30 fs pulse duration. The cross-correlation time of the pump and probe pulses was determined to be 89 ± 7 fs from the onset of the observed time-dependent scattering signals. The gaseous NMM sample pressure was controlled by a piezoelectric needle valve to ~7 torr of pressure at the interaction region. The gas cell and the CSPAD detector are in vacuum, with an average background pressure outside of the scattering cell of 2.6×10^{-4} torr, which is mostly comprised of the NMM that flows out of the windowless scattering cell. The pulse energy and gas pressure were optimized for a reduced background signal and a <10% excitation probability. The interaction length was kept small at 2.4 mm, which prevented excessive Beer–Lambert attenuation of the UV beam at the downstream end of the interaction region.

To collect time-resolved scattering patterns, the pump–probe delay time was controlled by a motorized delay stage, and the shot-to-shot timing jitter of the X-ray beam was monitored with a specialized timing tool[32]. The actual time delay of each shot was then determined to be the sum of the laser stage position and the edge position of the time tool. Furthermore, the shot-to-shot X-ray intensity was monitored by a photodiode downstream of the scattering cell. To achieve the necessary noise level (<0.1%), it was necessary to calibrate the intensity after the diffractometer set-up, because the X-ray also has spatial jitter that affects the transmission of the X-ray through the Pt pinholes (see Fig. 1).

The scattered X-rays were detected via a 2.3-megapixel CSPAD[24]. Details of the detector calibration, as well as the analysis of the measured scattering signals, are presented in Supplementary Section 1, as well as in the Supplementary Information of ref. [33].

Computational methods. To calculate the percent difference scattering signal caused by electronic excitation and by nuclear vibrational motions (see Fig. 2), the equatorial and axial geometries were optimized using the B3LYP/6-311++G(*d*,*p*) method for the neutral ground state, and the planar geometry was optimized using B3LYP/6-311++G(*d*,*p*) for the ionic ground state. The selected structural parameters of the optimized ionic ground state are shown in Table 1 in the ion structure column. The structure of the neutral ground-state equatorial geometry was further optimized at the CASSCF(2,5)/6-311+G(*d*) level and was used to simulate the ground-state scattering pattern as a reference. The selected structural parameters of the optimized neutral ground state are also presented in Table 1 in the ground-state structure column. The ab initio wavefunctions used to simulate the scattering patterns in the 3*s* and 3*p* states were calculated using the SA5-CAS(2,5)/6-311++G(*d*,*p*) method for the equatorial and planar NMM structures. All ab initio calculations were performed using the MOLPRO electronic structure software package[34,35], and scattering patterns were calculated using our own computer codes documented in refs. [27,28,36].

Using a total of 107 trajectories, we obtained approximately one million molecular geometries. We simulated the Rydberg-surface dynamics of photoexcited NMM using the SHARC[37–39] code interfaced with MOLPRO. SHARC treats nuclear motions classically, but non-adiabatic effects were included using the fewest-switches surface-hopping approach. The dynamics was propagated on the four lowest singlet electronic excitation states. The structures sampled from a Wigner distribution were initially populated to the 3*s* and three 3*p* states on the basis of their oscillator strengths, with 107 trajectories run for 1,000 fs. The electronic structure calculations during the dynamics were run at the SA5-CAS(2,5)/6-311+G(*d*) level of theory. A pool of 1,070,107 (greater than 10^6) geometries was extracted from the simulations. To test the dependence of the structure determination on the level of theory used, an ion-surface dynamics simulation was also performed. In this simulation, the nuclei are still treated classically, whereas electrons are treated quantum mechanically and calculated on the ion ground-state surface instead of the neutral Rydberg surfaces. We deliberately chose the ion surface rather than the Rydberg surface for this simulation to further test the independence of the resulting structure determination on the method used to create the pool of structures. In half of the trajectories, the UHF/6-311+G(*d*) method was used to calculate the ion state NMM at each time step, whereas in the other half, density functional theory (using the Perdew–Burke–Ernzerhof functional) was used instead. Combined, 173,997 geometries were obtained by the ion-surface dynamics simulations. Further details of the structural determination are included in Supplementary Section 2.

Data availability

The raw experimental data are archived on SLAC's internal file system. The raw pools of computed structures are stored locally at Brown University. All raw data are available from the corresponding author on reasonable request.

Code availability

The calculation of elastic scattering patterns from ab initio wavefunctions has been discussed in earlier publications[27,28,36]. The codes used to calculate scattering patterns, process the experimental data and perform the structural determination analysis are available from the corresponding author on reasonable request.

Received: 20 December 2018; Accepted: 10 June 2019;
Published online: 8 July 2019

References

1. Heller, E. J. Bound-state eigenfunctions of classically chaotic Hamiltonian systems: scars of periodic orbits. *Phys. Rev. Lett.* **53**, 1515–1518 (1984).
2. Tannor, D. J. *Introduction to Quantum Mechanics: A Time-dependent Perspective* (University Science Books, Sausalito, 2007).
3. Marcus, R. A. Electron transfer reactions in chemistry: theory and experiment. *Angew. Chem. Int. Ed.* **32**, 1111–1121 (1993).
4. Peirce, P., Dahleh, M. A. & Rabitz, H. Optimal control of quantum-mechanical systems: existence, numerical approximation, and applications. *Phys. Rev. A* **37**, 4950 (1988).
5. Zewail, A. H. Femtochemistry: atomic-scale dynamics of the chemical bond using ultrafast lasers (Nobel lecture). *Angew. Chem. Int. Ed.* **39**, 2586–2631 (2000).
6. Lambert, W. R., Felker, P. M. & Zewail, A. H. Quantum beats and dephasing in isolated large molecules cooled by supersonic jet expansion and excited by picosecond pulses: anthracene. *J. Chem. Phys.* **75**, 5958–5960 (1981).
7. Minitti, M. P. et al. Imaging molecular motion: femtosecond X-ray scattering of an electrocyclic chemical reaction. *Phys. Rev. Lett.* **114**, 255501 (2015).
8. Glownia, J. M. et al. Self-referenced coherent diffraction X-ray movie of ångstrom- and femtosecond-scale atomic motion. *Phys. Rev. Lett.* **117**, 153003 (2016).
9. Küpper, J. et al. X-ray diffraction from isolated and strongly aligned gas-phase molecules with a free-electron laser. *Phys. Rev. Lett.* **112**, 083002 (2014).
10. Barty, A., Küpper, J. & Chapman, H. N. Molecular imaging using X-ray free-electron lasers. *Annu. Rev. Phys. Chem.* **64**, 415–435 (2013).
11. Harb, M. et al. Electronically driven structure changes of Si captured by femtosecond electron diffraction. *Phys. Rev. Lett.* **100**, 155504 (2008).
12. Ischenko, A. A., Weber, P. M. & Dwayne Miller, R. J. Capturing chemistry in action with electrons: realization of atomically resolved reaction dynamics. *Chem. Rev.* **117**, 11066–11124 (2017).
13. Yang, J. et al. Diffractive Imaging of coherent nuclear motion in isolated molecules. *Phys. Rev. Lett.* **117**, 153002 (2016).
14. Yang, J. et al. Imaging CF_3I conical intersection and photodissociation dynamics with ultrafast electron diffraction. *Science* **361**, 64–67 (2018).
15. Zewail, A. H. 4D ultrafast electron diffraction, crystallography, and microscopy. *Annu. Rev. Phys. Chem.* **57**, 65–103 (2006).
16. Budarz, J. M. et al. Observation of femtosecond molecular dynamics via pump–probe gas phase x-ray scattering. *J. Phys. B* **49**, 34001 (2016).
17. Minitti, M. P. et al. Toward structural femtosecond chemical dynamics: imaging chemistry in space and time. *Faraday Discuss.* **171**, 81–91 (2014).
18. Williamson, J. C., Cao, J., Ihee, H., Frey, H. & Zewail, A. H. Clocking transient chemical changes by ultrafast electron diffraction. *Nature* **386**, 159–162 (1997).
19. Zhang, Y., Jónsson, H. & Weber, P. M. Coherence in nonradiative transitions: internal conversion in Rydberg-excited *N*-methyl and *N*-ethyl morpholine. *Phys. Chem. Chem. Phys.* **19**, 26403–26411 (2017).
20. Waters, M. D. J. et al. Symmetry controlled excited state dynamics. *Phys. Chem. Chem. Phys.* **21**, 2283–2294 (2019).
21. Yong, H. et al. Determining orientations of optical transition dipole moments using ultrafast X-ray scattering. *J. Phys. Chem. Lett.* **9**, 6556–6562 (2018).

22. Zhang, Y., Deb, S., Jónsson, H. & Weber, P. M. Observation of structural wavepacket motion: the umbrella mode in Rydberg-excited N-methyl morpholine. *J. Phys. Chem. Lett.* **8**, 3740–3744 (2017).
23. Dsouza, R., Cheng, X., Li, Z., Miller, R. J. D. & Kochman, A. Oscillatory photoelectron signal of *N*-methylmorpholine as a test case for the algebraic-diagrammatic construction method of second order. *J. Phys. Chem. A* **122**, 9688–9700 (2018).
24. Philipp, H. T., Hromalik, M., Tate, M., Koerner, L. & Gruner, S. M. Pixel array detector for X-ray free electron laser experiments. *Nucl. Instrum. Methods Phys. Res. A* **649**, 67–69 (2011).
25. Baskin, J. S. & Zewail, A. H. Ultrafast electron diffraction: oriented molecular structures in space and time. *ChemPhysChem* **6**, 2261–2276 (2005).
26. Lorenz, U., Møller, K. B. & Henriksen, N. E. On the interpretation of time-resolved anisotropic diffraction patterns. *New J. Phys.* **12**, 113022 (2010).
27. Northey, T., Zotev, N. & Kirrander, A. Ab initio calculation of molecular diffraction. *J. Chem. Theory Comput.* **10**, 4911–4920 (2014).
28. Northey, T., Moreno Carrascosa, A., Schäfer, S. & Kirrander, A. Elastic X-ray scattering from state-selected molecules. *J. Chem. Phys.* **145**, 154304 (2016).
29. Warren, B. E. *X-ray Diffraction* (Courier Corporation, 1969).
30. Liang, M. et al. The coherent X-ray imaging instrument at the Linac coherent light source. *J. Synchrotron Radiat.* **22**, 514–519 (2015).
31. Emma, P. et al. First lasing and operation of an ångstrom-wavelength free-electron laser. *Nat. Photon.* **4**, 641–647 (2010).
32. Bionta, M. R. et al. Spectral encoding method for measuring the relative arrival time between X-ray/optical pulses. *Rev. Sci. Instrum.* **85**, 083116 (2014).
33. Ruddock, J. M. et al. Simplicity beneath complexity: counting molecular electrons reveals transients and kinetics of photodissociation reactions. *Angew. Chem. Int. Ed.* **58**, 6371–6375 (2019).
34. Werner, H. J. et al. MOLPRO v.2012.1 (Molpro, 2012); https://www.molpro.net
35. Werner, H. J., Knowles, P. J., Knizia, G., Manby, F. R. & Schütz, M. Molpro: a general-purpose quantum chemistry program package. *WIREs Comput. Mol. Sci.* **2**, 242–253 (2012).
36. Moreno Carrascosa, A., Northey, T. & Kirrander, A. Imaging rotations and vibrations in polyatomic molecules with X-ray scattering. *Phys. Chem. Chem. Phys.* **19**, 7853–7863 (2017).
37. Mai, S. et al. SHARC v.2.0 (SHARC, 2018); https://sharc-md.org
38. Mai, S., Marquetand, P. & González, L. Nonadiabatic dynamics: the SHARC approach. *WIREs Comput. Mol. Sci.* **8**, 1370 (2018).
39. Richter, M., Marquetand, P., González-Vázquez, J., Sola, I. & González, L. SHARC: ab initio molecular dynamics with surface hopping in the adiabatic representation including arbitrary couplings. *J. Chem. Theory Comput.* **7**, 1253–1258 (2011).

Acknowledgements

The authors thank G. Stewart (SLAC National Accelerator Laboratory) for his generous assistance with preparing the figures. This work was supported by the US Department of Energy, Office of Science, Basic Energy Sciences, under award no. DESC0017995, and by the Army Research Office (grant no. W911NF-17-1-0256). Use of the LCLS, SLAC National Accelerator Laboratory, is supported by the US Department of Energy, Office of Science, Office of Basic Energy Sciences under contract no. DE-AC02-76SF00515.

Author contributions

P.M.W., A.K. and M.P.M. directed the project. M.L. and S.B. performed X-ray alignment and data collection. S.C., J.S.R. and M.P.M. performed laser alignment. T.J.L. and J.E.K. provided software support during the experiment. W.D. and Y.C. performed record keeping during the experiment. B.S., H.Y., N.Z., J.R., N.G., Y.C. and W.D. performed analyses on the experimental data. H.Y., N.Z. and D.B. performed theoretical computations and structural-determination analysis. B.S. planned the detailed experiments and implemented the data analysis. B.S. and H.Y. wrote the manuscript in consultation with the other authors.

Competing interests

The authors declare no competing interests.

Additional information

Supplementary information is available for this paper at https://doi.org/10.1038/s41557-019-0291-0.

Reprints and permissions information is available at www.nature.com/reprints.

Correspondence and requests for materials should be addressed to P.M.W.

Publisher's note: Springer Nature remains neutral with regard to jurisdictional claims in published maps and institutional affiliations.

nature chemistry

SUPPLEMENTARY INFORMATION

https://doi.org/10.1038/s41557-019-0291-0

In the format provided by the authors and unedited.

Ultrafast X-ray scattering reveals vibrational coherence following Rydberg excitation

Brian Stankus[1,4], Haiwang Yong[1,4], Nikola Zotev[2], Jennifer M. Ruddock[1], Darren Bellshaw[2], Thomas J. Lane[3], Mengning Liang[3], Sébastien Boutet[3], Sergio Carbajo[3], Joseph S. Robinson[3], Wenpeng Du[1], Nathan Goff[1], Yu Chang[1], Jason E. Koglin[3], Michael P. Minitti[3], Adam Kirrander[2] and Peter M. Weber[1]*

[1]Department of Chemistry, Brown University, Providence, RI, USA. [2]EaStCHEM, School of Chemistry, University of Edinburgh, Edinburgh, UK. [3]Linac Coherent Light Source, SLAC National Accelerator Laboratory, Menlo Park, CA, USA. [4]These authors contributed equally: Brian Stankus, Haiwang Yong. *e-mail: peter_weber@brown.edu

Ultrafast X-Ray Scattering Reveals Vibrational Coherence Following Rydberg Excitation

Brian Stankus[1†], Haiwang Yong[1†], Nikola Zotev[2], Jennifer Ruddock[1], Darren Bellshaw[2], Thomas J. Lane[3], Mengning Liang[3], Sébastien Boutet[3], Sergio Carbajo[3], Joseph S. Robinson[3], Wenpeng Du[1], Nathan Goff[1], Yu Chang[1], Jason E. Koglin[3], Michael P. Minitti[3], Adam Kirrander[2], Peter M. Weber[1*]

[1] Department of Chemistry, Brown University, Providence, RI 02912, USA
[2] EaStCHEM, School of Chemistry, University of Edinburgh, David Brewster Road, Edinburgh EH9 3FJ, UK
[3] Linac Coherent Light Source, SLAC National Accelerator Laboratory, Menlo Park, CA, USA
*** Correspondence to: peter_weber@brown.edu**
† These authors contributed equally to this work.

Supplementary Information:

1. Additional Experimental Methods and Analysis

2. Additional Structural Determination Analysis

1. Additional Experimental Methods and Analysis

The position of the detector relative to the interaction region was determined by fitting the experimentally measured scattering image of gaseous ground-state NMM to the theoretical scattering pattern, calculated with the Independent Atom Model and applying the anisotropic scattering dependence arising from the linearly polarized X-ray beam. The calibrated Cartesian coordinates of each pixel were converted to the scattering vector q and azimuthal angle ϕ according to Equations 1 and 2. The z direction is defined as the x-ray propagation axis, and the detector lies in the xy plane.

$$q = \frac{4\pi}{\lambda}\sin\left(\frac{1}{2}\mathrm{atan}\left(\frac{\sqrt{x^2+y^2}}{z}\right)\right) \quad (1)$$

$$\phi = \mathrm{atan2}(y,x) \quad (2)$$

The calibrated time-dependent scattering images are expressed as a percent difference relative to the ground-state scattering pattern, as expressed in Main Text Eq. 1. An animation of the scattering is shown in Supplementary Movie 1. The measured signals were averaged over all four azimuthal angle quadrants and then replicated over the entire circle prior to further analysis. The measured scattering signals suffer from a poor signal-to-noise ratio at large scattering angles ($q > \sim 4$ Å^{-1}) due to the low scattering amplitude as well as a smaller collection efficiency due to the shape of the CSPAD detector. In the structural determination analysis, the signals were weighted according to their shot noise (illustrated as error bars in Fig. 5) to ensure the determined structures were unbiased by the noise observed at large scattering angles.

The isotropic and anisotropic components of the scattering signal were decomposed as described in the main text, and the components are shown in Fig. 1. The anisotropic signal at early pump-probe delay times has been analyzed previously in detail[1]. Briefly, this anisotropy arises from preferential photo-excitation of molecules whose transition dipole moments align

with the polarization direction of the optical pulse in the laboratory frame. Analysis of this signal indicates that the initially excited state is the $3p_z$ Rydberg state (shown in Main Text Fig. 2). The temporal evolution of the anisotropic scattering signal arises from the motions of the rotational wavepacket, which will be the subject of further study.

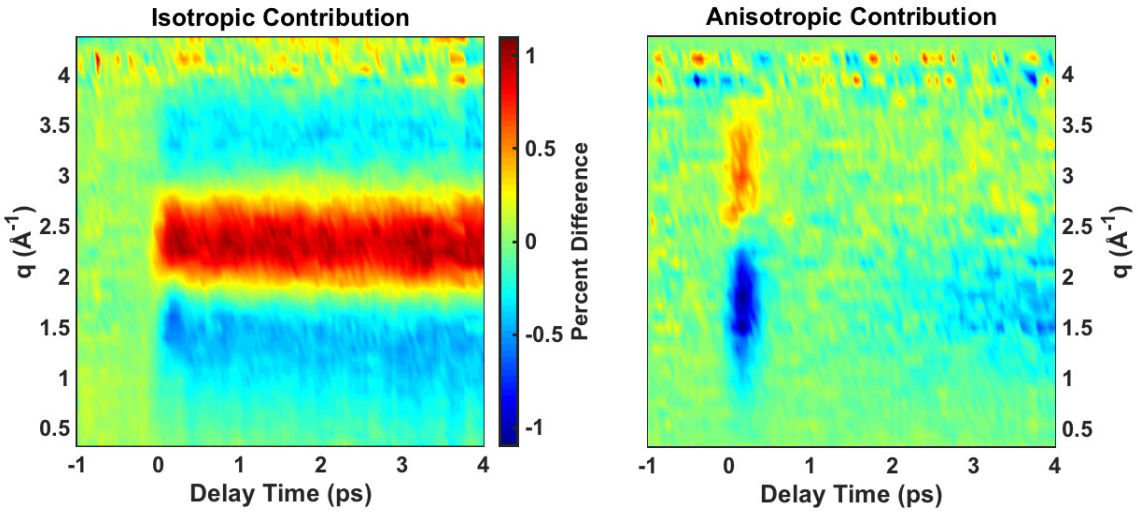

Fig. 1: The isotropic and anisotropic components of the experimentally measured difference scattering signal.

In order to determine the time dependence of the isotropic difference signal, the intensity and peak center (in q) of each of the two strongest extrema (in the ranges 1.0-1.8 $Å^{-1}$ and 2.0-2.8 $Å^{-1}$) were analyzed. To precisely determine the location and extremum of each band, the difference signal was fit to three overlapping Gaussian functions at each time point, and then the exact center position and extreme value were plotted as a function of time (see Fig. 2). The dynamics of the center position and difference signal level were fit to the same dynamical model referred to in the Main Text. This model is given by Eq. 3-5, where the actual fitting function is expressed as Eq. 5,

$$f(t) = c_1 + \left[\left(c_2 + c_3 \sin\left(\frac{2\pi t}{T} - \phi\right) e^{-(t-t_0)/\tau_{damping}}\right) + c_4 e^{-(t-t_0)/\tau_{IVR}}\right] H(t - t_0) \quad (3)$$

$$g(t) = \frac{1}{\sigma_{IF}\sqrt{2\pi}} e^{-(t-t_0)^2/2\sigma_{IF}^2} \quad (4)$$

$$I(t) = \int f(t')g(t - t')\, dt' \quad (5)$$

and $H(t\text{-}t_0)$ is the Heaviside function. The time dependence of all four components were fit simultaneously with the shared parameters shown in Table 1. The results of this fit to the experimental signal are shown in Fig. 2. In addition, results of this fit to the determined O-C5 distance are shown in Fig. 3 along with the N-C5 distance for comparison. A summary of the results for both the experimental signal and selected structural parameters are also shown in Table 1.

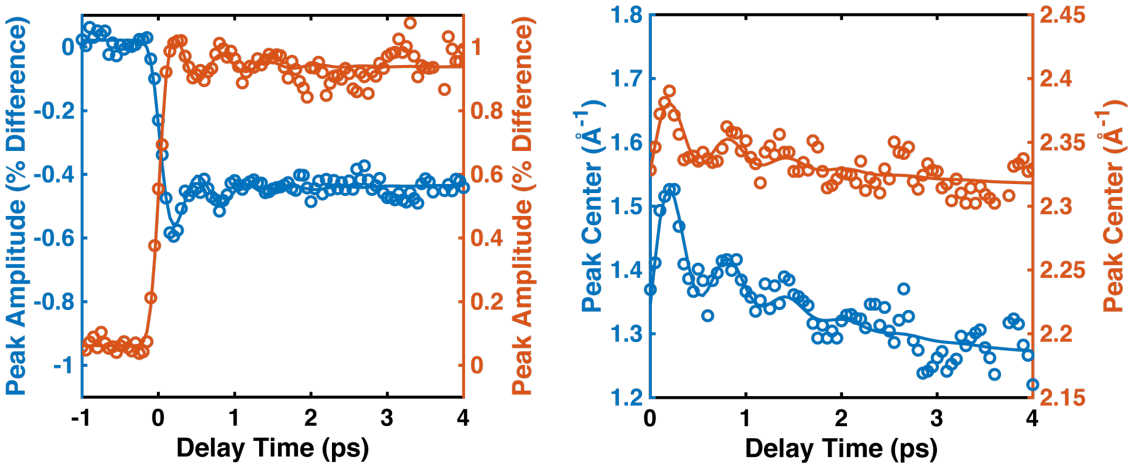

Fig. 2: Peak amplitude and center position for the extrema in the ranges 1.0-1.8 Å^{-1} (blue) and 2.0-2.8 Å^{-1} (orange), along with their fits as described in the text.

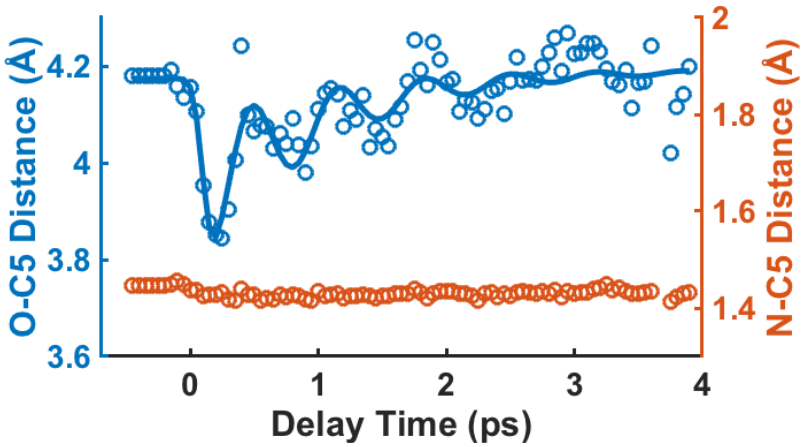

Fig. 3: Time-dependent plots of the O-C5 and N-C5 interatomic distances extracted from the structural determination analysis described in the Main Text, as well as the dynamic fit to the time dependence of the O-C5 distance as described above.

Table 1: Optimized fitting parameters to the dynamical model shown in Equations 3-5.

Parameter	Exp. Signal	O-N-C5 Angle	C5-N-C4-C3 Torsional Angle	O-C5 Distance
t_0 (fs)	-3 ± 8	-50 ± 24	-44 ± 14	48 ± 20
σ_{IF} (fs)	89 ± 7	100 ± 28	73 ± 17	57 ± 23
T (fs)	623 ± 19	619 ± 22	613 ± 14	674 ± 27
Φ (rad)	-0.54 ± 0.31	-0.97 ± 0.59	-1.07 ± 0.36	0.64 ± 0.44
$\tau_{damping}$ (fs)	635 ± 116	1490 ± 785	1900 ± 876	1010 ± 363
τ_{IVR} (fs)	1750 ± 465	1620 ± 1140	1310 ± 660	980 ± 300

2. Additional Structural Determination Analysis

The least-squares fitting error distribution for two structural parameters, the O-C5 and O-N distances, for a single time point, are shown in Fig. 4. The blue dots represent the inverse of the fitting errors from the geometries in the pool at a certain time point. For each distance, only the best-fitting structures are retained. The black curves are fits using three Gaussian functions to account for the skewness of the profiles. The peak centers of the fits are extracted as the value of the structural parameter for each time point. To better illustrate the time-dependent molecular motion, the geometry that gives the smallest fit errors across all 21 non-hydrogenic interatomic distances is chosen as the representative geometry. An animation of the molecular structure as a function of time (generated with Jmol[2]) is included as Supplementary Movie 2.

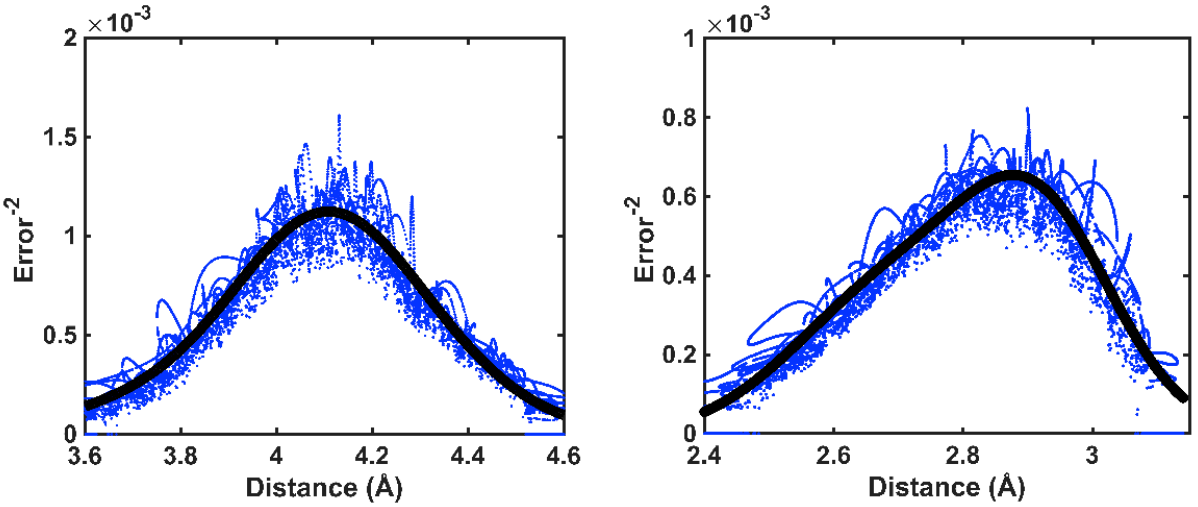

Fig. 4: The inverse of the least-squares fitting error as a function of the given structural parameter and the fits as described in the text. Left: O-C5 distance at 0.05 ps delay time. Right: O-N distance at 2.65 ps delay time.

The scattering patterns generated from the determined molecular structure at several representative time points are compared with the experimental signals in Figure 5.

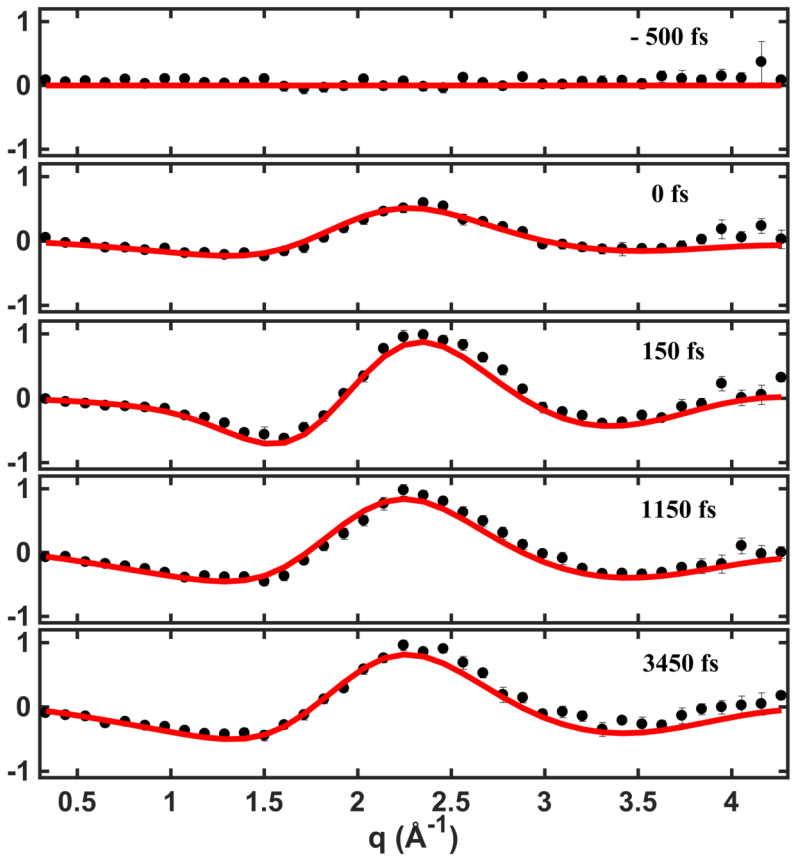

Fig. 5: The experimentally measured percent difference scattering signals (black), along with the estimated shot noise error at each point in momentum transfer space (error bars, shown to 3σ), as well as the simulated scattering pattern generated from the determined structure (red) at several representative delay time points.

To further demonstrate the independence of this structure determination on the computational method, the RMSD spread around the centroid of the entire set of 1,070,107 geometries is shown in Fig. 6. The molecular images indicate where the recovered geometries from the fitting procedure fall within this distribution. All geometries found in the molecular movie are confined in the range 0.22-0.31 Å from the centroid. The Rydberg state geometries are

most rigorously sampled on account of the surfaces used in the simulation. However, the distribution spreads across a wide range of RMSD values showing the large variety of structures in the pool, including some unphysical geometries in the tail of the distribution. The thorough sampling in the Rydberg geometry region allows for the high precision of the refinement process while the spread of possible geometries guarantees that the result remains reasonably unbiased.

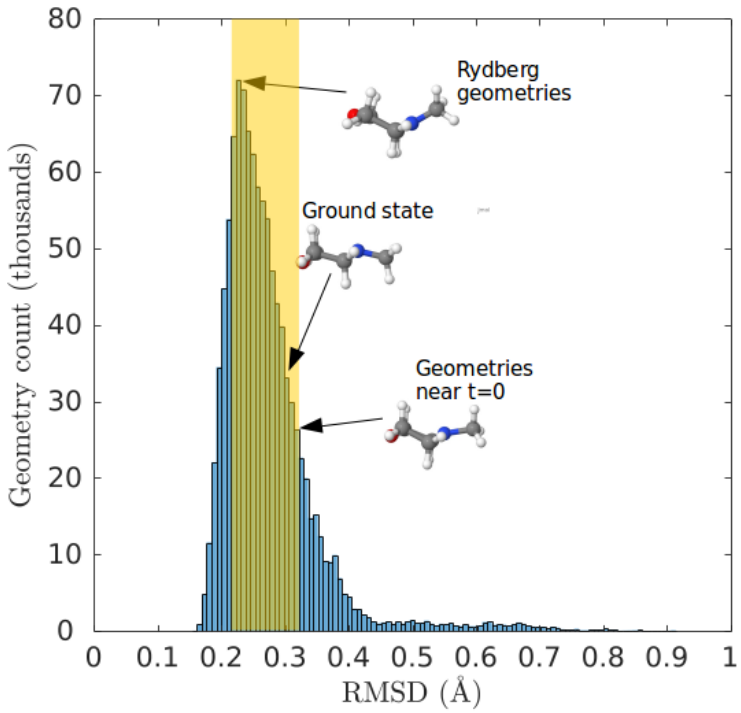

Fig. 6: RMSD spread of the geometries around the centroid of the entire set of 107 Rydberg-surface trajectories. The shaded region indicates the range in which all geometries from the molecular movie are found.

References

[1] Yong, H. *et al.* Determining Orientations of Optical Transition Dipole Moments Using Ultrafast X-ray Scattering. *J. Phys. Chem. Lett.* 6556–6562 (2018). doi:10.1021/acs.jpclett.8b02773

[2] Jmol: an open-source Java viewer for chemical structures in 3D. http://www.jmol.org/.

6.3 Conclusion

The high-throughput fitting method applied here demonstrates that it is possible to retrieve structural dynamics from UXS experiments on a femtosecond time scale with a high spatial resolution. However, there are three important limitations that might hinder the application of the approach to other molecules. Firstly, the reliance on tight geometrical constraints is of crucial significance here. Not only does it reduce the conformational space and thus, the number of geometries needed for the fit, but it also counteracts the limited information available in the scattering signal. Collecting large scattering angles and/or increasing the X-ray photon energy can in principle provide a higher resolution, which would lessen the dependence on theoretical input. Using the anisotropic component of the scattering could also achieve the same end result, if a clear methodology for its analysis was developed. Secondly, at each time point of the experiment, the scattering pattern gets assigned to a single structure. That completely neglects the spread of the nuclear wave packet. While the coherent vibrations seen for NMM indicate a narrow nuclear wave packet, that does not have to be the case in general. Similarly, the method would not be able to cope with situations when multiple reaction channels are present. If that was the case, each channel would need to be modelled by a separate structure, and a parameter to control the branching ratios would need to be introduced. The retrieval procedure would then run into overfitting issues. Finally, the dynamics in NMM evolves only on a family of Rydberg states. These are quite similar and their difference with the IAM is stable across the structural space. Subtracting it from the rest of the analysis is trivial. However, if the molecule undergoes internal conversion to a valence state that is significantly different, the electronic contribution would need to be modelled dynamically. Currently, there is no established way of doing that.

Chapter 7

Observing Photodissociation

7.1 Introduction

This chapter presents work which is reproduced with permission from Jennifer M. Ruddock, **Nikola Zotev**, Brian Stankus, Haiwang Yong, Darren Bellshaw, Sébastien Boutet, Thomas J. Lane, Mengning Liang, Sergio Carbajo, Wenpeng Du, Adam Kirrander, Michael P. Minitti and Peter M. Weber. "Simplicity beneath Complexity: Counting Molecular Electrons Reveals Transients and Kinetics of Photodissociation Reactions". *Angewandte Chemie International Edition* **58**, 6371 (2019).

Section 3.5 described the process of dissociation as observed in UXS experiments. As the title of the work presented in this chapter suggests, the loss of interference (also referred to as coherence in the text that follows) can be used as a simple but effective measure of the rate of dissociation. The dissociation reaction studied follows from the photoexcitation of TMA by a 200 nm pump pulse, which prepares the molecule in a $3p_z$ Rydberg state (possibly with a small population fraction on $3p_x/3p_y$), as indicated by the anisotropy of the scattering pattern shown in Figure 7.1. Modelling of the observed rates suggests the presence of two independent reaction channels to dissociation. The first one is fast, and is hypothesised to result from a conical intersection between the initially prepared state and the dissociative σ^* state. With reference to the *ab initio* computational results, the slower reaction channel has been attributed to a faster decay to a 3s Rydberg state, which is followed by a slow coupling to the same σ^* surface.

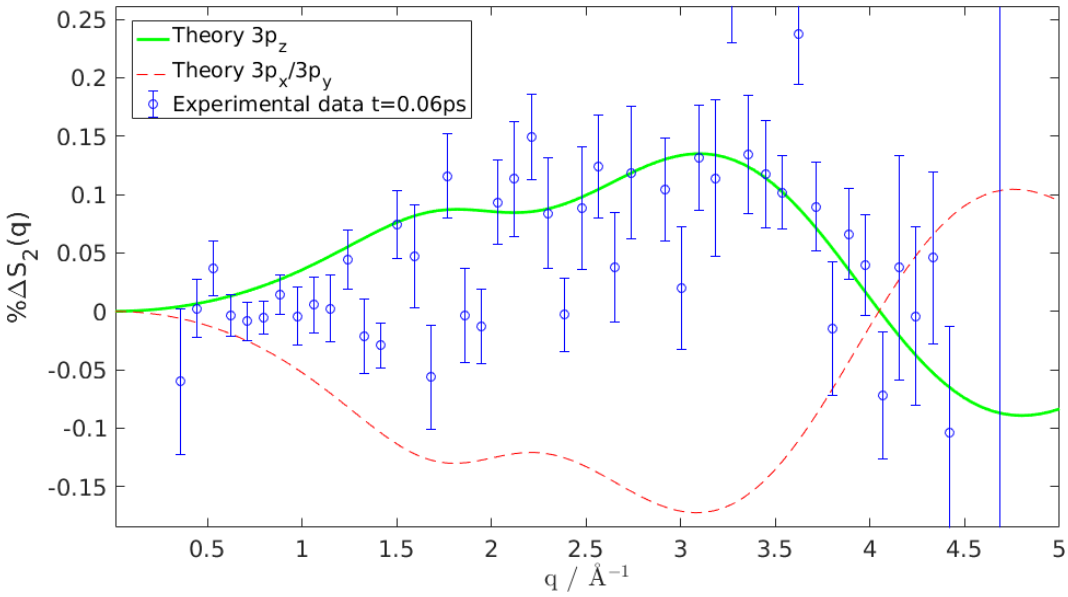

FIGURE 7.1: A comparison between the experimental anisotropy amplitude at t=0.06 ps and the simulated anisotropy from a perfect cosine squared distribution. The signal is expressed as percentage intensity change. The theoretical anisotropy is calculated for $3p_x$, $3p_y$ and $3p_z$ Rydberg states and scaled to match the experimental excitation fraction. The $3p_x$ and $3p_y$ states and anisotropy are degenerate on account of the symmetry of the molecule.

The dissociation of TMA leads to two products, methyl and dimethylamine (DMA) radicals. The DMA fragment is not stable, as indicated by other studies [123, 124], and further dissociates. The second dissociation is not observed on the time scale of the experiment. The structure of the transient DMA fragment was not known from previous studies. In principle, there are only a few techniques that can provide this information. It is shown that it is possible to obtain the structure of the DMA radical, by performing a least-squares fit to the scattering signal after the initial dissociation reaction has been completed.

Photodissociation Reactions

International Edition: DOI: 10.1002/anie.201902228
German Edition: DOI: 10.1002/ange.201902228

Simplicity Beneath Complexity: Counting Molecular Electrons Reveals Transients and Kinetics of Photodissociation Reactions

Jennifer M. Ruddock, Nikola Zotev, Brian Stankus, Haiwang Yong, Darren Bellshaw, Sébastien Boutet, Thomas J. Lane, Mengning Liang, Sergio Carbajo, Wenpeng Du, Adam Kirrander, Michael Minitti, and Peter M. Weber**

Abstract: *Time-resolved pump–probe gas-phase X-ray scattering signals, extrapolated to zero momentum transfer, provide a measure of the number of electrons in a system, an effect that arises from the coherent addition of elastic scattering from the electrons. This allows to identify reactive transients and determine the chemical reaction kinetics without the need for extensive scattering simulations or complicated inversion of scattering data. We examine the photodissociation reaction of trimethylamine and identify two reaction paths upon excitation to the 3p state at 200 nm: a fast dissociation path out of the 3p state to the dimethyl amine radical (16.6 ± 1.2 %) and a slower dissociation via internal conversion to the 3s state (83.4 ± 1.2 %). The time constants for the two reactions are 640 ± 130 fs and 74 ± 6 ps, respectively. Additionally, it is found that the transient dimethyl amine radical has a N–C bond length of 1.45 ± 0.02 Å and a C–N–C bond angle of 118° ± 4°.*

The identification and characterization of short-lived and reactive intermediates in chemical reaction sequences remains a challenging problem. The large number of photons produced by X-ray free-electron Lasers allows us to study gas-phase samples[1–4] and the ultrashort pulse duration makes it possible to investigate the structure of transients that are not accessible with other methods.[5] We use the Linac coherent light source (LCLS) X-ray free-electron laser to measure ultrafast X-ray scattering during the photodissociation reaction of the molecule trimethylamine (TMA) excited by 200 nm light. The experiment reveals the reaction kinetics of the dissociation of TMA into methyl and dimethylamine radicals, and uncovers the structure of the reactive and short-lived dimethylamine radical transient.

While a full analysis of the X-ray scattering data is complicated, the reaction products and the kinetics can be identified from the X-ray scattering signal in the limit of vanishing momentum transfer vectors, $q \rightarrow 0$, that is, at small scattering angles. This conceptually simple yet powerful analysis relies on the fact that coherent elastic scattering in the gas-phase is an intramolecular phenomenon. While the scattering from different electrons in each molecule adds up coherently, the elastic scattering from different molecules, that is, intermolecular scattering, adds up incoherently. This is attributed to the random positions of the molecules in the gas and the large intermolecular distances compared to the X-ray wavelength.[6] At small angles, the elastic scattering is therefore proportional to the square of the number of electrons in one molecule. Consequently, as the molecules dissociate into smaller fragments, there is a characteristic decrease of the scattering signal at small angles.

Amines are an important group of molecules due to their use in fertilizers and biological processes. TMA is a prototypical tertiary amine with accessible spectroscopic properties. It is known to dissociate into radical transients, which, being unstable, are difficult to study but are important in combustion, atmospheric chemistry, and enzymatic processes. In general, dissociation reactions can be difficult to study spectroscopically, since spectroscopic properties change between reactant and products.[7]

The electronic structure and photodissociation dynamics of TMA have previously been explored using photoionization spectroscopy and molecular beam techniques. Cardoza et al. found that optical excitation at 207.8 nm initially prepares the $3p_z$ state.[8] Internal conversion leads to the $3p_x$ and $3p_y$ states with a time constant of 540 ± 75 fs and then to the 3s state with a time constant of 2.9 ± 0.2 ps, as shown in Figure 1.[9] At higher energy, reached by two-photon excitation with 400 nm, a slightly faster 3s internal conversion time constant of 2.0 ps was found.[8] Using time-of-flight photoionization with excitation at 193 nm, Forde et al.[10,11] found three dissociative channels: a dominant (72 ± 9 %) channel involving a sequential reaction to N-methylmethanimine (NMMA); a minor channel (27 ± 9 %) resulting in dimethylamine (DMA) and methyl radicals ejected with higher kinetic energy; and, possibly, a trace amount of a third channel involving a secondary dissociation of DMA resulting in NC_2H_4 and molecular hydrogen with low kinetic energy. In the dominant pathway, the initially excited TMA first dissociates into DMA and CH_3, and then DMA fragments to form NMMA and hydrogen atoms. Because the experiments by Forde et al. only identified the final reaction products, they could not measure the time scales of the kinetic steps nor confirm the electronic or geometrical structures of the DMA transients. The intermediate reaction steps and the nature of the transient

[*] J. M. Ruddock, B. Stankus, H. Yong, W. Du, Prof. P. M. Weber
Department of Chemistry, Brown University
324 Brook St, Providence, RI 02912 (USA)
E-mail: peter_weber@brown.edu

J. M. Ruddock, S. Boutet, T. J. Lane, M. Liang, S. Carbajo, M. Minitti
SLAC National Accelerator Laboratory
2575 Sandhill Rd, Menlo Park, CA 94025 (USA)
E-mail: minitti@slac.stanford.edu

N. Zotev, D. Bellshaw, A. Kirrander
EaStCHEM, School of Chemistry, University of Edinburgh
David Brewster Road, Edinburgh EH9 3FJ (UK)

Supporting information and the ORCID identification number(s) for the author(s) of this article can be found under: https://doi.org/10.1002/anie.201902228.

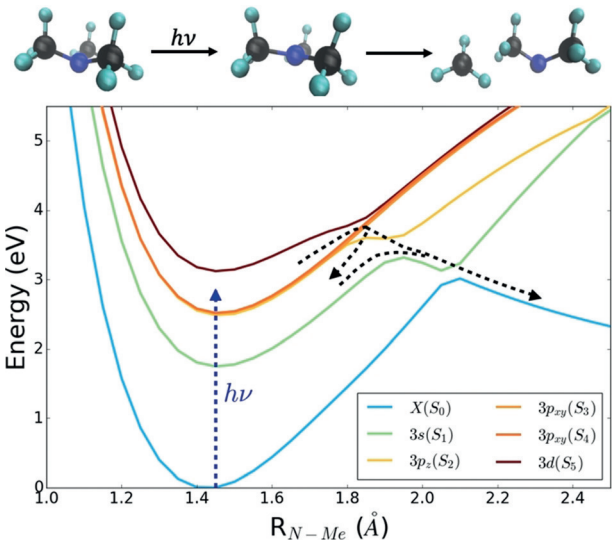

Figure 1. Reaction path of TMA upon UV excitation. Top: Schematic depiction of the dissociation of TMA upon UV excitation. Bottom: Adiabatic potential energy curves calculated at the state-averaged CASSCF level (SA6-CAS(2,6)/6-31+G*) using the 3s-optimized geometry, where a single N–Me distance was varied while all other coordinates were kept frozen. The states are labeled β(Sα), where β refers to the state character at the minimum energy geometry of the plot and α simply orders the adiabatic singlet states by energy. The blue dashed arrow indicates the excitation pulse. The black dashed arrows indicate the 3p→3s internal conversion and the dissociative pathway.

species therefore remain largely unknown. The time-resolved X-ray scattering experiment reported here provides the missing rate constants of the dissociation paths. Within the time window of the experiment, up to 1 ns after the initial excitation, we found no signature of the secondary dissociation of DMA into NMMA and hydrogen atoms, meaning that the DMA transient appears as a final reaction product.

Scattering signals were measured with the UV pump laser both on and off, giving rise to scattering patterns $I_{on}(q,t)$ and $I_{off}(q)$, where t is the delay time between the laser pump pulse and the X-ray probe pulse, and q is the amplitude of the momentum transfer vector. Details about the experiments are provided in the Supporting Information. It is convenient to express the pump–probe signal as a percent difference [Eq. (1)],

$$\%\Delta I(q,t) = 100\frac{I_{on}(q,t) - I_{off}(q)}{I_{off}(q)} \quad (1)$$

in which poorly defined experimental parameters such as background signals, pixel-to-pixel sensitivity variations of the detector, and gas-pressure fluctuations cancel out. The percent difference signal is proportional to the excitation fraction, which is kept low to minimize unwanted multiphoton processes.

The elastic scattering from a molecule is determined by its electron-density distribution[12] averaged over the vibrational and rotational degrees of freedom. In pump–probe experiments, the optical excitation might alter the electron density[13–16] and vibrational probability distributions,[4,5,15,17] and the laser and X-ray beam polarizations may cause anisotropies that combine with the rotational motions of the molecule to create alignment effects. The signals are furthermore averaged over the temporal profiles of the UV pump pulse and the X-ray probe pulse. To fully analyze pump–probe X-ray scattering patterns, all those phenomena need to be considered. The complexity of such a complete analysis constitutes a bottleneck, although successful examples have been achieved.[18–21]

Beneath this complexity, however, lies the opportunity to extract valuable information about chemical reaction kinetics by considering the total electron counts of the molecular scatterers. Polarization effects can be ignored since we only look at the isotropic scattering signal. Before dissociation, the scattering cross-section in the limit of zero momentum transfer, that is, $q\to0$, is given by [Eq. (2)]

$$\left(\frac{dI}{d\Omega}\right)(q\to 0) = \left(\frac{dI}{d\Omega}\right)_{Th} N^2, \quad (2)$$

where N is the number of electrons in a molecule and $(dI/d\Omega)_{Th}$ is the Thomson differential scattering cross-section,[6,15] with the square appearing due to the coherent addition of elastic scattering from different electrons within each molecule, as discussed in the introduction. As the molecules in the sample dissociate, resulting in a gaseous mixture of fragment molecules α with intermolecular distances that are large compared to the wavelength of the scattered X-ray radiation, the coherence of the waves scattered from different parts of the molecule is lost, so that their scattering signals add up incoherently for all but the smallest values of q. Therefore, for experimentally accessible ranges of q, the scattering from different fragments becomes additive such that [Eq. (3)],

$$\left(\frac{dI}{d\Omega}\right)(q\to 0) = \left(\frac{dI}{d\Omega}\right)_{Th} \sum_{\alpha} N_{\alpha}^2, \quad (3)$$

where $N=\Sigma_\alpha N_\alpha$ with N_α being the number of electrons in the fragments. This leads to the characteristic decrease in the small-angle scattering intensity. Of course, there is also the intermediate case in which a molecule is in the process of dissociation and an electron cannot be clearly associated with either fragment. However, presently we are interested in a qualitative analysis made possible by Equation (2) and (3), noting that the fraction of molecules at intermediate separation is negligible compared to the fraction of the reactant and product molecules at any given time.

With one nitrogen atom, three carbons, and nine hydrogen atoms, TMA has 34 electrons. The scattering signal extrapolated to $q\to0$ is therefore proportional to $34^2=1156$. The initial excitation to the 3p state and subsequent internal conversion to 3s changes the electron density distribution of the molecule and thereby the shape of the scattering signal in q space, but not the total electron count. Consequently, for $q\to0$, the percent difference given by Equation (1), considering the scattering signal from ground-state TMA and TMA in the excited 3s state, is expected to be zero. In contrast, for

the two fragment molecules DMA and CH_3, the $q \rightarrow 0$ scattering signal is proportional to $25^2 + 9^2 = 706$. Therefore, if the reaction to DMA and CH_3 is complete, the $q \rightarrow 0$ percent difference signal is reduced compared to the unreacted molecule by $100(706-1156)/1156 = -38.9\,\%$. We emphasize that there are no instrumental parameters in this percent difference. In an experiment, the percentage is coupled to the overall excitation probability, which is independent of the time delay and can therefore be separated in the analysis.

A selection of the pump–probe X-ray percent difference scattering curves, measured for q in the range from 0.3 $Å^{-1}$ to 4.7 $Å^{-1}$, are shown in Figure 2. Even though the gas pressure

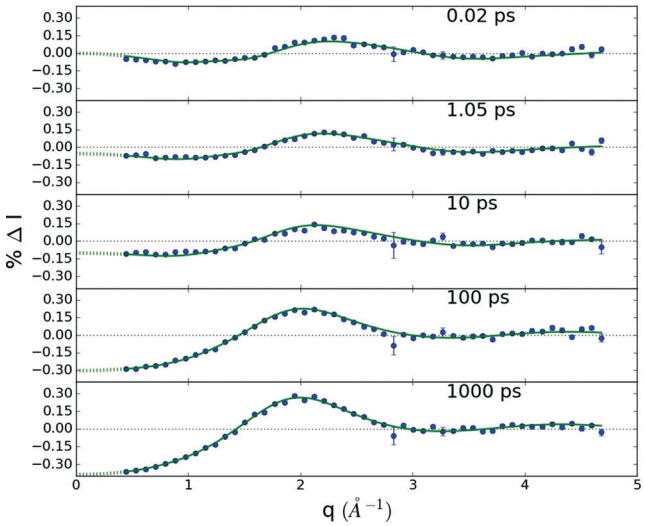

Figure 2. Experimental pump–probe X-ray scattering percent difference signals (blue dots) of TMA at the given delay times. The signals are scaled by the experimentally determined percent excitation of 1.83 %. The green solid lines are fits as described in the text, dashed lines are extrapolated for $q \rightarrow 0$. A dissociation reaction leads to a characteristic decrease of the signal at small values of q.

was small (6 torr) and the interaction length short (2.4 mm), the X-rays of LCLS are so bright that scattering patterns of excellent quality are obtained. Using a radio-frequency-based locking system,[22] the time delays between the UV pump pulses and the X-ray probe pulses were adjusted between −2 ps and 3 ns. For a finer resolution in the time delays, the pump–probe timing techniques previously reported were used.[17] Due to the small interaction region and large translational energy of the dissociation fragments, the 3 ns time point was not viable for analysis (see Supporting Information).

The postulated reaction scheme includes a two-step decay via the lower 3s(S1) Rydberg state as well as the possibility of a direct reaction out of the 3p(S2/S3/S4) manifold,

$$\mathrm{TMA}(3p) \rightarrow \begin{cases} \xrightarrow{k_0} p\ \mathrm{TMA}(3s) \xrightarrow{k_2} p\ (\mathrm{DMA} + \mathrm{CH_3}) \\ \xrightarrow{k_1} (1-p)(\mathrm{DMA} + \mathrm{CH_3}) \end{cases} \quad (4)$$

with rate constants k_0, k_1, and k_2, and a fraction $(1-p)$ of the excited molecules undergoing a single-step dissociation that has not been observed previously. The k_0 time constant is associated with internal conversion to 3s. Our experiment is blind to this process, but previous experiments determined the time constant $1/k_0$ to be 2.0 ps.[9] From the time sequence of the scattering patterns (Figure 2), we infer that the observed reaction is complete at 1 ns. This is apparent from the extrapolations to $q \rightarrow 0$ (green dotted lines), which show that low-q scattering decreases from 0 at small times to −0.389 at 1 ns, as expected. We can use this 1 ns pattern to determine the structure of the transient DMA radical (Figure 3). To calculate the percent difference scattering

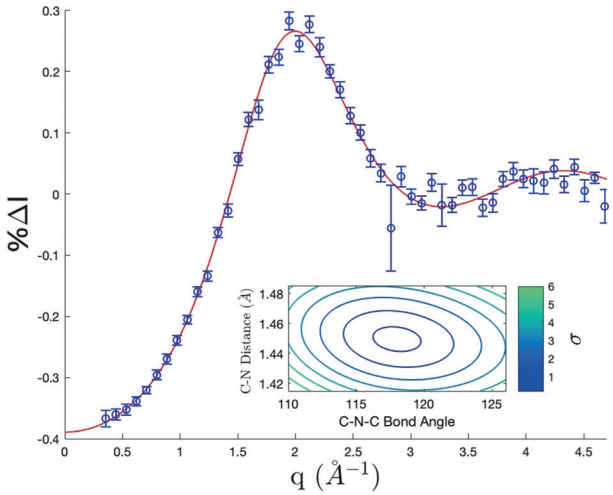

Figure 3. Difference scattering patterns of the DMA transient as obtained from the experimental data at long time delays (blue dots) and computed using an independent-atom model (red line). The red line extrapolates to −0.389 at $q \rightarrow 0$. Inset: residuals from the fit for different values of the bond length and bond angle. Contour lines are at 0.2, 1, 2, 3, 4, 5, and 6σ.

signal, we use the known structures of TMA[23] and the methyl radical.[24] Keeping the C–H distances in DMA fixed and varying the C–N bond lengths and the C–N–C bond angle, we can fit the experimental pattern. The resulting N–C bond length is 1.45 ± 0.02 Å and the C–N–C bond angle is $118 \pm 4°$. The structure calculated at CAS(3,3)/6-311 + G* has a bond length of 1.44 Å and a bond angle of 112°. We note that the nascent DMA radical might have substantial internal energy, which could result in a higher bond angle. The scattering signal of the electronically excited TMA species, given by the early time points before the reaction has significantly evolved, reflects both the changes in the electron density distribution upon electronic excitation and the high degree of vibrational excitation of the transients. A complete simulation of this pattern requires an in-depth quantum-mechanical analysis that will be presented in the future.

With the scattering signals of the early and late time points as experimentally determined, the kinetics of the reaction can be obtained by fitting the time dependent scattering patterns (Figure 2) to Equation (4) using the following equation [Eq. (5)]:

$$\begin{aligned} \%\,\Delta I(q,t) = & A_{\mathrm{TMA}}*(q)\left[(1-p)e^{-k_1 t} + pe^{-k_2 t}\right] \\ & + A_{\mathrm{DMA}}(q)\left[1-(1-p)e^{-k_1 t} - pe^{-k_2 t}\right] \end{aligned} \quad (5)$$

$A_{TMA^*}(q)$ and $A_{DMA^*}(q)$ are the scattering signals arising from the electronically excited TMA* and the $DMA + CH_3$ radical fragments, respectively. Equation (5) is simplified for the case where $k_1 \gg k_2$, as appropriate for this reaction, and recognizes that the analysis does not distinguish between the initially excited 3p(S2/S3/S4) states and the 3s(S1) state reached by internal conversion. Both states have a planar geometry around the central nitrogen, and the scattering signals of the diffuse 3p and 3s Rydberg states are experimentally indistinguishable. A best fit, shown in Figure 4, is obtained for $p = 0.834 \pm 0.012$, while time constants are determined as $1/k_1 = 640$ fs^{-1} and $1/k_2 = 74$ ps^{-1}. We note that we tried other schemes for the kinetics and found that this scheme, with $k_1 \gg k_2$, produced the best fit.

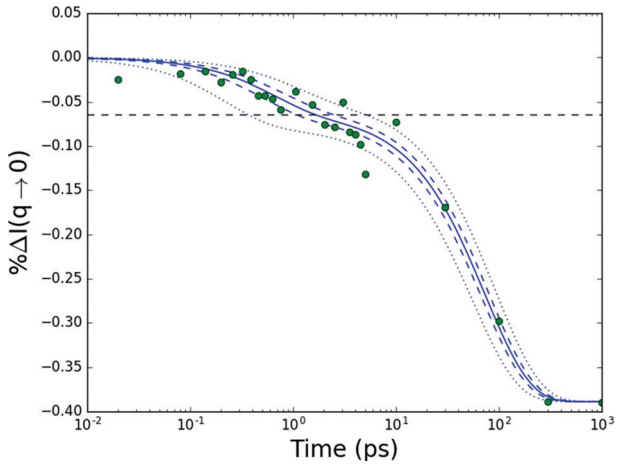

Figure 4. Time dependence of the decay of TMA upon excitation at 200 nm. The plot shows the percent difference scattering signal, Equation (1), extrapolated to $q \to 0$ and scaled by the percentage of excitation (green dots). The fit from Equation (5) (blue line), 1σ and 3σ tolerances (dashed and dotted blue lines, respectively) of the fit are also shown. The black dashed line is a 16.6% decrease in the $q \to 0$ scattering signal.

The identity of the reaction products and the bifurcation of the reaction can be immediately read out from the time dependence of the $q \to 0$ scattering signals in Figure 4. Only 83% of the molecules react in the two-step process, the overall rate of which is limited by the 74 ± 6 ps time constant. The remaining 17% of the molecules dissociate in the faster channel, with a time constant of 640 ± 130 fs. This can be seen by the kink in the curve of Figure 4, intercepted by the black dashed line, before the curve continues to decrease to −38.9% at 1 ns. The 640 fs time constant is close to the previously observed 540 fs time constant for internal conversion within the 3p manifold, suggesting that both processes have a related dynamic origin that remains to be explored. The minor channel could explain the high kinetic energy channel seen by Forde et al. with 193 nm excitation.

In summary, the X-ray scattering signal in the limit of $q \to 0$ scales as the square of the number of electrons of a molecule, a result of the coherent addition of scattering amplitudes. During a dissociation process, the coherence is lost as the fragments essentially become independent well-separated species in a random ensemble of scatterers. Consequently, the pump–probe scattering signals extrapolated to $q \to 0$ can be used to directly measure the change in the number of electrons in the molecules participating in a chemical reaction. In a dissociation reaction, the number of electrons in each fragment is different from the reactant molecule, and the quadratic dependence of the signal on the number of electrons renders the detection of this change quite sensitive. In the dissociation of TMA, we have found the changes in the $q \to 0$ scattering intensity to be in excellent agreement with the electron counts of the transient species of the reaction. Upon excitation at 200 nm, TMA decays into $DMA + CH_3$ in either the previously known relaxation to the 3s state followed by a dissociation with a 74 ps time constant or through a faster process with a 640 fs time constant. It is possible that the latter process is directly tied to the internal conversion within the 3p manifold. In previous studies of tertiary amines, it has been noted that one of the 3p states is dissociative along the N–C coordinate.[25,26] Here we observe that in traversing the conical intersection with other 3p states along this bond stretching coordinate, 17% of the population dissociates while the rest undergoes internal conversion, as observed in the photoelectron spectra.[11,12] This result also highlights that X-ray scattering provides a direct measurement of populations in competing reaction channels without a reliance on knowledge of photoionization cross-sections.

The experimental scattering patterns of the transient radical DMA species is consistent with a bent structure with a bond angle of 118° and a C–N bond distance of 1.45 Å, which isin good agreement with computational structures. The experiment also yields scattering signals of the electronically excited TMA species. Their analysis will require an in-depth calculation of the electron density distributions and pair correlation functions, the vibrational motions of the hot reaction transients, and the coupling between electronic and nuclear motions during large-amplitude vibrations. As free-electron lasers advance into harder X-ray regimes, larger q ranges can be captured, yielding even more structural detail of reaction intermediates. All these advances will benefit from the anchor of simplicity that the coherent addition of $q \to 0$ signals provides in determining the overall chemical reaction kinetics.

Acknowledgements

This work was supported by the U.S. Department of Energy, Office of Science, Basic Energy Sciences, under Award DESC0017995. Use of the Linac Coherent Light Source (LCLS), SLAC National Accelerator Laboratory, is supported by the U.S. Department of Energy, Office of Science, Office of Basic Energy Sciences under Contract No. DE-AC02-76SF00515. A.K. acknowledges support from a Royal Society of Edinburgh Sabbatical Fellowship (58507) and a research grant from the Carnegie Trust for the Universities of Scotland (CRG050414). N.Z. acknowledges a Carnegie Ph.D. Scholarship, D.B. an EPSRC Ph.D. studentship from the University of Edinburgh.

Conflict of interest

The authors declare no conflict of interest.

Keywords: free-electron lasers · gas-phase kinetics · photodissociation dynamics · ultrafast X-ray scattering

How to cite: *Angew. Chem. Int. Ed.* **2019**, *58*, 6371 – 6375
Angew. Chem. **2019**, *131*, 6437 – 6441

[1] A. Barty, J. Küpper, H. N. Chapman, *Annu. Rev. Phys. Chem.* **2013**, *64*, 415 – 435.
[2] C. Bostedt, et al., *J. Phys. B* **2013**, *46*, 164003 – 164023.
[3] S. Boutet, G. J. Williams, *New J. Phys.* **2010**, *12*, 035024 – 035047.
[4] A. Moreno Carrascosa, T. Northey, A. Kirrander, *Phys. Chem. Chem. Phys.* **2017**, *19*, 7853.
[5] S. Ryu, R. M. Stratt, K. K. Baeck, P. M. Weber, *J. Phys. Chem. A* **2004**, *108*, 1189.
[6] R. W. James, *The Optical Principles of the Diffraction of X-Rays*, G. Bell and Sons, Ltd., London, **1948**.
[7] A. D. Smith, E. M. Warne, D. Bellshaw, D. A. Horke, M. Tudorovskya, E. Springate, A. J. H. Jones, C. Cacho, R. T. Chapman, A. Kirrander, R. S. Minns, *Phys. Rev. Lett.* **2018**, *120*, 183003.
[8] J. D. Cardoza, F. M. Rudakov, P. M. Weber, *J. Phys. Chem.* **2008**, *112*, 10736 – 10743.
[9] J. D. Cardoza, P. M. Weber, *J. Chem. Phys.* **2007**, *127*, 036101 – 036102.
[10] N. R. Forde, M. L. Morton, S. L. Curry, S. J. Wrenn, L. J. Butler, *J. Chem. Phys.* **1999**, *111*, 4558 – 4568.
[11] N. R. Forde, L. J. Butler, B. Ruscic, O. Sorkhabi, F. Qi, A. Suits, *J. Chem. Phys.* **2000**, *113*, 3088 – 3097.
[12] E. B. Warren, *X-Ray Diffraction*, Addison-Wesley, **1969** and Dover Publication, **1990**.
[13] M. Ben-Nun, T. J. Martinez, P. M. Weber, K. R. Wilson, *Chem. Phys. Lett.* **1996**, *262*, 405 – 414.
[14] A. Kirrander, *J. Chem. Phys.* **2012**, *137*, 154310.
[15] T. Northey, N. Zotev, A. Kirrander, *J. Chem. Theory Comput.* **2014**, *10*, 4911.
[16] T. Northey, A. Moreno Carrascosa, S. Schäfer, A. Kirrander, *J. Chem. Phys.* **2016**, *145*, 154304.
[17] J. D. Geiser, P. M. Weber, *J. Chem. Phys.* **1998**, *108*, 8004.
[18] M. P. Minitti, J. M. Budarz, A. Kirrander, J. Robinson, T. J. Lane, D. Ratner, K. Saita, T. Northey, B. Stankus, V. Cofer-Shabica, J. Hastings, P. M. Weber, *Faraday Discuss.* **2014**, *171*, 81 – 91.
[19] J. M. Budarz, M. P. Minitti, D. V. Cofer-Shabica, B. Stankus, A. Kirrander, J. B. Hastings, P. M. Weber, *J. Phys. B* **2016**, *49*, 034001 – 034012.
[20] M. P. Minitti, J. M. Budarz, A. Kirrander, J. S. Robinson, D. Ratner, T. J. Lane, D. Zhu, J. M. Glownia, M. Kozina, H. T. Lemke, M. Sikorski, Y. Feng, S. Nelson, K. Saita, B. Stankus, T. Northey, J. B. Hastings, P. M. Weber, *Phys. Rev. Lett.* **2015**, *114*, 255501.
[21] J. M. Glownia, et al., *Phys. Rev. Lett.* **2016**, *117*, 153003.
[22] K. Gumerlock, J. Frisch, B. Hill, J. May, D. Nelson, S. Smith, Proceedings of FEL2014, **2014**, Basel, Switzerland.
[23] *Landolt-Bornstein: Group II,: Atomic and Molecular Physics Volume 7: Structure Data of Free Polyatomic Molecules* (Eds.: K. H. Hellwege, A. M. Hellwege), Springer, Berlin, **1976**.
[24] G. Herzberg, *Electronic spectra and electronic structure of polyatomic molecules*, Van Nostrand, New York, **1966**.
[25] J. O. F. Thompson, L. B. Klein, T. I. Solling, M. J. Paterson, D. Townsend, *Chem. Sci.* **2016**, *7*, 1826 – 1839.
[26] L. B. Klein, T. J. Morsing, R. A. Livingstone, D. Townsend, T. I. Solling, *Phys. Chem. Chem. Phys.* **2016**, *18*, 9715 – 9723.

Manuscript received: February 19, 2019
Accepted manuscript online: March 13, 2019
Version of record online: April 1, 2019

Angewandte Chemie
Eine Zeitschrift der Gesellschaft Deutscher Chemiker

Supporting Information

Simplicity Beneath Complexity: Counting Molecular Electrons Reveals Transients and Kinetics of Photodissociation Reactions

Jennifer M. Ruddock, Nikola Zotev, Brian Stankus, Haiwang Yong, Darren Bellshaw, Sébastien Boutet, Thomas J. Lane, Mengning Liang, Sergio Carbajo, Wenpeng Du, Adam Kirrander, Michael Minitti, and Peter M. Weber**

anie_201902228_sm_miscellaneous_information.pdf

TMA Supplementary Information

TABLE OF CONTENTS

1. Experimental Method:

This experiment was performed at the LCLS CXI instrument at SLAC National Accelerator Laboratory. [S1] The general experimental set-up has been previously described. [18,19] In the SC1 chamber, TMA was allowed to flow through a gas manifold at 6.05 Torr (Fig. S1(a)), measured with a Baratron manometer on the sample line. It was pumped with 200 nm light pulses focused to ~35 μm focus, ~90 fs FWHM, ~1.5 μJ. The laser focus diameter was determined by visual inspection using the built-in microscope, and the pulse duration and pulse energy were extrapolated from measurements upstream and downstream. The TMA was probed with 9.48 keV X-ray photons (Fig. S1(b)) with ≈3 mJ pulse energy, 30 fs FWHM and 30 μm focus. The x-ray scattering from the TMA was measured using the CSPAD detector.

2. Treatment of the Scattering Images

To maintain uniformity in the data, shots with X-ray energies less than 9.475 keV or greater than 9.483 keV were not included in the analysis.

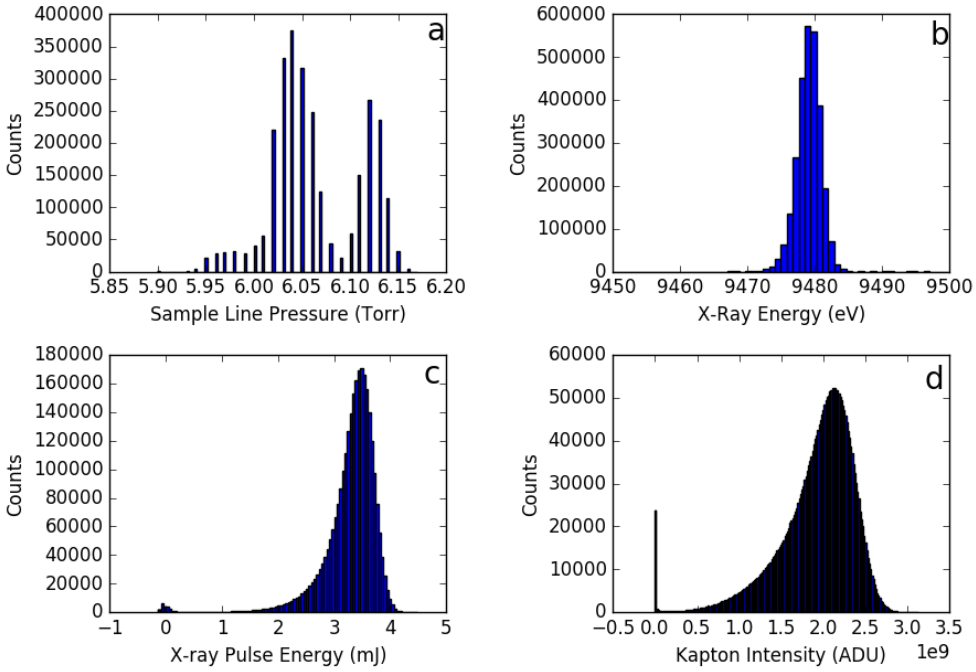

Figure S1. Shot-by-shot histograms of (a) the sample line pressure of the TMA, (b) X-ray photon energy, (c) the X-ray pulse energy as measured by the gas detector, and (d) the SC2 CSPAD intensity.

To account for shot-by-shot fluctuations in the X-ray pulse energy, a second CSPAD in SC2 was used to measure scattering from a Kapton foil. A histogram of the summed CSPAD intensities is shown in Figure S1 (d). The intensity measured on this second CSPAD was used to scale the intensities measured on the front CSPAD. Shots with CSPAD intensities below 1.3×10^9 ADU were not included in the analysis. In addition to this intensity scaling, the shots were also processed in batches of 3600 shots, and scaled by the average of the UV-off intensity, which accounts for short-time pressure fluctuations occurring in the sample line.

The timing of the UV-X-ray delay was controlled using an electronic delay of the UV pump. The fine-timing to account for the jitter of the X-rays was measured with the timetool.[S2] To make sure the timing was accurate, we used cut-offs on shots for which the timetool camera did not yield a good measurement. Figure S2 shows histograms of the timetool parameters used for determining the goodness of the shot: The pixel position on the camera, the amplitude of the error-function, and the width of the error-function. Shots with amplitudes less than 0.03 or greater than 0.13 were discarded, shots that came in at pixel positions less than 350 or greater than 900 were also discarded. And shots with FWHM peak widths less than 50 or greater than 450 were discarded.

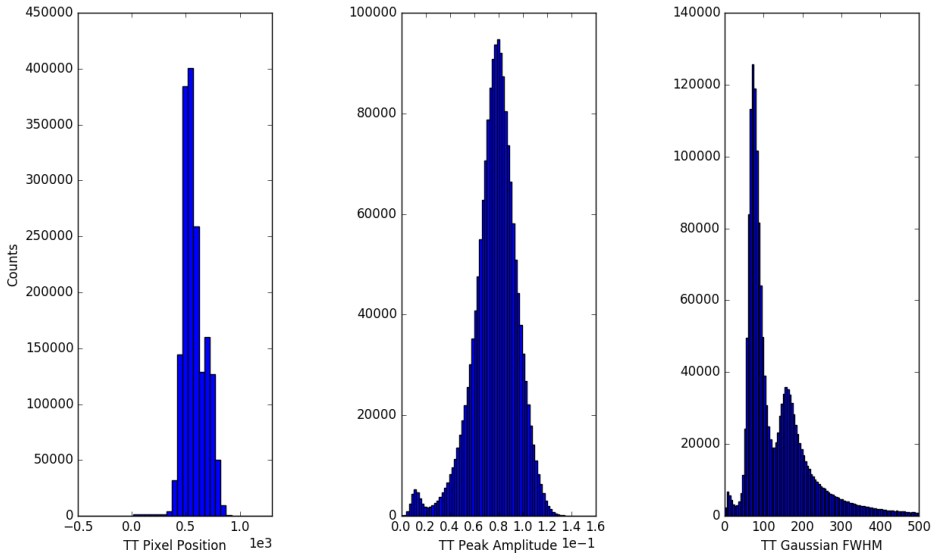

Figure S2. Histograms of timetool (TT) parameters. The left plot is the pixel position on the Opal camera, middle histogram is the peak amplitude, and the right histogram is the Gaussian FWHM of the onset of the peak.

The CSPAD pixel readout can be affected by bleeding of signal from nearest-neighbor pixels: a pixel may show a non-zero intensity if the pixel next to it detects a photon. This can be seen in the histogram of pixel intensities, shown in Figure S3. The one-photon peak has a maximum at 27.3 ADU (Figure S2, inset). When analyzing the detector images, any pixels with values less than 15.8 ADU, the minimum between the 0 and 1 photon peaks, are set to 0.

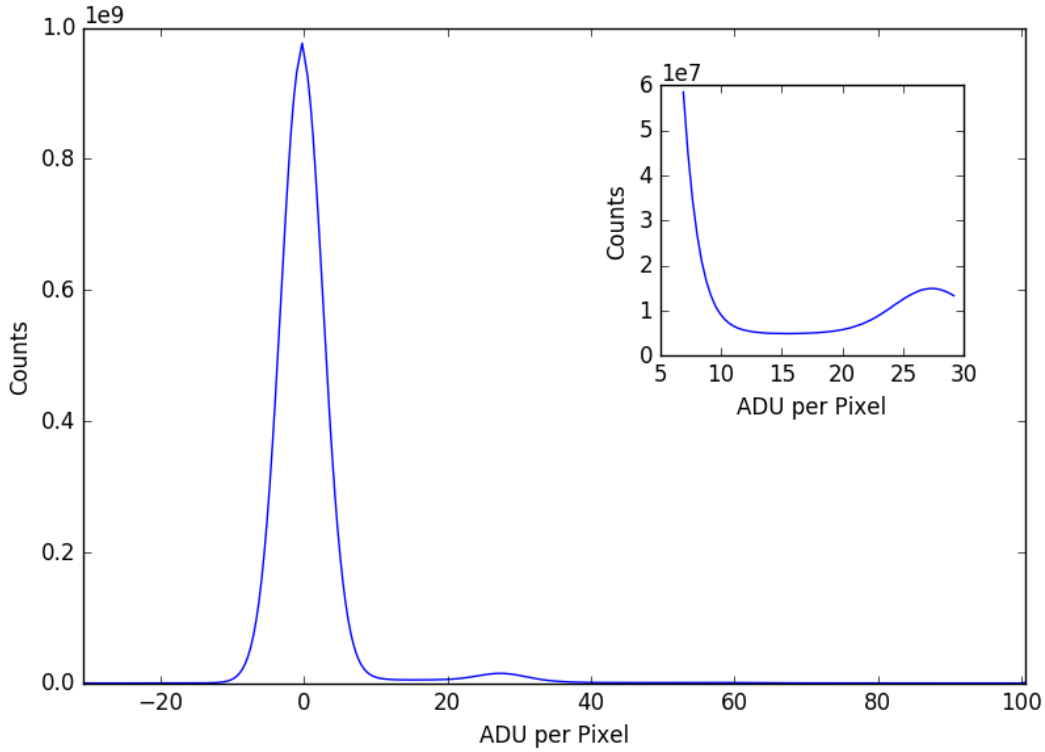

Figure S3. A histogram of the ADU per pixel on the CSPAD, the inset shows the minimum between the zero- and one-photon peaks.

All the images are collected and averaged over the number of shots taken.

Building a mask:

To prevent 'bad' pixels on the CSPAD from affecting the images used in the analysis, we masked pixels that consistently yielded outlier readouts. Taking an initial mask of unbonded pixels, and then using a dark image (without X-ray scattering) of the CSPAD, any pixel with a readout less than -2 ADU or greater than 2 ADU was masked.

In addition, spurious scattering from an upstream platinum pinhole in the diffractometer (Figure S4a) was also masked based on the ADU readout as compared to the average for a given distance from the center of the detector.

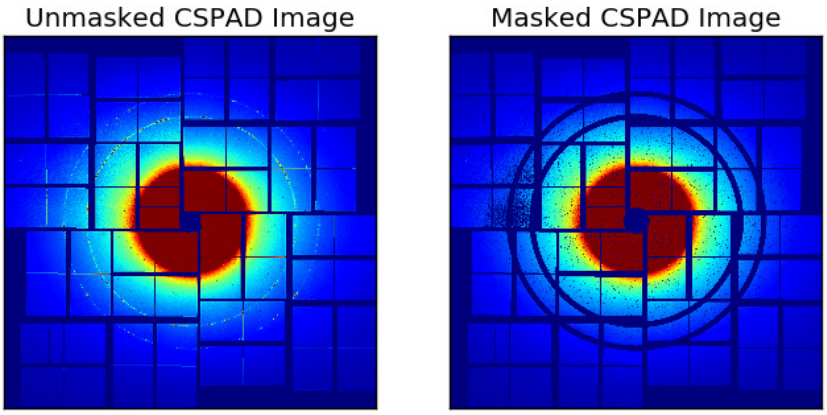

Figure S4. The left image shows the CSPAD image without a mask, showing platinum scattering rings. In the right plot, the CSPAD is masked to remove those extraneous rings.

Calibrating the detector distance:

To calibrate the detector distance, a least-squares fit is taken of the ground-state TMA scattering pattern as compared to the independent atom model (IAM) TMA pattern. The following equivalency was used:

$$\frac{I_{exp}}{\cos^3 2\theta} = I_{IAM}\left(\sin^2\phi + \cos^2\phi\cos^2 2\theta\right) \qquad \text{(Eqn. S1)}$$

The $\cos^3 2\theta$ factor on the left-hand side is to account for two things: one is the scaling of the X-ray scattering intensity with the square of the distance to a pixel on the detector, and the other is the effective area of the pixels with respect to the scattering angle from the interaction region. The ϕ dependent term on the right-hand side accounts for the horizontal polarization of the X-rays.

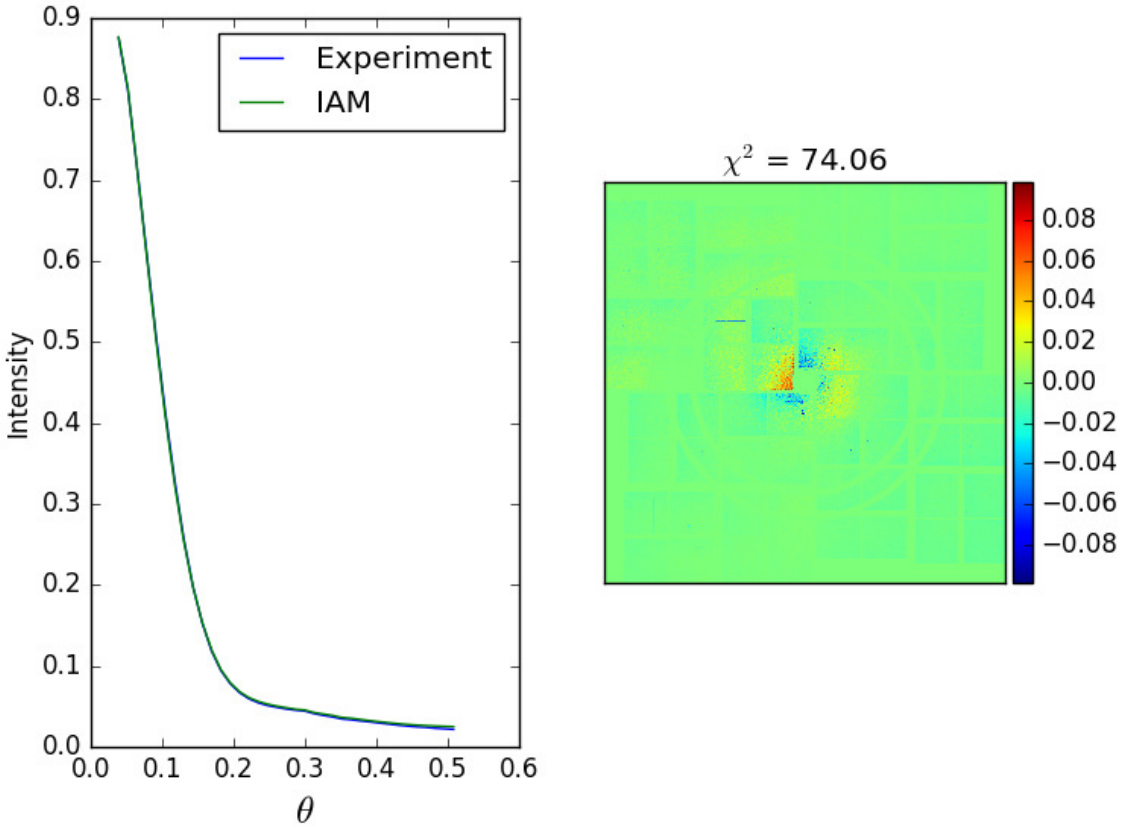

Figure S5. The left plot shows the experimental and theoretical (IAM) radially averaged TMA scattering patterns. The right plot shows a color-mapping of the difference experiment-theory on the CSPAD.

Error Analysis:

Errors in the measurement might arise from the pixelated nature of the CSPAD detector, from the intensity calibration of the X-ray pulses and from pulse-to-pulse variations of the optical pump laser intensity. There are also faint traces of scattering from the platinum pinholes, which, however, affect specific q values only. The average number of photons per q-bin, $\bar{I}(q)$, is

$$\bar{I}(q) = \frac{1}{N_{shots}} \times \frac{\sum_{pixels \in q} I}{\sum_{pixels \in q} 1} \qquad \text{(Eqn. S2)}$$

where N_{shots} is the number of X-ray pulses, and *I* is the total number of photons over the accumulated frames scattered into a set of pixels that are part of the q bin. The number of photons is calculated by dividing the total intensity of the summed images by 27.3 ADU/photon (the maximum ADU value of the one-photon peak, as shown in Figure S3).

The dominant source of error is the counting statistics of photons, which we take to be the square root of the number of photons scattered into a q range:

$$\Delta\bar{I}(q) = \frac{1}{N_{shots}} \times \frac{\sqrt{\sum_{pixels \in q} I}}{\sum_{pixels \in q} 1} \qquad \text{(Eqn. S3)}$$

Error propagation gives the error in the percent difference scattering signals as

$$\Delta^2[\%\Delta I](q,t) = \left(\frac{100}{\bar{I}_{off}(q)}\right)^2 \times \left((\Delta\bar{I}on(q,t))^2 + \left(\frac{\bar{I}_{on}(q,t)}{\bar{I}_{off}(q)}\right)^2 (\Delta\bar{I}off(q))^2\right) \qquad \text{(Eqn. S4)}$$

Where $\%\Delta I$ is the percent difference intensity as defined in Eqn 5.

Time zero

During the experiment, time zero was estimated by the ability to see a difference curve of the UV-excited TMA intensity. To get a more accurate time zero, the rise of the change in intensity was fit to an error function. The range of 2.07 – 2.74 Å^{-1} was chosen because it had the greatest amplitude change in intensity. The results are shown in Figure S6, with time zero being at -26 fs (relative to the arbitrary time zero chosen during the data acquisition), and a Gaussian FWHM of 148 fs.

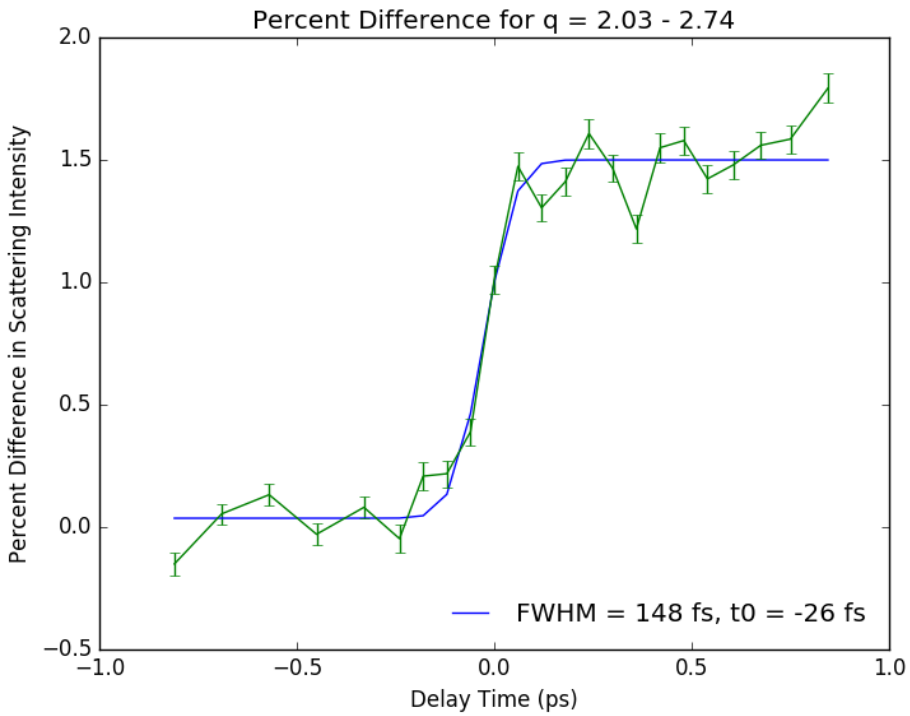

Figure S6. Error function fit of the time dependent difference scattering signal in the q-range from 2.03 to 2.74 Å^{-1}.

Even without explicit alignment of the molecules in the sample, the scattering signal shows a strong time-varying anisotropy which originates from the selective excitation of molecules whose transition dipole moment aligns with the pump polarisation axis, and the subsequent rotational dephasing. It is a common practice to rotationally average the angular-resolved signal to achieve a higher signal-to-noise ratio. In addition to discarding information about the

orientation of the molecular ensemble with respect to the laboratory frame, such a procedure may induce a non-negligible error in the interpretation of the experiment.[S5] It has been shown that a more rigorous treatment is given by a plane wave expansion of the detected scattering signal so that the percentage intensity change is cast into the form:[S6,S7]

$$\%\Delta I(q,\phi,t) = \sum_{l=0}^{\infty} P_l(-\cos\phi_p \cos\frac{\theta}{2})\ \%\Delta I_l(q,t),$$

where ϕ_p is the azimuthal angle with respect to the laser polarization axis, and P_l denotes the Legendre polynomial of order l. For a single-photon excitation, only the first two even $\%\Delta I_l$ terms are non-zero, where $l = 0$ and $l = 2$ represent the isotropic and anisotropic contributions to scattering, respectively. Consequently, the separation of the two terms becomes a linear fitting problem for each fixed time-delay and magnitude of the scattering vector.[S8] The following analysis is based on the isotropic signal only. We leave the interpretation of the observed anisotropy for a future publication.

The 3 ns time point

In the analysis of the data, we found the overall scattering signal had decreased for the 3 ns time point, resulting in a distorted percent different scattering signal. We realized that this was probably due to the geometry of the experiment. From Forde, et al. we can estimate the velocities of the dissociation fragments to be ~2-3 μm/ns.[8,9] Therefore, after 3 ns, a significant amount of the fragments is ejected from the 30 μm interaction region, resulting in the distortion of the pump-probe signal. We decided this data point could not be directly compared to the other data points and therefore did not include it in our analysis.

3. Fitting the Data to a kinetics scheme

The isotropic components are used to derive the kinetics, Equation 6. An IAM pattern produced a good fit to the 1ns time point to obtain A_{DMA} (Figure 3). From this fit we estimate the percent excitation to be ≈1.83%, therefore the likelihood of 2-photon ionization is low. The early time points (<0.5 ps) were not well-reproduced with an IAM pattern of TMA, most likely due to the diffuse nature of the electronically excited state. Therefore, the data at the 0.12 ps time point was fitted to the following functional form:

$$\%\Delta I(q,0.12ps) = \left(1-\mathrm{erf}\left(\sigma(q-\mu)\right)\right)\times\sum_1^2 c_i\frac{\sin(qr_i)}{qr_i} + \mathrm{erf}(\sigma(q-\mu))\times\sum_3^8 c_i\frac{\sin(qr_i)}{qr_i} \quad \text{(Eqn. S5)}$$

This is two sinc functions spliced together with an error function of center $\mu = 1.19\ \text{Å}^{-1}$ and $\sigma = 3$. The splice was used because it was important to obtain a good fit at low q, with the percent difference intensity at q=0 set to 0. The resulting fit is shown in Figure S7, and fit parameters are listed in Table S1.

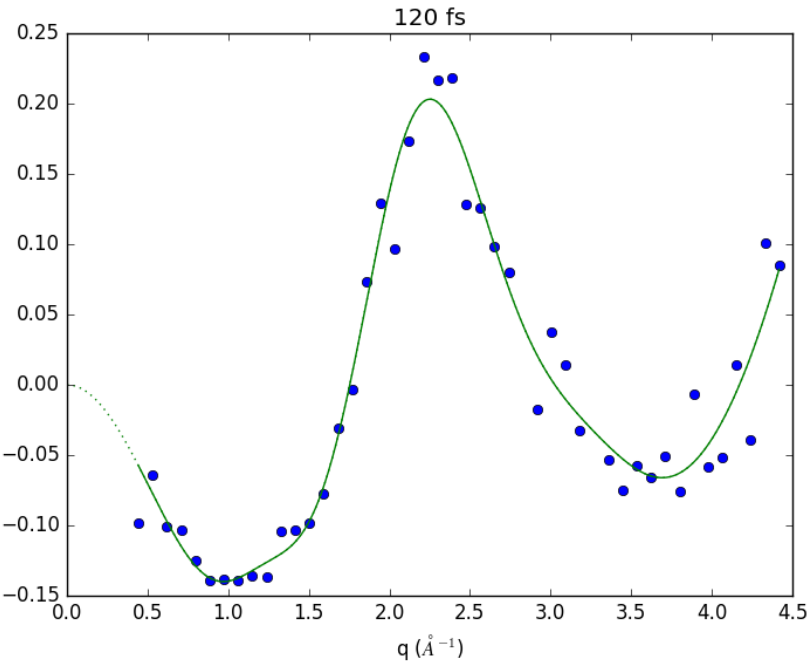

Figure S7. The fit of the data at 0.12ps to Equation S5 using the parameters in Table S1.

Table S1. The parameters as shown in Equation S5.

i	c_i	r_i
1	84.55	5.472
2	-84.55	1.522
3	111.39	4.242
4	-85.99	2.132
5	-30.34	1.164
6	8.92	6.411
7	-98.61	4.313

To find errors in the DMA structure parameters, the method described in references S3 and S4 is used. The error in a parameter p is estimated by changing p by a small amount dp, fixing that parameter, and refitting to find a new minimum sum of squares, $\mathcal{X}^2$. Then the following equation is used:

$$\Delta p \approx \frac{dp}{\sqrt{d\mathcal{X}^2}} \qquad \text{(Eqn. S6)}$$

Full References

2. C. Bostedt, J. D. Bozek, P. H. Bucksbaum, R. N. Coffee, J. B. Hastings, Z. Huang, R. W. Lee, S. Schorb, J. N. Corlett, P. Denes, P. Emma, R. W. Falcone, R. W. Schoenlein, G. Doumy, E. P. Kanter, B. Kraessig, S. Southworth, L. Young, L. Fang, M. Hoener, N. Berrah, C. Roedig and L. F. DiMauro, *J Phys B: At Mol Opt Phys* **2013**, *46*, 164003-164023.

19. J. M. Glownia, et al. A. Natan, J. P. Cryan, R. Hartsock, M. Kozina, M. P. Minitti, S. Nelson, J. Robinson, T. Sato, T. van Driel, G. Welch, C. Weninger, D. Zhu, and P. H. Bucksbaum, *Phys. Rev. Lett.*. **2016**, 117, 153003.
S1. S. Boutet, G. J. Williams, *New J. Physics*. **2010**, 12, 035024.
S2. M. Harmand, R. Coffee, M.R. Bionta, M. Chollet, D. French, D. Zhu, D. M. Fritz, H. T. Lemke, N. Medvedev, B. Ziaja, S. Toleikis, M. Cammarata, *Nat. Phot.*. **2013**, 7, 215-218.
S3. P.J. Cumpson, M. P. Seah, *Surface and Interface Analsysis* 1992, 18, 345.
S4. J. P. Cryan, 'Strong field and x-ray interactions with aligned molecules', PhD Thesis, 2012, Stanford University, Stanford, CA.
S5. J. S. Baskin and A. H. Zewail, "Oriented Ensembles in Ultrafast Electron Diffraction," *ChemPhysChem*, vol. 7, no. 7, pp. 1562–1574, Jul. 2006.
S6. J. S. Baskin and A. H. Zewail, "Ultrafast Electron Diffraction: Oriented Molecular Structures in Space and Time," *ChemPhysChem*, vol. 6, no. 11, pp. 2261–2276, Nov. 2005.
S7. U. Lorenz, K. B. Møller, and N. E. Henriksen, "On the interpretation of time-resolved anisotropic diffraction patterns," *New Journal of Physics*, vol. 12, no. 11, p. 113022, Nov. 2010.
S8. M. Ben-Nun, J. Cao, and K. R. Wilson, "Ultrafast x-ray and electron diffraction: theoretical considerations," *The Journal of Physical Chemistry A*, vol. 101, no. 47, pp. 8743–8761, 1997.

7.3 Conclusion

This study explored the capabilities of UXS to determine reaction kinetics. In a way, this is a more classical application of the technique. After all, there are numerous other ways of studying reaction rates in the realm of time-resolved spectroscopy. However, the ability to determine transient structures adds an extra dimension to this work, and shows some of the advantages of monitoring reactions from the perspective of the structure evolution instead of their energetics.

Reflecting critically on the work, there are two main shortcomings. The first one stems from the fact that the DMA radical, as well as the TMA molecule still in the Rydberg manifold, are vibrationally hot. Even if the kinetic energy is initially localised to a single mode, there is enough time for it to dissipate to other modes of motion thus creating a rather wide vibrational wave packet. It is then highly likely that the scattering patterns are the result of a spread of possible structures rather than a single one. However, as detailed in the previous chapter, a simultaneous fit with multiple geometries is prone to failures. A second point of criticism is the neglect of the second dissociation step reported by other authors. Even if the population of dissociated DMA radicals is small on the scale of the experiment, that might have implications for the transient structure found here. It should be pointed out that the drop of the signal as $q \to 0$ as a result of loss of interference between the NMMA and the hydrogen atom is really small – approximately 4% of all DMA dissociates. In other words, it is hard to detect solely from the signal at $q \to 0$ without appreciable fraction of DMA undergoing this reaction. Should a small fraction of NMMA be present, the determined DMA transient structure would be slightly skewed towards the NMMA geometry.

Chapter 8

Conclusion

UXS experiments can currently only be performed at XFEL facilities, which are the only light sources that fulfil simultaneously the requirements for short X-ray pulse duration and high brightness. Exciting a molecule and monitoring its dynamics in a pump-probe fashion, UXS is a unique tool for studying the fast transformations that accompany the majority of photochemical reactions. The advantage of performing the experiments in the gas phase is that molecular motion is unconstrained and close to ideal. In addition, there is no intermolecular scattering interference in this environment, which means that the detected signal originates from a single molecule with all its quantum peculiarities. The aim of this thesis has been to outline the theory of UXS and encompass a number of theory-related aspects with a practical significance for experimental work.

The theoretical description of UXS presented in Chapter 2, is concerned with three main processes - photoexcitation, dynamics and X-ray scattering. Firstly, assuming that the ensemble of molecules is initially in its ground vibronic state with no preferential alignment as a result of a broad population of rotational states, a linearly polarised optical laser prepares a wave packet on one or more excited states. The probability of excitation is related to the square of the TDM. The excited state exhibits a cosine-squared orientation with respect to the angle between the laser polarisation axis and the TDM. This symmetry breaking renders the scattering signal anisotropic. The evolution of the nuclear wave packet on the manifold of excited states is inherently non-adiabatic. After passing through regions of conical intersections, the molecule can reach a large number of final products. A first-principles

description of X-ray scattering helps us appreciate how UXS can monitor the changes that occur in both nuclear geometry and electronic states.

As detailed in Chapter 3, there are a number of procedures that can be applied to the raw experimental data to reveal better the information content. These include the decomposition of the raw signal into isotropic and anisotropic components, as well as converting it to fractional signal change. Even after these manipulations, certain information about the real space structure of the molecule cannot be retrieved, which can be attributed to both experimental and fundamental limitations. This is why UXS scattering relies on theoretical and computational tools to aid the analysis.

In Chapter 4 we described some common methods for calculating exciting electronic states, as well as algorithms for numerical propagation of the nuclear wave packet on the excited states' PESs. Importantly, a new approach for computing isotropic X-ray scattering cross-sections directly from the *ab initio* electronic density was presented.

Chapters 5-7 covered applications of the theory and computational methods to actual experimental data. The alignment of the TDM with the pump pulse polarisation axis and its direction in the molecular frame of reference were shown to enable the determination of the initially excited electronic state in NMM. The subsequent coherent vibrations were retrieved from the scattering data by a constraint-fit procedure which relied on a pool of theoretical structures. Finally, in the case of excitation to a 3p Rydberg state in TMA, the resulting dissociation channels, their rate constants and the geometry of transient species were investigated.

Looking ahead, a number of upcoming milestones for UXS can be anticipated. The first immediate one is to provide a concrete proof that electron delocalisation associated with excited electronic states can be observed simultaneously with the structure evolution. The work on coherent motion in NMM presented here already touches upon this subject. It has been shown that the effect of electronic rearrangements can rival that of nuclear motion in some cases. While not discussed in this thesis, a recent work has been able to demonstrate more robustly that the initial redistribution of the electron density associated with photoexcitation before the onset of nuclear motion

can indeed by captured directly in UXS experiments [125]. However, the simultaneous direct observation of nuclear motion and electron redistribution via UXS is still challenging and calls for an improved signal level. The upcoming upgrades to LCLS-II and the new European XFEL offer hope that new work in this direction will follow in the not-so-distant future.

A smaller effect, but still in principle observable, electron correlation is one of the aspects that makes UXS attractive for fundamental studies of electronic structure and a potential method for benchmarking *ab initio* calculations. In the absence of energy resolution, correlation is encoded in the difference between total and elastic scattering, sometimes referred to as total inelastic scattering. Contrary to the established approach to treat it as a constant background, it is not structureless or isotropic but contains vital information for the collective motion of the electrons.

Another interesting aspect that has been systematically neglected in UXS experiments that are concerned with structural changes, is the anisotropy of the signal and its time evolution. While it has been shown here that it can be used as a reliable way to determine the initially accessed electronic state, its time evolution can also provide information about rotational properties of the molecule. Especially when it is coupled to large structural changes such as dissociation, the changes in the rotational constants can be used to pinpoint the time-scale of structural deformations. Similarly, the scattering anisotropy directly encodes for the internal structure of the molecule. It can thus be used to supplement the structure determination methods that utilise the isotropic scattering component.

This thesis has not discussed in great length the so-called coherent mixed scattering – the scattering that originates from the interference between two electronic states. The strength of coherent mixed scattering is governed by three main factors - the states' symmetry, their separation and the overlap between the corresponding nuclear wave packet. As with other cases where two electronic states are involved, coherent mixed scattering is subject to selection rules. In absence of energy resolution gating, only states of the same symmetry can exhibit this type of scattering. Hence, one possibility

to observe it is in regions of conical intersections. However, there the nuclear wave packet overlap might be small [126], so that the contribution to the total signal is weak. Another possibility is to prepare a wave packet on two independent states, so that there is a good nuclear overlap. However, the energy difference between the electronic states needs to be small, otherwise the coherent mixed scattering will oscillate rapidly in time. Its detection would only be possible with extremely short X-ray pulses on order of a femtosecond or shorter. In either case, a clever experimental set up combined with a well-targeted system would be needed in order to show coherent mixed scattering experimentally.

This thesis has described some of the recent advances in the theory, interpretation and analysis of UXS experiments. While still in its early days, UXS has shown a great capacity to elucidate photochemical dynamics. Unlike rival spectroscopic techniques, it monitors structural evolution directly, which makes it both tangible and powerful. The future of UXS is as bright as XFELs themselves. However, a real success can only be achieved through the development of rigorous theory and computational tools.

Bibliography

[1] N. L. Rangel, K. S. Williams, and J. M. Seminario. *J. Phys. Chem. A* **113**, 6740 (2009).

[2] V. Balzani, A. Credi, and M. Venturi. *ChemSusChem* **1**, 26 (2008).

[3] R. J. D. Miller. *Faraday Discuss.* **194**, 777 (2016).

[4] G. A. Worth and L. S. Cederbaum. *Annu. Rev. Phys.* **55**, 127 (2004).

[5] W. Domcke and D. R. Yarkony. *Annu. Rev. Phys.* **63**, 325 (2012).

[6] N. J. Turro. *Modern Molecular Photochemistry*. University Science Books, 1991.

[7] D. Bates and A. Kingston. *Nature* **189**, 652 (1961).

[8] R. W. P. McWhirter. *Nature* **190**, 902 (1961).

[9] A. Cox, T. J. Kemp, *et al. Introductory Photochemistry*. McGraw-Hill, 1971.

[10] S. Mukamel. *Principles of Nonlinear Optical Spectroscopy*. Vol. 29. Oxford University Press, 1995.

[11] R. J. Squibb *et al. Nat. Commun.* **9**, 63 (2018).

[12] M. Born and R. Oppenheimer. *Ann. Phys.* **389**, 457 (1927).

[13] H. Trommsorff. *Ann. Chem. Pharm.* **11**, 190 (1834).

[14] R. G. W. Norrish and G. Porter. *Nature* **164**, 658 (1949).

[15] G. Porter. *Proc. R. Soc. A: Math. Phys. and Eng. Sci.* **200**, 284 (1950).

[16] W. R. Lambert, P. M. Felker, and A. H. Zewail. *J. Chem. Phys.* **75**, 5958 (1981).

[17] L. R. Khundkar and A. H. Zewail. *Annu. Rev. Phys. Chem.* **41**, 15 (1990).

[18] G. Cerullo *et al. Photochem. Photobiol. Sci.* **6**, 135 (2007).

[19] J. Xu *et al. J. Phys. B* **49**, 112001 (2016).

[20] R. Bonifacio, C. Pellegrini, and L. Narducci. *Opt. Commun.* **50**, 373 (1984).

[21] J. Ullrich, A. Rudenko, and R. Moshammer. *Annu. Rev. Phys. Chem.* **63**, 635 (2012).

[22] M. M. Seibert *et al. Nature* **470**, 78 (2011).

[23] T. R. M. Barends *et al. Nature* **505**, 244 (2013).

[24] L. Young *et al. Nature* **466**, 56 (2010).

[25] K. Pande *et al. Science* **352**, 725 (2016).

[26] J. Duris *et al. Nat. Photonics* **14**, 30 (2020).

[27] S. Serkez *et al. J. Opt.* **20**, 024005 (2018).

[28] P. Emma *et al. Nat. Photonics* **4**, 641 (2010).

[29] T. Ishikawa *et al. Nat. Photonics* **6**, 540 (2012).

[30] H.-S. Kang *et al. Nat. Photonics* **11**, 708 (2017).

[31] W. Decking and H. Weise. *Proc. of International Particle Accelerator Conference*, MOXAA1 (2017).

[32] C. J. Milne *et al. Appl. Sci.* **7**, 720 (2017).

[33] V. Ayvazyan *et al. Eur. Phys. J. D* **37**, 297 (2006).

[34] V. Lyamayev *et al. J. Phys. B* **46**, 164007 (2013).

[35] D. Huang, D. Gu, and M. Zhang. *Proc. of the 39th Free Electron Laser Conf.* **FEL2019**, Germany (2019).

[36] M. P. Minitti *et al. Phys. Rev. Lett.* **114**, 255501 (2015).

[37] K. H. Kim *et al. Nature* **518**, 385 (2015).

[38] H. T. Lemke *et al. J. Phys. Chem. A* **117**, 735 (2013).

[39] P. Debye. *Phys. Z.* **28**, 135 (1927).

[40] R. James. *The Optical Principles of the Diffraction of X-Rays*. 6th ed. Vol. II. The Crystalline State. G. Bell and Sons Ltd, 1962.

[41] L. Bartell and R. Gavin. *J. Am. Chem. Soc.* **86**, 3493 (1964).

[42] L. Bartell and R. Gavin. *J. Chem. Phys.* **43**, 856 (1965).

[43] A. Debnarova and S. Techert. *J. Chem. Phys.* **125**, 224101 (2006).

[44] A. Debnarova, S. Techert, and S. Schmatz. *J. Chem. Phys.* **133**, 124309 (2010).

[45] A. Debnarova, S. Techert, and S. Schmatz. *J. Chem. Phys.* **134**, 054302 (2011).

[46] T. Northey, N. Zotev, and A. Kirrander. *J. Chem. Theory Comput.* **10**, 4911 (2014).

[47] T. Northey *et al. J. Chem. Phys.* **145**, 154304 (2016).

[48] A. Kirrander, K. Saita, and D. V. Shalashilin. *J. Chem. Theory Comput.* **12**, 957 (2016).

[49] A. Kirrander and P. M. Weber. *Appl. Science* **7**, 534 (2017).

[50] A. M. Carrascosa, T. Northey, and A. Kirrander. *Phys. Chem. Chem. Phys.* **19**, 7853 (2017).

[51] A. M. Carrascosa and A. Kirrander. *Phys. Chem. Chem. Phys.* **19**, 19545 (2017).

[52] A. M. Carrascosa *et al. J. Chem. Theory Comput.* **15**, 2836 (2019).

[53] R. M. Parrish and T. J. Martínez. *J. Chem. Theory Comput.* **15**, 1523 (2019).

[54] D. J. Tannor. *Introduction to Quantum Mechanics: a Time-Dependent Perspective*. University Science Books, 2007.

[55] J. J. Sakurai. *Advanced Quantum Mechanics*. Pearson Education India, 1967.

[56] R. Loudon. *The Quantum Theory of Light*. Oxford University Press, 2000.

[57] R. N. Zare. *Ber. Bunsenges. Phys. Chem.* **86**, 422 (1982).

[58] R. N. Zare. *Angular momentum: understanding spatial aspects in chemistry and physics*. J. Wiley & Sons, 1988.

[59] E. H. Van Kleef and I. Powis. *Mol. Phys.* **96**, 757 (1999).

[60] P. R. Bunker and P. Jensen. *Fundamentals of Molecular Symmetry*. CRC Press, 2018.

[61] C. M. Marian. *Wiley Interdiscip. Rev. Comput. Mol. Sci.* **2**, 187 (2012).

[62] B. Sutcliffe. *Adv. Chem. Phys.* **114**, 1 (2000).

[63] D. W. Jepsen and J. O. Hirschfelder. *J. Chem. Phys.* **32**, 1323 (1960).

[64] A. Fröman. *J. Chem. Phys.* **36**, 1490 (1962).

[65] W. Kołos and L. Wolniewicz. *Rev. Mod. Phys.* **35**, 473 (1963).

[66] M. Born and K. Huang. *Dynamical Theory of Crystal Lattices*. Clarendon Press, 1954.

[67] M. Born and V. Fock. *Z. Phys.* **51**, 165 (1928).

[68] N. E. Henriksen and K. B. Møller. *J. Phys. Chem. B* **112**, 558 (2008).

[69] U. Lorenz, K. B. Møller, and N. E. Henriksen. *Phys. Rev. A* **81** (2010).

[70] S. P. Hau-Riege. *Nonrelativistic Quantum X-ray Physics*. John Wiley & Sons, 2015.

[71] R. Santra. *J. Phys. B* **42**, 023001 (2008).

[72] W. Schülke. *Electron Dynamics by Inelastic X-ray Scattering*. Vol. 7. Oxford University Press, 2007.

[73] I. Waller and D. R. Hartree. *Proc. R. Soc. Lond. Ser. A* **124**, 119 (1929).

[74] M. Simmermacher *et al. J. Chem. Phys.* **151**, 174302 (2019).

[75] T. Helgaker, P. Jørgensen, and J. Olsen. *Molecular Electronic-Structure Theory*. John Wiley and Sons, 2000.

[76] G. Dixit, O. Vendrell, and R. Santra. *Proc. Natl. Acad. Sci.* **109**, 11636 (2012).

[77] M. Simmermacher, N. E. Henriksen, and K. B. Møller. *Phys. Chem. Chem. Phys.* **19**, 19740 (2017).

[78] K. Bennett *et al. Proc. Nat. Acad. Sci.* 1805335115 (2018).

[79] M. Simmermacher *et al. Phys. Rev. Lett.* **122**, 073003 (2019).

[80] J. M. Ruddock *et al. Sci. Adv.* **5**, eaax6625 (2019).

[81] P. M. Felker, J. S. Baskin, and A. H. Zewail. *J. Phys. Chem.* **90**, 724 (1986).

[82] P. M. Felker and A. H. Zewail. *J. Chem. Phys.* **86**, 2460 (1987).

[83] P. Felker. *J. Phys. Chem.* **96**, 7844 (1992).

[84] N. Zotev *et al. J. Chem. Theory Comput.* **16**, 2594 (2020).

[85] D. A. Kohl and E. J. Shipsey. *Z. Phys. D* **24**, 33 (1992).

[86] M. Ben-Nun, J. Cao, and K. R. Wilson. *J. Phys. Chem. A* **101**, 8743 (1997).

[87] J. Cao and K. R. Wilson. *J. Phys. Chem. A* **102**, 9523 (1998).

[88] J. S. Baskin and A. H. Zewail. *ChemPhysChem* **7**, 1562 (2006).

[89] U Lorenz, K. B. Møller, and N. E. Henriksen. *New J. Phys.* **12**, 113022 (2010).

[90] J. S. Baskin and A. H. Zewail. *ChemPhysChem* **6**, 2261 (2005).

[91] J. M. Budarz *et al. J. Phys. B: At. Mol. Opt. Phys.* **49**, 034001 (2016).

[92] P. Debye. *Ann. Phys.* **46**, 809 (1915).

[93] R. Bryan. *International Tables for Crystallography. Vol. C. Mathematical, Physical and Chemical Tables Edited by AJC Wilson*. 1993.

[94] P. A. Doyle and P. S. Turner. *Acta Crystallogr. A* **24**, 390 (1968).

[95] A. Fox, M. O'Keefe, and M. Tabbernor. *Acta Crystallogr. A* **45**, 786 (1989).

[96] M. Coulthard. *Proc. Phys. Soc.* **91**, 44 (1967).

[97] R. M. Gavin and L. S. Bartell. *J. Chem. Phys.* **44**, 3687 (1966).

[98] R. M. Gavin and L. S. Bartell. *J. Chem. Phys.* **45**, 4700 (1966).

[99] D. A. Kohl and L. S. Bartell. *J. Chem. Phys.* **51**, 2891 (1969).

[100] D. A. Kohl and L. S. Bartell. *J. Chem. Phys.* **51**, 2896 (1969).

[101] A. Szabo and N. S. Ostlund. *Modern Quantum Chemistry: Introduction to Advanced Electronic Structure Theory*. Dover Publications Inc., 2012.

[102] R. Martin. *Electronic Structure: Basic Theory and Practical Methods*. Cambridge University Press, 2004.

[103] K. Andersson *et al. J. Phys. Chem.* **94**, 5483 (1990).

[104] K. Andersson, P. Malmqvist, and B. O. Roos. *J. Chem. Phys.* **96**, 1218 (1992).

[105] J. Finley *et al. Chemical Physics Letters* **288**, 299 (1998).

[106] H.-D. Meyer, U. Manthe, and L. S. Cederbaum. *Chem. Phys. Lett.* **165**, 73 (1990).

[107] U. Manthe, H.-D. Meyer, and L. S. Cederbaum. *J. Chem. Phys.* **97**, 3199 (1992).

[108] G. A. Worth *et al. Int. Rev. Phys. Chem.* **27**, 569 (2008).

[109] G. W. Richings *et al. Int. Rev. Phys. Chem.* **34**, 269 (2015).

[110] B. G. Levine *et al. Chem. Phys.* **347**, 3 (2008).

[111] D. V. Makhov *et al. Chem. Phys.* **493**, 200 (2017).

[112] J. C. Tully. *J. Chem. Phys.* **93**, 1061 (1990).

[113] J. Wang and V. H. Smith. *Int. J. Quant. Chem.* **52**, 1145 (1994).

[114] C. Sarasola, J. Elorza, and J. Ugalde. *J. Math. Chem.* **23**, 405 (1998).

[115] A. J. Thakkar and B. S. Sharma. *Int. J. Quant. Chem.* **85**, 258 (2001).

[116] D. L. Crittenden and Y. A. Bernard. *J. Chem. Phys.* **131**, 054110 (2009).

[117] R. E. Hoffmeyer, P. Bündgen, and A. J. Thakkar. *J. Phys. B* **31**, 3675 (1998).

[118] L. McMurchie and E. Davidson. *J. Comput. Phys.* **26**, 218 (1978).

[119] H.-J. Werner *et al. WIREs Comput. Mol. Sci.* **2**, 242 (2012).

[120] H.-J. Werner *et al. MOLPRO, version 2012.1, a package of ab initio programs*.

[121] M. P. Minitti *et al. Faraday Discuss.* **171**, 81 (2014).

[122] J. M. Budarz *et al. J. Phys. B* **49**, 034001 (2016).

[123] N. R. Forde *et al. J. Chem. Phys.* **111**, 4558 (1999).

[124] N. R. Forde *et al. J. Chem. Phys.* **113**, 3088 (2000).

[125] H. Yong *et al. Nat. Commun.* **11** (2020).

[126] M. Kowalewski, K. Bennett, and S. Mukamel. *Struct. Dyn.* **4**, 054101 (2017).